ISSN 1580-2949
UDK 669+666+678+53 MTAEC9, 42(4)141–188(2008)

| MATER. TEHNOL. | LETNIK VOLUME 42 | ŠTEV. NO. 4 | STR. P. 141–188 | LJUBLJANA SLOVENIJA | JUL.–AUG. 2008 |
|---|---|---|---|---|---|

# VSEBINA – CONTENTS

UDK 620.1.08:537.5
Review article/Pregledni članek

ISSN 1580-2949
MTAEC9, 42(4)143(2008)

# APPLICATIONS OF FOCUSED ION BEAM IN MATERIAL SCIENCE

## UPORABA FOKUSIRANEGA IONSKEGA CURKA V ZNANOSTI MATERIALOV

**Luca Repetto, Giuseppe Firpo, Ugo Valbusa**

Nanomed Lab, Centro di Biotecnologie Avanzate – CBA, L.go R. Benzi, 10, 16132 Genova, Italy and Università of Genova, Physics Department, Via Dodecaneso, 33 16146 Genova, Italy
valbusa@fisica.unige.it

*Prejem rokopisa – received: 2007-10-08; sprejem za objavo – accepted for publication: 2008-06-24*

The focused ion beam (FIB) microscope is a tool that has a widespread use in the field of material science because it is able to micromachining with high resolution imaging thus therefore enhancing a broad range of both fundamental and technological applications in material science. The FIB is based on a beam of Ga ions which sputter the sample enabling precise machining at the nanometer/micrometer scale. The FIB instruments received particular attentions in the 1980s when the semiconductor industry used it as offline equipment for mask or circuit repair, but only in the 1990s the FIB was used in research laboratory. Nowadays there are commercial instruments (Dual Beam FIB / SEM) that integrate the precision cross section power of a FIB with the high resolution imaging of an SEM creating a powerful cross section and imaging tool. The combined SEM capability allows for real time monitoring of the FIB cuts with a higher resolution.

Key words: focused ion beam, ion source, dual beam instruments, ion-solid interactions, applications

Mikroskop s fokusiranim snopom ionov (FIB) je orodje s široko uporabnostjo v znanosti materialov, ker omogoča mikroobdelavo in opazovanje z veliko ločljivostjo in odpira široko področje temeljnih raziskav materialov in tehnoloških aplikacij. Podlaga FIB je curek Ga-ionov, s katerim se obstreljuje tarča, kar omogoča mikroobdelavo pri redu velikosti nanometer-mikrometer. Naprava FIB je vzbudila posebno pozornost v 80-ih letih, ko so jo uporabljali v industriji polprevodnikov za popravilo mask in tokokrogov, v 90-ih letih pa se je razširila tudi v raziskovalne laboratorije. Na voljo so komercialne naprave (Dual beam FIB), ki združujejo natančnost FIB z visoko ločljivostjo SEM, kar ustvari učinkovito orodje za obdelavo in opazovanje. Kombinirana naprava omogoča v realnem času opazovano FIB-obdelavo z veliko ločljivostjo.

Ključne besede: izvor ionov, naprava z dvojnim curkom, interakcija ion-trdna snov, uporaba

## 1 INTRODUCTION

In his famous talk on nanotechnology "There's Plenty of Room at the Bottom" held at the 1959 meeting of the American Physical Society at Caltech [1], Richard Feynman considered *"the problem of manipulating and controlling things on a small scale"*. As an example of this kind of manipulations, he considered the task of writing *"the entire 24 volumes of the Encyclopaedia Britannica on the head of a pin"* and for the purpose he imagined a machine which could afford this task: *"we can reverse the lenses of the electron microscope in order to demagnify as well as magnify. A source of ions, sent through the microscope lenses in reverse, could be focused to a very small spot"*.

Even if Feynman describes an interaction of the ions with the sample that is different from the one we know to happen (he postulates a deposition while we know that the result is a removal of atoms), all the same his words sounds like a very rough but essential picture of the focused ion beam (FIB).

In this paper we describe how this very intuitive idea has become a real instrument (in **Figure 1** we reproduce the result of Feynman's "experiment" with a modern FIB). In particular we will consider the state of the art of dual-beam instruments, where the FIB is coupled to a scanning electron microscope (SEM) to realize one of the most powerful tools available in the field of nanotechnology.

In Section 2 we will give an account of the main elements which build-up the FIB, namely an ion source and a set of lenses and scanning coils used to produce a finely focused ion spot which can be rastered and

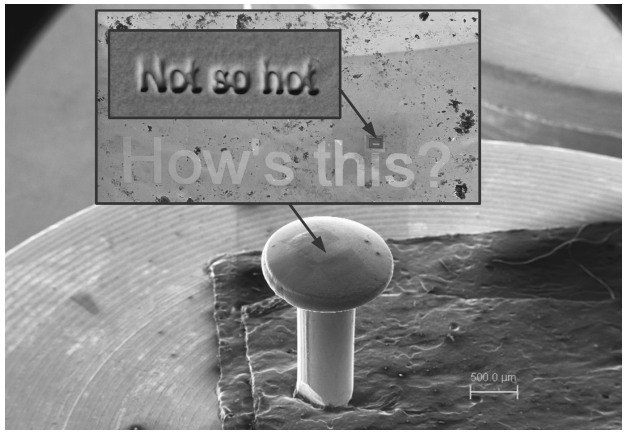


**Figure 1:** Feynman's experiment: "High school competition". The "o" letters in the smallest box have an internal diameter less than 400 nm.
**Slika 1:** Feynmannov eksperiment: "Tekmovanje visoke šole". Notranji premer majhnih črk o v majhnem okvirju je manjši od 400 nm.

pointed in the desired position to form images of the sample or mill specified shapes on it. In Section 3 we briefly describe the complexity of ion-solid interactions which for example allow the processes of sputtering and secondary electron emission (plus a plenty of other physical effects) used in the instrument operation. Finally, in Section 4 a sample of typical application will be described.

The aim of this paper is not to give an exhaustive description of the physics and the technology of focused ion beams, but rather to provide a fast introduction with mention to recent applications. For complete descriptions of the topic Refs. [2–5].

## 2 THE FOCUSED ION BEAM

The most important characteristic usually required to a FIB is the capability to mill very precise shapes in samples. This operation is performed by focusing in a very small spot the ions and moving this spot to the position where this localized sputtering is required. This is achieved through an ion source and an ion column where a set of lenses and scan coils are housed.

The performances that can be obtained in this "primary" task are first of all related to the spot size, the intensity and the stability of the beam. In principle the smallest and most intense is the ion spot, the most precise and fastest will be the job. In practice, limitations in the maximum removal rate that can be achieved may occur as effect of unwanted phenomena like redeposition [4], but this will be considered later.

### *2.1 The ion source*

Like in optical systems, the fundamental ingredient to get a small and intense spot is a *bright source*, where the brightness is defined [7] as the differential current intensity $d^2I$ emitted by the surface element $dA$ of the source into the solid angle $d\Omega$, i. e. $B = d^2I/dA d\Omega$.

The most efficient and practical way to satisfy the requirement of a high brightness is through the so called *Liquid Metal Ion Sources* (LMIS). LMIS are nowadays the common choice for general purpose instruments, where no special demand exists for the ion species and we will limit our description to instruments were this solution is adopted.

In a liquid metal ion source, a field emitter (typically a tungsten needle with a tip radius of a few microns) is connected to a reservoir containing a liquid metal (or alloy). A heating system is provided for the reservoir if the chosen metal is not liquid at the temperature of operation. The metal, which can flow to the emitter, need to be a wetting liquid. In this case, if a voltage (the *extraction voltage*) of the order of 1 kV is applied by a nearby electrode the liquid assumes a conical shape which is the equilibrium configuration under the competing forces produced by the surface tension and the electrostatic field. In an ideal situation, where no further effect would occur, it has been shown [8] that an ideal cone with a half angle of 49.3° (called a "Taylor cone") would be created. In practice, the liquid cone is pulled by the electrostatic field until its end radius $R$ reaches a value small enough to have an electric field that can start field evaporation [9] in proximity of the tip. In this situation any further reduction in the tip radius is inhibited and it has been shown [10] that the cone apex takes a rounded shape with $R \approx 1$–$10$ nm.

According this scheme, ion sources of Ga, Au, Si, Pd, B, P, As, Cu, Ge, Fe, In, U, Be, Cs, Li , Pb, etc. have been produced with brightness $B \approx 10^6$ A/cm$^2$ sr.

Particularly relevant is the implementation of the Gallium LMIS, which is currently the most common choice in commercial instruments. The reasons for this choice are manifold: the low melting temperature (29.8 °C) is certainly fundamental, since it simplify the system and prevent or reduce chemical and physical interactions between the liquid metal and the field emitter. Gallium atomic mass (69.72) has an "intermediate" value between light and heavy elements; this makes gallium ions suitable for efficient sputtering with a wide choice of substrates (the maximum energy transfer in a scattering event occurs when the target and the projectile have the same mass). Its physical properties like surface tension, vapour pressure and vacuum properties maximize the source lifetime. Overall gun performances have been demonstrated to be excellent with respect characteristics like angular intensity and energy spread.

### *2.2 The column*

Although the mechanism of field evaporation is possible only for a very small $R$, the effective source size results to be much larger due to space-charge effects. In practice a virtual source size of the order of 50–100 nm has been estimated [11].

To reach a probe size on the sample of the order of 10 nm or less the image of the source need to be demagnified. This and other similar tasks are performed by the ion column. We will not enter into the details of this part of the instrument since the argument is mostly technical, but we will limit to a functional description of its components.

After being generated in the gun, ions are accelerated down the column by a voltage typically chosen in the range 5–50 kV. The optical system therein contained is usually composed by two electrostatic lenses. The choice of electrostatic lenses rather than electromagnetic ones like in SEM columns, is due to the fact that ions are much massive than electrons. This implies that if accelerated at the same energy, ions are much slower and thus the magnetic part of the Lorentz force is by far weaker.

The first element of a two lens system is the condenser whose function is to "collect" the ions and to set a suitable divergence for the beam before it passes

the forming aperture. The apertures shape the probe and reduce the current. In this way a range of different probe currents can be selected by changing the aperture (and eventually the condenser voltage). Typically the current intensity can be chosen from a few picoamps to a few tenths of nanoamps. The lens that follows is the objective lens that focus the beam on the sample.

Further elements contained in the column are a deflection/astigmatism unit and a fast beam blanker used for raster and mill operation.

### *2.3 Dual-beam instruments*

As we will describe in Sec. 3, the ion-solid interaction is a quite a complicated process and the intuitive concept of a nano-mill for the FIB is valid only in a very rough approximation.

In practice, the result of even very simple operations like milling a square hole in a flat sample can give unexpected results as shown in **Figure 2**. For "unique" samples this can be a question of great concern for the operator which is responsible for analysis that cannot be repeated. The best solution to this problem has been to provide the way to have real-time visual inspection on how the work is advancing. The technical implementation of this solution are dual-beam instruments, where a SEM can operate simultaneously with the FIB.

In standard dual-beam instruments the electronic column enter vertically the high vacuum chamber where the sample is placed, while the FIB column axis has some angle with respect to the SEM, typically around 50°. In **Figure 3** the interior of a dual-beam instrument is shown, where the vertical electron column and the 54° tilted ion column can be seen.

The capabilities of this workstation can be further increased to make it become a complete nano-factory by

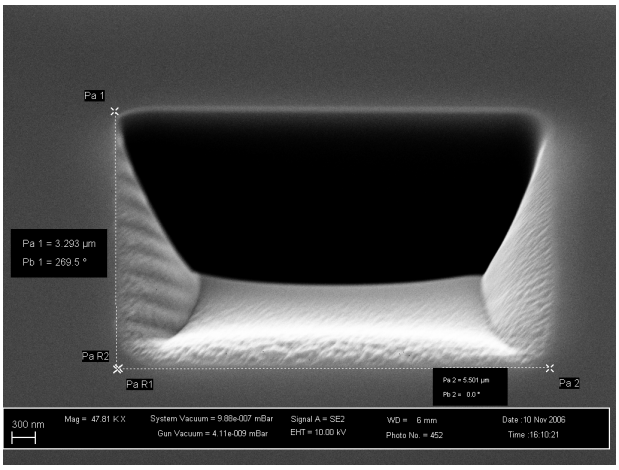


**Figure 2:** Effects of redeposition: the milling process had been set to produce vertical walls, but the final result shows a "mild" slope on the side milled first.

**Slika 2:** Učinek redepozicije: proces obdelave je bil nastavljen za izdelavo pokončnih sten, končni rezultat pa je majhen naklon stene, ki je bila izdelana najprej.

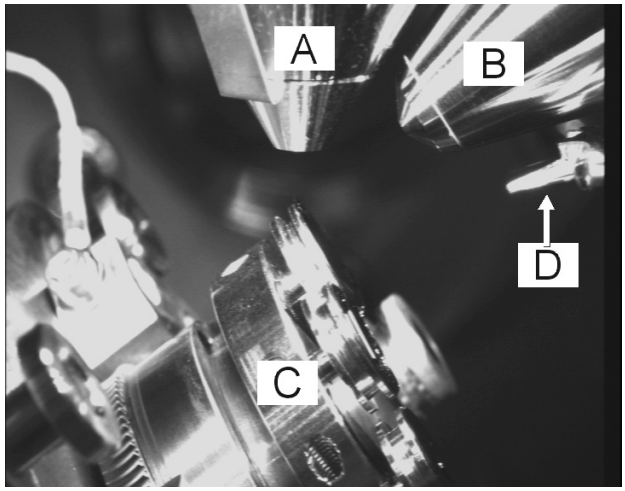


**Figure 3:** Interior of the sample chamber of a dual beam instrument. A: SEM, B: FIB, C: sample stage, D: GIS.

**Slika 3:** Notranjost komore za vzorec pri napravi z dvojnim curkom. A: SEM, B: FIB, C: mizica z vzorcem, D: GIS

equipping the FIB with a *Gas Injections System* (GIS) and micro-manipulators and eventually the SEM with an analytical tool like an EDS (*Energy Dispersive X-Ray Spectroscopy*) system or a WDS (*Wavelength Dispersive X-Ray Spectroscopy*) system [12].

The GIS is a mechanical arm inside the sample chamber ending with capillaries connected by valves to external reservoirs where different gas species can be contained. By placing these capillaries very close to the sample and opening one of the valves, the pressure can be locally increased without perturbing excessively the high vacuum condition needed for FIB and SEM operation. The gas injected in the chamber adsorbs on the sample surface. The molecules in this weak bond state can be broken by the ion beam impinging on the surface. Depending on the adsorbed gas, different processes can occur. If the gas is a precursor of some element or chemical compound, a part of the molecule becomes chemically bond to the substrate while the other part is removed by the pumping system. In this way, precise local deposition of metals like Au, Pt, W etc., or insulators like $SiO_2$ can be realized. Other precursor can instead be injected to enhance or make selective the ion etching process.

Micro-manipulators inside the sample chamber can be used to move portions of the sample extracted by using the FIB. A typical task is the preparation of lamellae for Transmission Electron Microscopy (TEM). In other cases they can be used like electrical probes for conductivity measurement during the work session.

Analytical tools provide a way to establish the chemical composition of the sample. In conjunction with the FIB capability to realize sections, these systems literally acquire a third dimension making it possible a volumetric mapping of chemical species in the sample.

## 3 ION-SOLID INTERACTIONS

It has already been mentioned that the most important operation that can be realized by a FIB is a spatially selective removal of atoms from the sample. From a general point of view, this process is called *sputtering* and has been studied in detail in a fundamental paper by Sigmund [13].

One of the initial observations reported by Sigmund is that it is unlikely for the first collision of the ion to produce a sputtered atom, since the transferred momentum (at least for normal incidence) has a component in the direction entering the surface.

On the contrary sputtering is one of the results of the so called "collision cascade" initiated by the ion entering the sample. This ion undergoes a series of collisions in the target and each atom which acquires sufficient kinetic energy by this collision can initiate a new series of collisions.

The physics of the collision cascade is complex and not fully understood. Moreover it cannot uniquely be defined since the open scattering channels can be different for different energy of the primary beam. We will limit our considerations to a very schematic classification.

A fundamental division of the processes that take place during a collision cascade is between elastic and inelastic events. Elastic processes are responsible for displacement of lattice atoms, defects generation (*amorphization*) and sputtering. Inelastic events generate secondary electrons, X-rays, photoluminescence and phonons (heat). From the point of view of the incident ion, each event causes a transfer of energy to the solid (a speed reduction) and a deviation from the direction taken after the previous collision. At end (when and if the initial ion kinetic energy is not sufficient to make it move freely in the solid) the ion can stop in the sample (*implantation*) if the random deviations occurred did not bring it again to the surface with enough energy to escape in the vacuum (*backscattering*). The energy losses can occur in "nuclear channels" with elastic events (for typical FIB energies mostly by screened Coulomb scattering) and in "electronic channels" where inelastic interaction with lattice electrons produce excitation and ionization.

Aside from sputtering, among the processes described, secondary electron generation is the most important. By utilizing the SEM detectors is in fact possible to generate images also with the FIB.

The resulting images can show contrast mechanism (like the contrast for the local crystallographic orientation) that are not present when an electron primary beam is used. On the other hand, this imaging mode suffer from a continuous modification of the sample due to the contemporaneous occurrence of sputtering events.

The processes described above are fundamental in nature. The actual phenomenology can be sometimes unexpected for the presence of further mechanisms. We describe briefly three of these mechanisms that can pose some limitation or at least make more complex the process of milling.

### *3.1 Redeposition*

Atoms removed by sputtering or backscattered ions can actually fail to "escape" from the solid and instead they can deposit on the surface of the sample very close to the milling site. The effect is a degradation in the quality of the milling operation that can easily reach unacceptable levels as shown in **Figure 2**. This effect is more pronounced when trying to mill high aspect ratio features and when using high ion fluxes. Possible solution are the reduction of the current and/or the dwell time at the expenses of a longer process time. A different solution is the introduction through the GIS of a reactive gas like F, which binds to the sputtered atoms and facilitate the removal by the pumping system.

### *3.2 Channelling*

Channelling occurs in crystalline material and is an apparent inhomogeneity of the sputtering yield across a chemically homogenous surface (**Figure 5**). It is due to the lower atom density along low index directions, resulting in a lower probability for the incident ion to hit a target ion.

### *3.3 Auto-organization*

Off-normal incidence of the primary beam can make evident the effects of the instability generated by the dependence on the local curvature of the sputtering yield [14–18]. Since the erosion rate in depressions is larger than on surface mounds, any surface deviation from flatness tend to be amplified. The presence of a competing smoothing force due to surface atom diffusion produces typical structures showing long-range correlations. Easy to observe are wavelike structures usually indicated as ripples. In conventional milling processes the generation of these structures does not have particular relevance as long as height corrugations of the order of $\approx$10 nm can be neglected.

## 4 APPLICATIONS

The FIB has reached a relatively large diffusion thanks to its application in microelectronic industry started in the 1980s. The capability to remove or add atoms in selected sites with submicron precision makes the FIB an instrument which can hardly be replaced in applications like failure analysis, mask and integrated circuit (IC) repair. A classical example is the inspection of a buried IC, where conventional techniques employing mechanical tools to reveal the hidden parts can introduce artefacts that cannot be tolerated if resolution in the nanometre range is required.

As the diffusion in industry increased, in the 1990s, FIB systems started to be acquired by research labs: one fundamental application became the preparation of TEM cross-section lamellae. In this case several advantages can be indicated with respect to traditional techniques like the use of a ultramicrotome. First of all FIB preparation is site-specific: the lamella can be extracted from a selected location in the sample. This possibility is fundamental for structured samples as in the case of biological specimens. Then, in general, a fewer artefacts are introduced above all when dealing with samples showing a non-homogeneous hardness across the section or with very soft materials.

A further well-established application of the FIB is direct three-dimensional micro and nano-machining. These capabilities have used for MEMS (Micro-Electro-Mechanical Systems) and photonics structures realizations both in processes where only the FIB is used for rapid prototyping and in situation where finer details are added to classical lithography works.

Since all these topics are widely covered in the literature, in the remaining part of this paper we will consider relatively new applications like the production of solid-state nanopores, and the study of ion-induce self-organization processes.

They can serve as examples for two different ways to go beyond established limits of state-of-the art FIB instruments.

### *4.1 Production of solid-state nanopores*

Nanopores produced in solid state membranes have been proposed as the key element for a new class of devices deputed to fast DNA sequencing or (in a more general case) characterization (see [19] and references therein contained).

In the basic set-up, an insulating membrane where a hole with size in the 1–10 nm range has been drilled, separates in two part a reservoir containing an ionic solution. By placing an electrode in each part and by establishing a voltage bias between the two regions, a ionic current starts to flow across the pore. If DNA molecules are inserted in the negatively biased region, they will tend to go through the pore and during the translocation a variation in the ionic current is expected. In principle, for pores small enough, it should be possible associate the instantaneous current variation to the single base which is occupying the pore in that instant. Variant of this scheme have been proposed, but all of them require an insulating membrane with a pore that is comparable in size with single-stranded DNA, i. e. a few nanometres in diameter.

Classical lithographic techniques do not have sufficient resolution to be used in nanopores production, and, in this case, even the FIB can not perform the task directly. It has been reported in several papers a minimum reproducible size for FIB drilled pores in typical $Si_3N_4$ or $SiO_2$ membranes ($\approx$100 nm thick) of about 30 nm. Techniques like *nano-sculpting* [20] and high energy electron irradiation [21–23] have been proposed and an effective shrinkage to the desired size has been demonstrated.

In the first case, a $SiO_2$ membrane, where pores with a diameter of $\approx$50 nm have been realized by using a FIB, is irradiated with a broad 3 keV $Ar^+$ beam. Under this irradiation, a gradual closure occurs as can be deduced from real time measurement of the transmitted ion current and final size less than 1 nm can be achieved. The process is explained through a model where adatoms (surface-diffusing mobile species), created by the incident beam, diffuse to the pore and fill it in.

In the second case pores of similar initial size are produced by electron-beam lithography and plasma etching in a $SiO_2$ membrane. Subsequent exposure to 300 keV electrons in a TEM reduces the size in a controllable way, with a precision of 0.2 nm (resizing occurs while imaging and this allows to follow the process). The claimed mechanism is a fluidization of the $SiO_2$ under

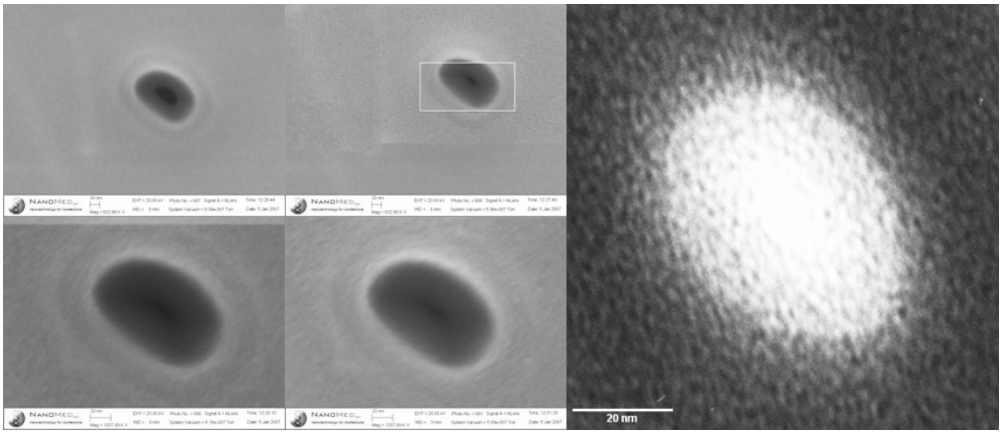


**Figure 4:** Sequence showing shrinkage of a solid state nanopore in $Si_3N_4$ under electron irradiation. In the last tab an ex-situ acquired TEM micrograph shows a final size smaller than 10 nm.

**Slika 4:** Sekvence kažejo krčenje nanopore v $Si_3N_4$ pri obsevanju z elektroni. Zadnji TEM-posnetek prikazuje, da je končna velikost manjša od 10 nm.

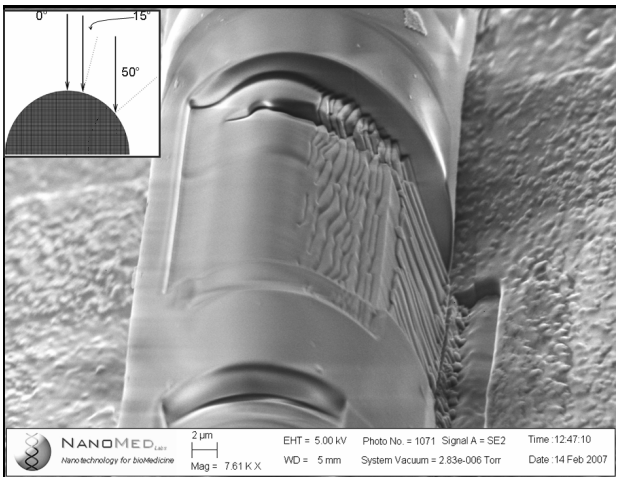


**Figure 5:** Ripple formation on a silicate bio-structure (spicule). The ion beam is orthogonal to the sample holder, but due to the cylindrical shape of the sample, its incidence angle increases with the radius. Ripple rotation for angles closer to grazing incidence appear, as expected from Bradley and Harper theory [14].

**Slika 5:** Nastajanje brazd na silikatni biostrukturi (spicule). Curek ionov je pravokoten na nosilec vzorca, zaradi valjaste oblike vzorca pa vpadni kot raste s premerom. Pojavi se zasuk brazd za kot blizu drsnega, kot napoveduje Bradley-Harperova teorija.

the high energy electron irradiation and a pore shrinkage under the action of surface tension.

Recently a new techniques that can entirely be realized inside a dual-beam instrument has been proposed and the results appear to be interesting. In this case the pore size is reduced during SEM imaging and the shrinking rate can be monitored simply following the image evolution. The resolution of this process is limited by the SEM capabilities to values larger than 1 nm. In **Figure 4** a size reduction sequence is shown. The final size is evaluated ex-situ in a TEM.

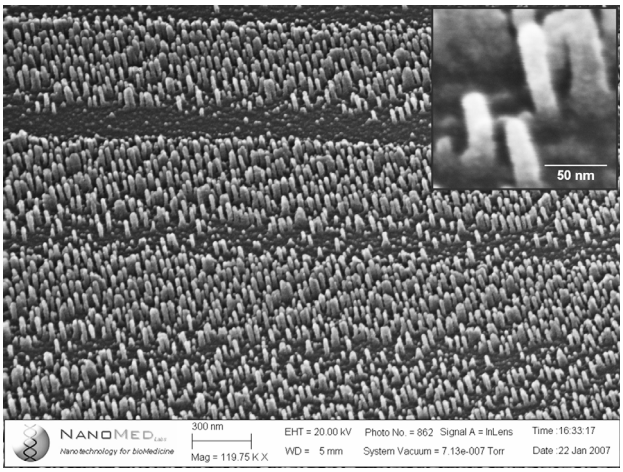


**Figure 6:** Pillar in silicon produced by off-normal incidence with a FIB. In the inset a particular at higher magnification clearly shows that the dimensions of the pillars is beyond FIB resolution.

**Slika 6:** Stolpci na siliciju, doseženi z nenormalno vpadnostjo v FIB. Slika pri veliki povečavi v okvirju prikazuje, da je dimenzija stolpcev pod ločljivostjo FIB.

### *4.2 Nanostructuring by self-organization processes*

The self-organizations processes briefly described in Sec. 3 have been often indicated as a possible high throughput method for nanostructuring surfaces. Recently it has been shown that similar structures can be created also by using the FIB and moreover the long range correlation of this structures can be increased if they are produced on a surface where an ordered template has previously been milled. Although the high throughput characteristic of this technique is lost when the process is realized with a FIB (due to the relative low currents used with respect to broad-beam sources) nevertheless some advantages are obtained. First of all, the possibility to use higher local fluxes allows the exploration of regimes which hardly can be accessed with conventional guns. Then, the self-organization process can be induced with different condition in adjacent regions producing structures of higher complexity. Finally, dual-beam instruments offer the capability of following in a real-time mode the process. This can give the necessary feedback to overcome the lack of knowledge of all the variables entering the self-organization process that influences the capability to predict the final morphology of the surface.

From the point of view of the FIB user, the advantage of this technique is in term of increased resolution in producing particular structures as shown in **Figure 6**. Moreover for particular structures the process time can be greatly reduced.

## 5 CONCLUSION

We have reviewed the main characteristics of Focused Ion Beam technology with particular attention to dual-beam platforms. The applications that we have mentioned demonstrate the widespread diffusion that this kind of instruments have reached, diffusion that goes beyond the fields where the use was initiated, i. e. microelectronic industry. We have finally considered two new research fields where the FIBs can both play a fundamental role and find new ways to go beyond its current limits.

## Acknowledgment

We acknowledge the Italian Ministry for Research (MUR) which funded the NANOMED Project and allowed the acquisition of a state-of-the-art dual-beam instrument.

We also acknowledge Fondazione Carige for funding the cleanroom where the FIB/SEM is located.

## 6 REFERENCES

[1] First published in *Engineering and Science* magazine, XXIII (1960) 5 Available from World Wide Web: http://www.its.caltech.edu/~feynman/plenty.html

[2] J. Orloff, M. Utlaut, L. Swanson, "High Resolution Focused Ion Beams: FIB and Its Applications", Kluwer, New York 2003
[3] J. Meingailis, J. Vac. Sci. Technol. B 5 (**1987**), 468
[4] J. Orloff, Rev. Sci. Instrum. 64 (**1993**), 1105
[5] Introduction to Focused Ion Beams – Instrumentation, Theory, Techniques and Practice, L. Giannuzzi, F. Stevie (eds), Springer, Boston 2005
[6] T. Ishitani, T. Ohnishi, J. Vac. Sci. Technol. A 9 (**1991**), 3084
[7] M Born, E. Wolf, Principles of Optics, Pergamon, Oxford 1991, 6th (corrected) ed.
[8] G. I. Taylor, Proc. R. Sot. London A 280 (**1964**), 383
[9] E. W. Müller Phys. Rev. 102 (**1956**), 618
[10] D. R. Kingham, L. W. Swanson, Vacuum 34 (**1984**), 941
[11] J. W. Ward, J. Vat. Sci. Technol. B 3 (**1985**), 207
[12] J. Goldstein, D. Newbury, D. Joy, C. Lyman, P. Echlin, E. Lifshin, L. Sawyer, J. Michael, Scanning Electron Microscopy and X-Ray Microanalysis, Springer (2003), 3rd ed.
[13] P. Sigmund, Phys. Rev. 184 (**1969**), 383
[14] R. M. Bradley, J. M. E. Harper, J. Vat. Sci. Technol. A 6 (1988), 2390
[15] J. D. Erlebacher, M. J. Aziz, E. Chason, M. Sinclair, J. Florio, Phys. Rev. Lett. 82 (**1999**), 2330
[16] S. Habenicht, Phys. Rev. B 63 (**2001**), 125419
[17] M. A. Makeev, R. Cuerno, A. L. Barabasi, Nucl. Instr and Meth. B 197 (**2002**), 185
[18] U. Valbusa, C. Boragno, F. Buatier de Mongeot, J. Phys. Condens. Matter 14 (**2002**), 8153
[19] C. Dekker, Nature Nanotechnology 2 (**2007**), 209
[20] Li J., Stein D., McMullan C., Branton D., Aziz M. J., Golovchenko J., Nature 412 (**2001**), 166
[21] A. J. Storm, J. H. Chen, X. S. Ling, H.W. Zandbergen, C. Dekker, Nature Materials, 2 (**2003**), 537
[22] H. Chang, S. M. Iqbal, E. A. Stach, A. H. King, N. J. Zaluzec, R. Bashir, Appl. Phys. Lett. 88 (**2006**), 103109
[23] W. M. Zhang, Y. G. Wang, J. Li, J. M. Xue, H. Ji, Q. Ouyang, J. Xu, Y. Zhang, Appl. Phys. Lett. 90 (**2007**), 163102

UDK 050:669.1:6(497.4)
Review article/Pregledni članek

ISSN 1580-2949
MTAEC9, 42(4)151(2008)

# MATERIALS AND TECHNOLOGY: HISTORICAL OVERVIEW

## MATERIALI IN TEHNOLOGIJE: ZGODOVINSKI PREGLED

**Nina Jamar[1], Jana Jamar[2]**

[1]Lipce 10, 4273 Blejska Dobrava, Slovenia
[2]Uredništvo serijske publikacije Materiali in tehnologije, Inštitut za kovinske materiale in tehnologije, Lepi pot 11, 1000 Ljubljana, Slovenia
nina.jamar@telemach.net

*Prejem rokopisa – received: 2008-01-10; sprejem za objavo – accepted for publication: 2008-07-14*

This article describes the evolution of the scientific journal Materials and Technology (Materiali in tehnologije) from its predecessors, the Iron and Steel Journal (Železarski zbornik) and Metals Alloys Technologies (Kovine zlitine tehnologije). We present the statistical data for the journal relating to the years 2000–2006. The article looks at the electronic form of the journal and the influence of online publishing on the recognition and citing of Materials and Technology around the world. We show how the process of publishing the scientific journal takes into account ISO 9000. The article concludes with a description of how Materials and Technology will develop in the future.

Key words: scientific serial publication, Materials and Technology, historical overview, statistical data, electronic publishing, ISO 9000

Članek opisuje razvoj znanstvene serijske publikacije Materiali in tehnologije (Materials and Technology) od njenih predhodnikov, Železarski zbornik (Iron and Steel Journal) in Kovine zlitine tehnologije (Metals Alloys Technologies), do današnjih dni. Predstavljeni so statistični podatki za obdobje od leta 2000 do leta 2006. Opisan je razvoj elektronske oblike serijske publikacije in vpliv elektronskega izdajanja na mednarodno prepoznavnost in citiranje serijske publikacije Materiali in tehnologije. Predstavljen je potek izdajateljske dejavnosti serijske publikacije Materiali in tehnologije po ISO 9000. Članek se končuje z opisom, kako naj bi se serijska publikacija Materiali in tehnologije razvijala v prihodnje.

Ključne besede: znanstvena serijska publikacija, Materiali in tehnologije, zgodovinski pregled, statistični podatki, elektronsko založništvo, ISO 9000

## 1 ŽELEZARSKI ZBORNIK – IRON AND STEEL JOURNAL

The periodic publication the Iron and Steel Journal (Železarski Zbornik) (ISSN 0372-8633) started as a joint project of the Slovenian Ironworks company and the Metallurgical Institute Ljubljana, an independent institution and also the central R&D facility for the company. At that time, in decisions about the development of technology and products, theoretical knowledge was applied to an increasing extent in addition to experience, and at the management level it was considered useful to provide, for people working in R&D, the possibility to exchange ideas and R&D results. At almost the same time, the organisation of the first of annual conferences to provide a platform for oral presentations and discussions about R&D started. The journal was published from 1967 to 1991 as a quarterly, with only three numbers in the first volume. Published articles were classified according to the Universal Decimal Classification and later also using the ASM/SLA Classification. The abstracts were published in English and German, and from 1968 also in Russian. By 1975 the journal started to print authors' abstracts in Slovenian, German, English and Russian. Starting with Volume 2, the Annual Chronological Index was published in the last number of each volume or in the first issue of the next volume.

## 2 KOVINE ZLITINE TEHNOLOGIJE – METALS ALLOYS TECHNOLOGIES

In 1992 the Iron and Steel Journal (Železarski zbornik) changed its name to Metals Alloys Technologies (Kovine Zlitine Tehnologije) (ISSN 1318-0010). The name was changed to better cover the topics of the published articles, which had broadened from topics related to iron and steel to other metallic alloys as well as inorganic materials, polymers, and materials that are used in vacuum technology. A similar evolution took place in some western countries, e.g., in Great Britain the name of the journal Acta metallurgica was changed to Acta materialia, and in Germany the name Zeitschrift für Metallkunde was changed to Zeitshcrift für Materialkunde. Four issues per volume of Metals Alloys Technologies were published up to 1995, and six issues per volume were published from 1996 on. The manuscripts were submitted for publication from authors from Slovenia and abroad. The Annual Index, which included the chronological, authors' and subject index, was added to the last issue of the year. At the request of an industrial society, in 1997 a special number was published.

The role of the publisher was assumed by the Institute of Metals and Technology, and several institutions and industrial companies were brought in as associate publishers to provide a broader base. The

associate publishers were the companies ACRONI Jesenice, IMPOL Slovenska Bistrica, Slovenia steelworks, Metal Ravne, Talum Kidričevo, the National Institute of Chemistry, Institute "Jožef Stefan", the Faculty of Mechanical Engineering, and the Slovenian Society of Tribology. The Ministry for Science and Technology of the Republic of Slovenia (now the Ministry of Higher Education, Science and Technology of the Republic of Slovenia) funded some of the publishing expenses. The content was original scientific and professional contributions, review articles and expanded texts based on communications presented at the annual Conference on Materials and Technology.

All the articles were published according to international ISO standards (ISO 8, ISO 18, ISO 214, ISO 215, ISO 690, ISO 690-2, ISO 832, ISO 999, ISO 2145, ISO 3297, ISO 5122, ISO 8459/1-5) and in line with the Instructions of the Slovenian Research Agency (SIST ISO 4, SISI ISO 8, SIST ISO 215, SIST ISO 214, SIST ISO 18, SIST ISO 690-2, SISI ISO 999, SIST ISO 2145, SIST ISO 5122). These instructions required ISSN, standard terminology, international measures and units, abstract, keywords, the beginning of the article on the odd page, and also the data on the author and the periodical publication had to be presented on the same page. Titles, abstracts and keywords were, for all articles, published in Slovenian and English. Since 1998 the date of receipt of the manuscript and the date of acceptance of the article for publication have also been published.

At the suggestion of the Ministry for Science and Technology of the Republic of Slovenia, in 1998 the editorship of the journal started to categorize and arrange the published articles according to the recommendations of the typology for guiding bibliographies and the entry of data in COBISS Slovenia (Cooperative Online Bibliographic Systems and Services). Between 1996 and 1999, 436 entries in COBISS for the articles were made for articles published in previous years.

In bibliometric analysis and a comparison of the Iron and Steel Journal (Železarski Zbornik) and Metals Alloys Technologies (Kovine Zlitine Tehnologije) 1996/97 several parameters were used for the comparison, for example:

- the number of authors of each article and the number of institutions from which the authors came,
- the breadth of the contents base,
- the shift from a professional publication to a scientific periodical publication.

The results of the analysis showed a significant improvement of the journal Metals Alloys Technologies (Kovine Zlitine Technologije) in terms of originality, quality and the presentation of topics, as well as the regularity of publishing. The improvement was due to three factors: better knowledge and experience of the domestic authors, the increasing share of authors from abroad, and the publishing of topics on a wide range of materials as well as phenomena and processes.[1]

## 3 MATERIALS AND TECHNOLOGY – MATERIALI IN TEHNOLOGIJE

In 2000 a new name, Materials and Technology (Materiali in tehnologije) (ISSN 1580-2949), was given to the journal and a new editorial board was selected, although the editors were not changed. The content was broadened to cover articles dealing with topics from a wide range of materials, such as metals and alloys, polymers, inorganic and vacuum materials, their testing and characterisation, development, manufacturing, processing and application for engineering structures. Also, articles on new developments in composites were published. The journal became the leading periodical publication in the field of materials in Slovenia. The topics published justified the change of the journal's name, and this change attracted authors from other scientific disciplines, especially solid-state physics. The future aims of the journal are to achieve a higher international recognition and an appropriate citation index. Only by a continuous improvement in quality, which is related to the striving for greater originality and quality of the published works and the attraction of new, younger authors, especially from foreign countries, will an appropriate indexing in the Science Citation Index be achieved. This will attract new authors, Slovenian and foreign, who are to a large extent currently submitting their papers for publication in foreign journals. Six issues were published per volume, and double issues have not been published in the past two years. The sixth and last issue in the volume also includes the Annual Index: chronological, authors and subject index.

During the 35$^{th}$ year of publication of the journal Materials and Technology – Materiali in Tehnologije in 2001, a bibliometric-bibliographic comparison of the journals Materials and Technology (2000) and Materials Science and Technology (2000) was done. It should be emphasized that Materials science and Technology is an international journal with the impact factor. The results have shown that there are no significant differences between the journals. The only noticeable difference is in the number of cited (and listed) sources. But when we are talking about the sources of references and about the age of the cited sources there are no significant differences. The finding that there are no significant differences between journals opens a lot of questions concerning international and local journals.[2]

The articles from periodical publication Materiali in tehnologije / Materials and Technology were till 2007/1 indexed in nine international secondary publications and databases:

- Metals Abstracts, Engineered Materials Abstracts, Business Alert Abstracts (Steels, Nonferrous, Polymers, Ceramics, Composites), Chemical Abstracts, Aluminium Industry Abstracts, Referativnyj žurnal Metallurgija, Metadex, Inside Conferences, and DOMA, and since 2007/1 also in:

- DOAJ (Directory of Open Access Journals), GOOGLE SCHOLAR and SCIRUS.

**We are pleased to inform that Materiali in Tehnologije has been selected for coverage in Thomson Reuters products and custom information services. Beginning with vol. 41 (1) 2007, this publication is indexed and abstracted in the following:**

- **Science Citation Index Expanded (also known as SciSearch®)**
- **Materials Science Citation Index**
- **JournalCitations Reports / Science Edition**

**In the future Materiali in Tehnologije may be evaluated and included in additional Thomson Reuters products and information services to meet the needs of the scientific and scholarly research community.**

The process of publishing Materials and Technology is in accordance with ISO 9000 **(Diagram 1)**.

**Table 1:** Typology of articles (1967–2006)
**Tabela 1:** Tipologija člankov (1967–2006)

| Typology of articles | Number | % |
|---|---|---|
| Review scientific articles | 121 | 6.66 |
| Original scientific articles | 984 | 54.19 |
| Professional articles | 600 | 33.03 |
| Technical news | 86 | 4.74 |
| Other | 25 | 1.38 |
| Together | 1816 | 100.00 |

During the 40th year of publication, in 2007, a Special Issue of the journal Materials and Technology – Materiali in Tehnologije "The Bibliography of the articles 1967–2006" was published.

The post office issued a stamp "40 years of publishing of the periodical publication Materials and Technology" to mark the anniversary of the journal. The anniversary was also marked by the entering in COBISS (www.cobiss.si) all articles (1816) published in the journal and its predecessors in the years 1967 to 2007.

### *3.1 Statistical data on Materials and Technology – Materiali in Tehnologije: 2000–2006*

**Table 2:** Number of issues, pages and articles
**Tabela 2:** Fizični obseg

| Issue | Pages | Articles |
|---|---|---|
| 2000 / 1–6 | 452 | 79 |
| 2001 / 1–6 | 500 | 72 |
| 2002 / 1–6 | 492 | 71 |
| 2003 / 1–6 | 420 | 67 |
| 2004 / 1–6 + special number | 491 | 67 |
| 2005 / 1-6 | 334 | 30 |
| 2006 / 1-6 | 354 | 44 |
| Total | 3043 | 430 |

**Table 3:** Share of scientific versus professional articles
**Tabela 3:** Razmerje med objavljenimi znanstvenimi in strokovnimi članki

| Year | Professional % | Scientific % |
|---|---|---|
| 2000 | 38.00 | 62.00 |
| 2001 | 33.00 | 67.00 |
| 2002 | 21.00 | 79.00 |
| 2003 | 36.00 | 64.00 |
| 2004 | 28.35 | 71.65 |
| 2005 | 26.70 | 73.30 |
| 2006 | 13.65 | 86.35 |

**Table 4:** Language of publishing
**Tabela 4:** Jezik člankov

| Year | Slovenian % | English % |
|---|---|---|
| 2000 | 84.80 | 15.20 |
| 2001 | 72.20 | 27.80 |
| 2002 | 69.00 | 31.00 |
| 2003 | 58.00 | 42.00 |
| 2004 | 53.75 | 46.25 |
| 2005 | 31.70 | 68.30 |
| 2006 | 20.45 | 79.55 |

**Table 5:** Authors
**Tabela 5:** Analiza po avtorjih

| Year | All authors | Articles | Authors / article |
|---|---|---|---|
| 2000 | 222 | 79 | 3 |
| 2001 | 222 | 72 | 3 |
| 2002 | 216 | 71 | 3 |
| 2003 | 194 | 67 | 3 |
| 2004 | 243 | 67 | 4 |
| 2005 | 109 | 30 | 4 |
| 2006 | 147 | 44 | 3 |

**Table 6:** Nationality of authors
**Tabela 6:** Mednarodnost avtorjev

| Year | Slovenia % | Foreign countries % |
|---|---|---|
| 2000 | 85.10 | 14.90 |
| 2001 | 85.10 | 14.80 |
| 2002 | 80.10 | 19.90 |
| 2003 | 73.20 | 26.80 |
| 2004 | 62.15 | 37.85 |
| 2005 | 69.70 | 30.30 |
| 2006 | 52.40 | 47.60 |

**Table 7:** Subject area
**Tabela 7:** Vsebinski pregled člankov

| Scientific field | 2000 | 2001 | 2002 | 2003 | 2004 | 2005 | 2006 |
|---|---|---|---|---|---|---|---|
| Metallic materials | 51.90 | 68.10 | 71.85 | 67.15 | 71.70 | 70.00 | 68.20 |
| Inorganic materials | 31.60 | 11.10 | 12.65 | 7.45 | 11.95 | 23.30 | 9.10 |
| Vacuum technology | 8.90 | 12.50 | 7.00 | 10.45 | 7.45 | 0.00 | 4.55 |
| Polymers | 6.30 | 6.90 | 7.05 | 3.00 | 3.00 | 3.35 | 13.60 |
| Building materials | 0.00 | 0.00 | 0.00 | 7.45 | 5.95 | 3.35 | 4.55 |
| Information science | 1.26 | 0.00 | 1.40 | 0.00 | 0.00 | 0.00 | 0.00 |
| Research policy | 0.00 | 1.40 | 0.00 | 0.00 | 0.00 | 0.00 | 0.00 |
| Research and development | 0.00 | 0.00 | 0.00 | 1.50 | 0.00 | 0.00 | 0.00 |
| Standardization | 0.00 | 0.00 | 0.00 | 1.50 | 0.00 | 0.00 | 0.00 |
| Methodology | 0.00 | 0.00 | 0.00 | 1.50 | 0.00 | 0.00 | 0.00 |

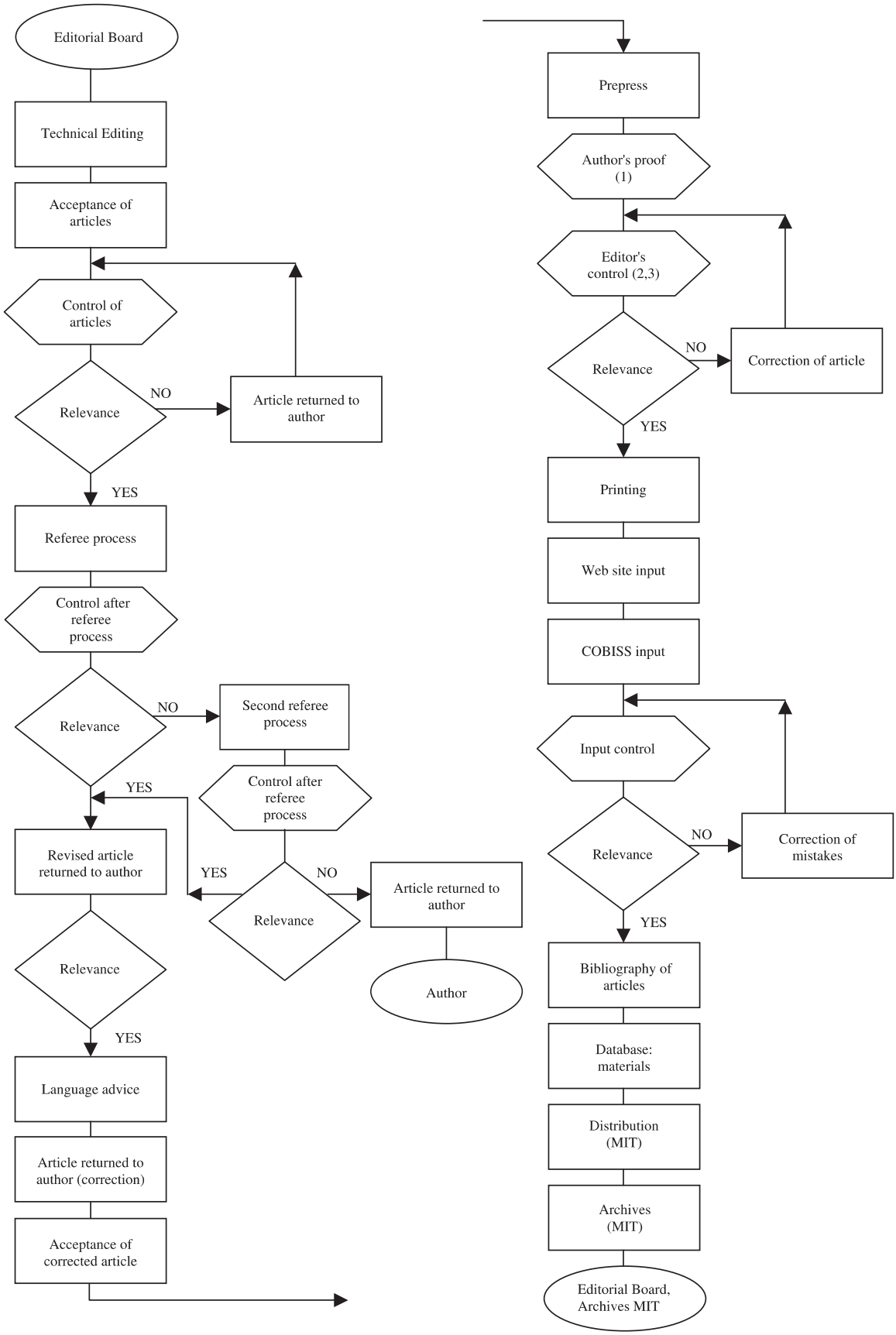


**Diagram 1:** The process of publishing Materials and Technology in accordance with ISO 9000
**Diagram 1:** Potek izdajateljske dejavnosti serijske publikacije Materiali in tehnologije po ISO 9000

**Table 8:** References quoted
**Tabela 8:** Citiranje literature

| Number of articles with references quoted (%) | | | | | | | |
|---|---|---|---|---|---|---|---|
| Number of references | 0 | 1–4 | 5–9 | 10–14 | 15–19 | 20–29 | 30 and more |
| Year | | | | | | | |
| 2000 | 1.27 | 15.19 | 39.24 | 26.58 | 8.86 | 7.59 | 1.27 |
| 2001 | 0.00 | 13.88 | 40.28 | 23.61 | 6.95 | 12.50 | 2.78 |
| 2002 | 0.00 | 11.30 | 33.80 | 28.15 | 12.70 | 11.25 | 2.80 |
| 2003 | 1.50 | 14.90 | 41.80 | 26.90 | 3.00 | 5.95 | 5.95 |
| 2004 | 1.50 | 10.45 | 43.25 | 22.35 | 14.95 | 6.00 | 1.50 |
| 2005 | 0.00 | 3.35 | 50.00 | 16.65 | 13.35 | 6.65 | 10.00 |
| 2006 | 0.00 | 18.18 | 34.10 | 22.72 | 13.63 | 4.54 | 6.81 |

**Table 9:** Average citations per article
**Tabela 9:** Povprečno število citatov na članek

| Year | Citations | Articles | Articles without citations | Citations / article |
|---|---|---|---|---|
| 2000 | 797 | 79 | 1 | 10.10 |
| 2001 | 807 | 72 | 0 | 11.20 |
| 2002 | 848 | 71 | 0 | 11.95 |
| 2003 | 775 | 67 | 1 | 11.55 |
| 2004 | 734 | 67 | 0 | 10.95 |
| 2005 | 530 | 30 | 0 | 18.30 |
| 2006 | 576 | 44 | 0 | 13.10 |

Based on the statistical data, the following findings should be emphasized **(Tables 2–9)**:

- the number of articles decreased from 79 articles in 2000 to 44 articles in 2006. This is in part due to the decrease in the R&D activity after the independence of Slovenia and in part due to the devaluation of articles published in Slovenian journals,
- the number of scientific articles increased in relation to professional articles from 62 % in 2000 to 86 % in 2006, an indication of the improved average originality and scientific value of the presented topics,
- the number of articles published in English has increased very considerably, from 15.20 % in 2000 to 79.55 % in 2006, as a direct consequence of the official underrating of the use of Slovenian for publishing articles on topics related to technical aspects, technology and natural sciences,
- the share of international authors increased very substantially, from 14.90 % in 2000 to 47.60 % in 2006,
- the average number of references quoted per article published has increased slightly, from 10.10 in 2000 to 13.10 in 2006.

### *3.2 Access in electronic form*

In electronic form the journals Metals Alloys Technology – Kovine Zlitine Tehnologije and Materials and Technology – Materiali in Tehnologije were initially accessible at the following URL: http://www.imt.si/materiali-tehnologije (ISSN 1580-3414).

The idea of the digitalisation of the journal Metals Alloys Technologies came in 1995. The decision was made for the journal to have a web site for the basic presentation of the journal. The web site was accessed at http://www.ctk.uni-lj.si/kovine/. In the next two years, 1997 and 1998, the newly developed HTML 3.2 and HTML 4 allowed new solutions, while Microsoft Office 97 made possible the very simple transformation of documents from the Office environment to hypertext. As a result, the idea of the electronic publishing of articles in full-text form was revived. The growth of electronic serials with access to the articles in full-text form allowed a comparison between different file types in which the full texts were accessible at web sites. The most interesting for the comparison were the journals on natural sciences and technology because of them having solutions for the graphical elements in the articles, i.e., graphs and figures, and for other difficult text parts, like mathematical derivations and chemical formulae. The web site of the journal was supplemented with a simple search tool for searching on the basis of indexes and hypertext assemblies of articles (data on authors, abstracts in Slovenian and English, key words in Slovenian and English).

With the change of the title Metals Alloys Technologies to Materials and Technology, the web site was given a new form and content. The new URL of the electronic version of the journal is http://www.imt.si/materiali-tehnologije. The web site presented a sort of web portal for the field of natural sciences and technology. The aim of the web site was to achieve the highest data accessibility for a wide circle of users. The web site also enables an interactive attitude between readers and the editorship. With the monitoring of new technologies in electronic publishing as well as with further education, more useful connections with electronic forums and with notifications for the users about the new ways of accessing the data from this field of science (monitoring of the development and accessibility of new databases and standards, notifications about conferences, the possibility for further education, and the monitoring of legislation) it is possible that the web site will be friendly and useful for researchers, students and other.[3]

The advantages of publishing the journal in electronic form are:

- ordering of articles from a simple database allows subject enquiries over the content of the articles,
- simplification of the contacts between the authors and the editorship,
- permanent and simple access to the full text of the articles regardless of the place and time,
- the electronic form can be accessed before the printing of the journal,
- wider impact and visibility in the international community,

- different search options (by indexes, abstracts, keywords),
- possibilities for connections between quoted and other related articles,
- quick accessibility of authors to notifications of the editorship: to instructions for submission of manuscripts and other notifications,
- access and downloading of the full text of the article,
- traceability of the article (history of the article at one point),
- the electronic form is cheaper than the printed form.

### *3.3 Materials and Technology – the future*

- Materials and Technology – Materiali in Tehnologije is the leading periodical publication in the field of materials and composites in Slovenia, and strengthening this position should be the main goal for the Editorial Board in the future.
- The number of articles in English should increase further. However, the activity of maintaining Slovenian as a developed cultural language should not be neglected. For this reason, as the leading periodical publication, in the future articles in Slovenian should also be published. A compromise should be found between the majority of articles published in English, mostly original scientific works, and some of the articles published in Slovenian, probably mostly with authors from industry. The bilingual publishing of all articles depends on the extent of funding.
- The journal covers the fields where figures, microstructures and diagrams are very important, for this reason the editors should conserve the quality of printing at the current level or even improve it.
- The editors should attract more distinguished authors especially from English-speaking countries.
- The number of citations of the journal in prestigious periodical publications should be increased.
- The electronic form of the periodical publication of the journal must maintain its level of quality.
- The electronic version of the journal should exist as a web portal, where the user, in addition to the articles in full-text form, should find information about other services from the scientific fields covered (the catalogue of web connections, news, interesting information and data of interest for scientists).
- The journal should actively take part in the development of a potential information service for Slovenian professional and scientific periodical publication.

## 4 REFERENCES

[1] N. Jamar, M. Baš, P. Južnič, Mater. Tehnol., 34 (**2000**) 1/2, 7–14

[2] P. Južnič, N. Jamar, Mater. Tehnol., 36 (**2002**) 3/4, 169–177

[3] M. Pušnik, The role of special libraries by the acceleration of the social and economic development. Construction of library collections: the acquisition and secretion of the material, Ljubljana, 2000, 163–172

UDK 621.785.5:669.14.018.8
Original scientific article/Izvirni znanstveni članek

ISSN 1580-2949
MTAEC9, 42(4)157(2008)

# LOW ENERGY-HIGH FLUX NITRIDATION OF METAL ALLOYS: MECHANISMS, MICROSTRUCTURES AND HIGH TEMPERATURE OXIDATION BEHAVIOUR

## NITRIRANJE KOVINSKIH ZLITIN S FLUKSOM Z MAJHNO ENERGIJO IN VELIKO GOSTOTO: MEHANIZMI, MIKROSTRUKTURE IN VISOKOTEMPERATURNO OKSIDACIJSKO VEDENJE

**Fernando Pedraza**

Université de La Rochelle. Laboratoire d'Etudes des Matériaux en Milieux Agressifs (LEMMA, EA 3167). Avenue Michel Crépeau, 17042 La Rochelle cedex 01, FRANCE
fpedraza@univ-lr.fr

*Prejem rokopisa – received: 2007-09-17; sprejem za objavo – accepted for publication: 2008-06-07*

Nitridation is typically carried out to improve wear and erosion of different metal and alloy substrates. In the case of "stainless" alloys, the nitridation temperature needs to be lowered to avoid the precipitation of CrN that would reduce the overall corrosion resistance. Low energy – high flux nitridation allows to nitride relatively thick layers in short times at low temperatures depending on the substrate crystal structure and chemical composition as shown for pure Ni, a Ni-20Cr model alloy, a conventional AISI 304L stainless steel and an ODS FeAl intermetallic alloy. The mechanisms of nitridation, the phases and microstructures are discussed in this work with the support of X-ray diffraction, atomic force, scanning and transmission electron microscopy techniques.

The high temperature oxidation behaviour of the nitrided matrices is thereafter evaluated in air and the results are compared to non nitrided specimens. The oxidation kinetics are determined with thermogravimetry and the mechanisms are discussed in light of the oxide phases and microstructures resulting from the previous nitridation treatment. It will be shown that a reduction of the high temperature oxidation resistance occurs for the shortest oxidation times because of trapping of the protective elements.

Key words: nitridation, ion implantation, nitrided layer, austenite alloys, ODS Fe-Al alloys, surface oxidation

Nitriranje poveča obrabno in erozijsko odpornost podlag iz kovin in zlitin. Pri nerjavnih jeklih je treba znižati temperaturo nitriranja, da bi se izognili izločanju CrN, ki bi zmanjšalo splošno korozijsko odpornost. Nitriranje s fluksom z majhno energijo in veliko gostoto omogoča, da se ustvarijo relativno debeli sloji v kratkem času in pri nizki temperaturi, odvisno od mikrostrukture in kemijske sestave podlage, kot je prikazano za čisti Ni, modelno zlitino Ni-Cr20, konvencionalno jeklo AISI 304 L in za intermetalno zlitino FeAl ODS. V tem delu razpravljamo o mehanizmu nitriranja, fazah in mikrostrukturah na temelju rezultatov difrakcije rentgenskega sevanja, opazovanja atomske sile ter vrstične in presevne elektronske mikroskopije.

Ocenili smo visokotemperaturno vedenje nitriranih matic na zraku in ga primerjali z nenitriranimi vzorci. Kinetiko oksidacije smo ugotovili s termogravimetrijo in o rezultatih razpravljamo z upoštevanjem oksidnih faz in mikrostruktur, ki so nastale pri nitriranju. Ugotovili smo, da se zmanjša visokotemperaturna oksidacijska odpornost pri najkrajših časih oksidacije zaradi ujetja varovalnih elementov v pasti.

Ključne besede: nitriranje, ionska implantacija, nitrirana plast, avstenitne zlitine, Fe-Al ODS zlitina, oksidacija površine

## 1 INTRODUCTION

Nitriding of austenitic stainless steels has been extensively studied owing to the significant improvements in surface hardness and tribological behaviour [1] as well as in corrosion resistance [2] so long as precipitation of CrN is avoided [3]. All these improvements obtained at moderate temperature ($T < 450$ °C) seem to be associated with the formation of an interstitial solid solution of nitrogen in the steel matrix: face centred cubic (fcc) $\gamma_N$ or "expanded austenite". Various studies suggest that the $\gamma_N$ would correspond to a fcc phase with a high density of stacking faults likely induced by the internal stresses in the nitrided layer [4-6].

However, the effect of the nitriding process to other alloy systems has been poorly investigated to date. For high temperature applications, Ni-base superalloys are typically employed as they show good corrosion and oxidation resistance and excellent resistance to creep and rupture at high temperatures [7]. However, they exhibit poor wear resistance. Therefore, plasma nitriding studies have been carried out for instance on Inconel 718 (containing the mass fraction of Cr 20 %) at temperatures between 550 °C and 750 °C leading to precipitation of chromium nitride, CrN, and subsequent increase in Knoop hardness [8] and wear resistance until the nitrided layer is worn away [9]. Further studies on plasma assisted nitriding of Inconel 690 (containing the mass fraction of Cr 30 %) have been carried out at temperatures between 300 °C and 400 °C [10] where the different depths of nitrogen diffusion have been related to the grain orientations and the anisotropic dependence of stress on strain [11].

The low energy-high flux nitrogen implantation approach has rarely been addressed. This is also known

as an implantation-diffusion technique at relatively low temperatures to promote nitrogen diffusion while arresting CrN precipitation in stainless steels [5,6,12,13]. Williamson et al. [14] studied a collection of 16 fcc metals nitrided under the same conditions (0.7 keV, 2 mA $cm^{-2}$, 400 °C and 15 min). It was shown that the Ni-rich alloys contained much less nitrogen with correspondingly thinner layers than the Fe-rich alloys. Besides, no nitrogen could be detected in the pure Ni specimens but an isolated diffracted peak corresponding to the $Ni_3N$ phase. The second study dealt with the tribological properties of Inconel 600 (containing the mass fraction of Cr 16 %) in comparison with the AISI 316 stainless steel, both nitrided at 400 °C for 1 h under 1.2 keV and 1 mA $cm^{-2}$ [15]. Again, a thin layer with a maximum concentration of the mole fraction of N 9 % was found in the Ni-rich substrates compared to a 25 at% in the stainless steel, but still offering an increase in hardness and a reduction in wear rate.

Despite the extensive use of Ni base superalloys, their significant weight is a limitation in the aeronautic domain as fuel consumption must be reduced. To this end, various intermetallic alloys based on TiAl and on FeAl represent solid alternatives to replace the heavier Ni superalloys [16]. In these materials, the nitridation of TiAl have received most of the attention concerning the treatment itself [17–19], their corrosion properties [20] or their high temperature behaviour [21–24]. However, little is known on the nitridation of FeAl intermetallic alloys. To the best of our knowledge, only the oxidation kinetics and the likely mechanisms of a nitrided ODS FeAl alloy were reported by Dang et al. [25].

Contrary to most of the studies devoted to wear and erosion, the purpose of this work is to review the mechanisms of nitridation by implantation-diffusion (also called low energy-high flux nitridation) in different model (pure Ni, Ni20Cr), commercial (AISI 304L) and candidate materials (ODS FeAl) and the effect on their high temperature oxidation behaviour. The roles of "physics" (crystal structure, grain orientation) and "chemistry" (alloying elements) will be discussed to elucidate the mechanisms involved upon nitridation. On the basis of the resulting phases and microstructures, the high temperature oxidation behaviour will thereafter be interpreted.

## 2 EXPERIMENTAL

**Table 1** gathers the base composition and crystal structure of the materials of study. The samples consisted of round coupons of varying diameter and 1 mm thick cut from the bars. The main surfaces were mechanically polished to a final roughness of 0.01 μm. They were then ultrasonically degreased in acetone and rinsed in 96 % ethanol.

Low energy – high flux nitrogen ($N_2^+$, $N^+$) implantation was carried out at LMP (Poitiers, France) with a Kaufman type ion source at 1.2 keV and a current density of about 1 mA $cm^{-2}$ for 1 h, corresponding to an estimated dose of about $2.25 \cdot 10^{19}$ $cm^{-2}$. The temperature of the samples was carefully controlled with a thermocouple attached on the back of the samples. Prior to the nitridation treatment, $Ar^+$ sputtering (1.2 keV, 0.5 mA $cm^{-2}$ for 15 min) was carried out on each main coupon face to remove the rigid oxide layer that precludes nitridation [26]. The backing pressure in the chamber upon the nitriding process was better than $10^{-2}$ Pa. Implantation was carried out on both principal coupon faces for the subsequent oxidation experiments, representing about 85 % of the overall surface. Oxidation of the nitrided specimens was conducted in a Setaram TG92 thermobalance of $10^{-6}$ g of accuracy at 800 °C for 24 h under synthetic air. Heating and cooling rates were fixed at 50 °C/min.

**Table 1:** Substrates major composition ($\chi$/%) and the initial crystal structure

**Tabela 1:** Osnovni sestavni elementi v odstotkih in začetna kristalna struktura podlag ODS-zlitine, utrjene z disperzijo oksidov

| substrate | Fe | Cr | Ni | Al | $Y_2O_3$ | matrix |
|---|---|---|---|---|---|---|
| Ni | - | - | ≈ 100 | - | - | fcc |
| Ni20Cr | - | 20 | 80 | - | - | fcc |
| AISI 304L | 70 | 20 | 10 | - | - | fcc |
| ODS* FeAl | 60 | - | - | 38 | 2 | ordered B2 |

* ODS = oxide dispersion strengthened

Thermodynamic calculations have been performed using the HSC Chemistry software [27] to assess the thermodynamically stable compounds expected to form within the different matrices. The calculations have been carried out at equilibrium conditions at $10^{-2}$ Pa (implantation conditions) and at atmospheric pressure (after implantation) disregarding collision cascades and sputtering of the surfaces. Only the gas species $N_2^+$ (g) or $N_2$ (g) have been considered to react with the substrates, thus taking into account the splitting of the molecules into 2 nitrogen atoms and the corresponding energy release.

The characterisation of the implanted and the oxidised specimens was undertaken using contact mode atomic force microscopy (AFM) with an Autoprobe CPR (Veeco Instruments), by X-ray diffraction in a Bruker AXS D-5005 equipment in the $\theta$–$2\theta$ configuration and grazing incidence (GIXRD) using Cu $K_{\alpha 1}$ ($\lambda$ = 0.15406 nm) radiation as well as by scanning electron microscopy (SEM) coupled to energy-dispersive spectrometry (EDS) in a JEOL JSM-4510 LV. Cross sections of the implanted specimens were also prepared for transmission electron microscopy (TEM) studies in a JEOL-JEM 2010 operating at 200 kV. For such purpose, careful mechanical polishing in SiC# 4000 emery paper was performed down to a thickness of about 50 μm. Then, Ar bombardment at 3 keV was carried out in a GATAN PIPS™ (precision ion polishing system) model 691 at

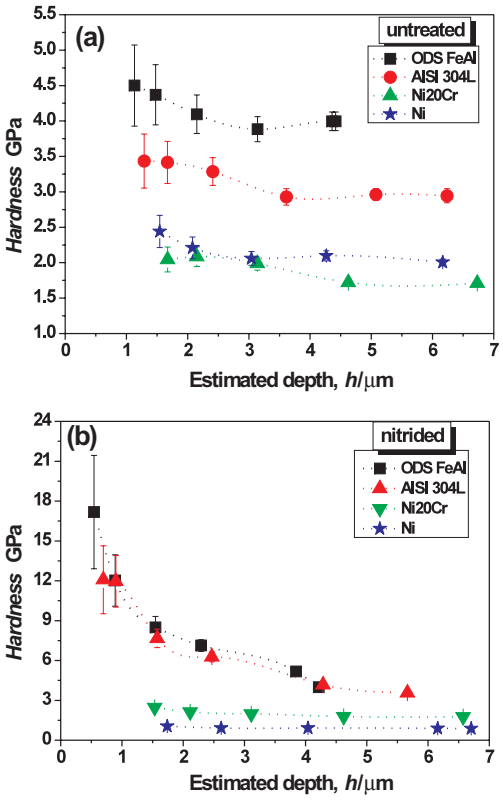


**Figure 1:** Evolution of Vickers microhardness with estimated depth of the (a) untreated specimens and (b) nitrided by implantation-diffusion –NID-

**Slika 1:** Evolucija mikrotrdote po Vickersu z ocenjeno globino; (a) nenitriran vzorec (b) nitriran z ionsko implantacijo in difuzijo – NID

different angles. Vickers microhardness measurements were also performed at increasing loads to get acquainted of the effects of the implantation.

## 3 RESULTS AND DISCUSSION

### *3.1 Nitridation by implantation-diffusion*

After nitridation, all the substrates undergo increased surface microhardness compared to the untreated specimens as depicted in **Figure 1**. In comparison with the untreated specimens, the hardness increase is of about (8, 20, 250 and 280) % for pure Ni, Ni20Cr, AISI 304L and ODS FeAl, respectively. From these results, it can be considered that nitridation does not effectively occur in pure Ni. This can be due to two interconnected mechanisms. The first one is due to the incorporation of N as an interstitial solid solution and/or to the formation of hard metal nitrides, i. e. "structural deformation", i. e. the appearance of harder crystalline phases. The second one is related to an increased plastic deformation typically occurring upon implantation, i. e. "microstructural deformation", i. e. surface roughness.

Regarding the crystallographic phases, the XRD patterns after implantation clearly reveal various features and striking differences among the different substrates as shown in **Figure 2**. In the case of pure Ni [**Figure 2(a)**] the patterns of the untreated and the nitrided specimens are rather similar. Calculations of the lattice parameters of both untreated and nitrided substrates leads to the

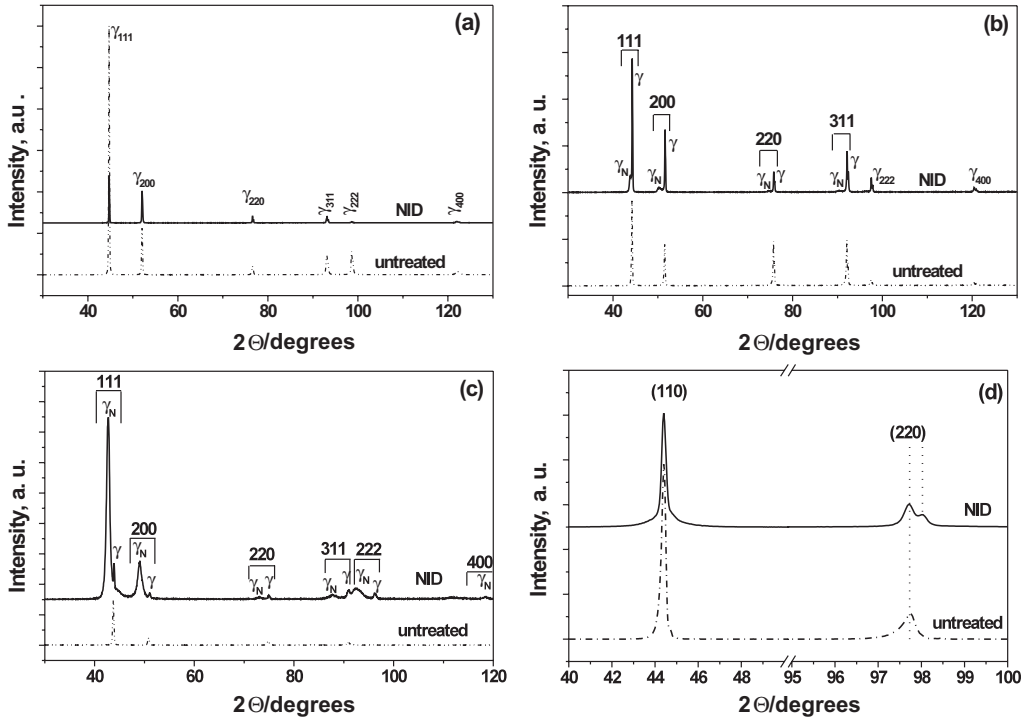


**Figure 2:** X-ray diffraction patterns of the different substrates untreated and nitrided by implantation diffusion –NID- (a) pure Ni, (b) Ni20Cr, (c) AISI 304L and (d) ODS FeAl

**Slika 2:** Diagrami difrakcije rentgenskega sevanja za različne podlage, nenitrirane in nitrirane z implantacijsko difuzijo (NID): (a) čisti Ni, (b) NiCr20, (c) AISI 304 in (d) ODS FeAl

same results ($a_o \approx 0.351$ nm) hence indicating no expansion of the matrix volume. The only remarkable changes involves an attenuation of the <111> directions after nitridation compared to the untreated Ni. Williamson et al. [14] also claimed the absence of $\gamma_N$ peaks in pure Ni at a lower energy and a higher flux than in our studies. However, they observed a hexagonal $Ni_3N$ phase and detected a small shift to lower angles, thus implying retention of a very small amount of nitrogen.

Contrary to pure Ni, the nitrided Ni20Cr and AISI 304L substrates [**Figure 2(b)**] exhibit a fcc $\gamma_N$ phase [28] at lower diffraction angles and the original $\gamma$ phase peaks have shifted towards higher diffraction angles [29]. For the sake of comparison between both implanted Cr-containing substrates a rough estimation of the retained nitrogen has been carried out using the Vegard's law for substitutional solid solution as follows: $a_{\gamma N} = a_\gamma + \alpha \cdot C_N$, where $a_{\gamma N}$ and $a_\gamma$ are the lattice parameters for the N-containing and N-free $\gamma$ phases, respectively, and $\alpha$ is the Vegard's law constant (0.00072 for Fe alloys, also assumed for Ni alloys in this study [14]). The concentration of nitrogen is the mole fraction in $x$(N)%. The results are gathered in **Table 2**.

**Table 2:** Lattice parameters of the N-containing $\gamma_N$ and N-free $\gamma$ austenite phases, the relative expansion induced, and their corresponding average atomic nitrogen contents, $x$(N)%, as a function of the diffraction plane (hkl) in Ni20Cr and AISI 304 L

**Tabela 2:** Mrežni parametri avstenitnih faz $\gamma$-faz z dušikom in brez njega, relativna inducirana razširitev in ustrezna povprečna atomska vsebnost dušika $x$(N)% za različne difrakcijske ravnine (hkl) v Ni20Cr in AISI 304L

| | hkl | 111 | 200 | 220 | 311 |
|---|---|---|---|---|---|
| Ni20Cr | $a_{\gamma N}$/nm | 0.3580 | 0.3637 | 0.3589 | 0.3612 |
| | $a_\gamma$/nm | 0.3538 | 0.3540 | 0.3545 | 0.3548 |
| | expansion/% | 1.2 | 2.8 | 1.2 | 1.8 |
| | $x$(N)/% | ≈6 | 13.5 | 6 | ≈9 |
| AISI 304L | $a_{\gamma N}$/nm | 0.3666 | 0.3716 | 0.3666 | 0.3683 |
| | $a_\gamma$/nm | 0.3572 | 0.3583 | 0.3583 | 0.3583 |
| | expansion/% | 2.6 | 3.7 | 2.3 | 2.7 |
| | $x$(N)/% | 13 | 18.5 | 11.5 | 14 |

**Table 2** shows that the retained amount of nitrogen is highly anisotropic. In Ni20Cr the N content is significantly lower than in the AISI 304L steel regardless of the crystallographic plane. In both substrates however, the highest amount of nitrogen seems to concentrate in the (200) planes and the lowest in the (220). The different partitioning of nitrogen in the various planes also brings about different expansion of the lattice, which in turn may induce strains and stresses. Menthe et al. [30] suggested that a tetragonal distortion of the fcc phase had occurred whereas Fewell et al. [31] proposed a triclinic distortion. Marchev et al. [32,33] considered instead the formation of a martensitic phase. However, any of these would imply the presence of extra peaks never observed on the diffraction patterns. A new structural model nitrogen expanded austenite has been recently proposed by Blawert et al. [4] assuming the effects of deformations and twin faulting commonly observed in fcc metals or alloys. The $\gamma_N$ expanded austenite would correspond to a fcc phase with a high density of stacking faults likely induced by the internal stresses existing in the nitrided layer [5,6]. Indeed, it has been shown that the presence of stacking and twin faults in a perfect fcc lattice produces angular displacements of peaks in XRD patterns [34]. The three nitrogen solid solutions observed by Leroy et al. [10] after plasma nitriding of the Ni base alloy Inconel 690 (Ni-30Cr-10Fe, *w*/%) has not been observed in this work using low energy-high flux implantation.

In the ODS FeAl intermetallic, the major contribution arises from the (110) and (220) reflections before and after nitridation. At grazing incidence, the hexagonal AlN appears as inferred by three XRD peaks ($2\Theta$ = 33.2°, 36.1° and 38°) and a large and high (110) peak corresponding to the substrate matrix [25]. In this alloy, the chemical affinity of N to Al is much greater than that to Fe (e. g., $\Delta H_f° = -318.0$ and $-10.5$ kJ mol$^{-1}$ for AlN and $Fe_4N$, respectively) [35] and thus iron nitride formation was not expected to occur.

The surface state after nitridation is also quite different among the substrates as shown by plane view SEM in **Figure 3**. In pure Ni some grains are darker and the orientation of the dislocation slipping bands composing each grain is underpinned; while other grains are lighter in colour and of smoother appearance. In addition, a significant number of protrusions appear throughout the entire surface, especially at grain boundaries. AFM investigations confirm that the roughness can vary between 17.5 nm and 27.5 nm and the aligned bands can be ascribed to the slipping bands due to the presence of stress, as also reported in fcc AISI 316 L stainless steel [36]. In Ni20Cr the surface is rather uniform and smooth with no protrusions but with relatively coarse pores. The average roughness is of about 5 – 8 nm but more significant height differences among grains compared to nitrided Ni. The AISI 304L surface is the most heterogeneous of all three fcc nitrided substrates. Some grains are very smooth and deeper and contain large pores thus reminding of the Ni20Cr grains, whereas other grains resemble more the nitrided Ni by underlining the slipping bands, hence being rougher. A common feature observed on the three fcc alloys is the occurrence of twinning within the grains, but again the morphology of twins differs from one matrix to the other. On the contrary, the ordered B2 cubic structure ODS FeAl, the surface seems very uniformly implanted with no twins but some protrusions at the external surface and remaining porosity. This latter feature can be mainly explained by the manufacturing process of this material, which is powder metallurgy. The elongated shape of the protrusions would be related to "softer" areas of the base material, where the strengthening effect

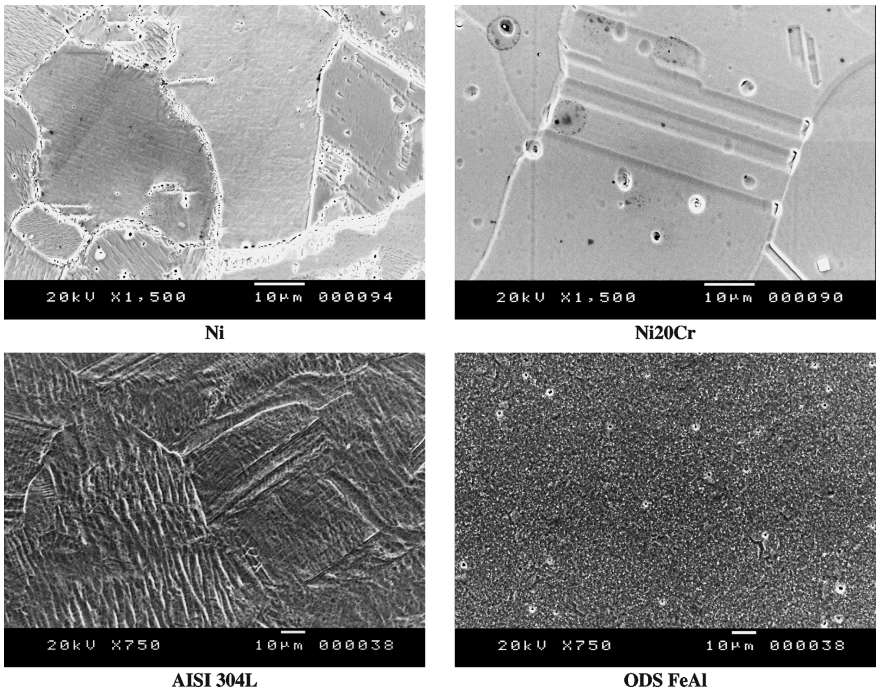


**Figure 3:** SEM surface morphology after low energy-high flux nitridation of (a) pure Ni, (b) Ni20Cr, (c) AISI 304L and (d) ODS FeAl
**Slika 3:** SEM-morfologija površine po nitriranju s fluksom z majhno energijo in veliko gostoto pri (a) čistem niklju, (b) NiCr20, (c) AISI 304 L in (d) ODS FeAl

of $Y_2O_3$ particles is less important, as revealed by AFM studies [**Figure 4(a)**]. This microstructure is accompanied by the highest roughness values, which can attain up to 50 nm.

According to the work of Pranevicius et al. [37], the surface roughness can derive from the competition between surface kinetics and bulk diffusion. Nucleation of roughness would first occur by relocation of adatoms, formation of surface vacancies and removal of atoms, which in turn lead to the appearance of clusters of atoms in other regions of the surface. The development of surface roughness subsequently occurs by further relocation and sputtering of atoms displaced by the ion beam. Thereafter, diffusion of nitrogen seems to occur mainly along grain and sub-grain boundaries creating compressive stresses [38]. Within the metallic substrate, atomic nitrogen can then recombine as molecular nitrogen, raising locally the pressure and inducing plastic deformation. Therefore, the amount of deformation would depend on the yield stress of the host material. As a result, a blistered surface appears [39,40]. Due to the recession of the metal surface upon implantation, the blisters are peeled off and the pores are then clearly visible in pure Ni and in Ni20Cr [**Figure 4(b)**]. Since the solubility of nitrogen in nickel is very low the observed porosity is rather shallow. The larger number of pores and blisters are however found at the grain and twin boundaries rather than within the grains as also inferred in a previous study [41]. This seems to support the idea that diffusion of nitrogen might be more prone to occur along these short circuit paths, which also become readily

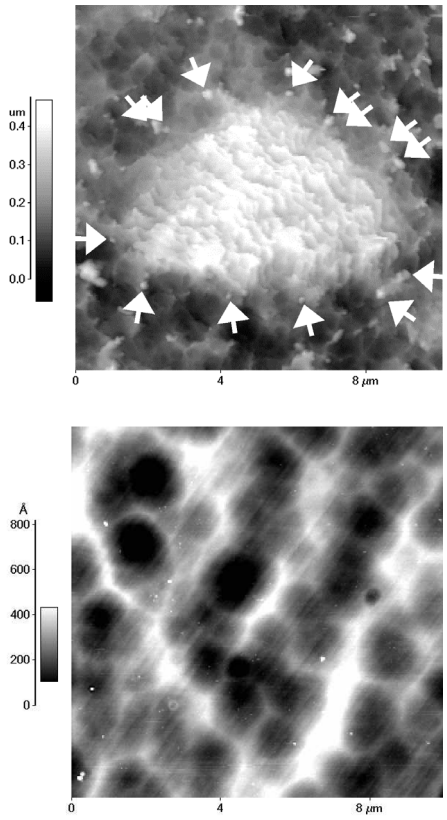


**Figure 4:** AFM images of (a) nitrided ODS FeAl showing ridges pinned by $Y_2O_3$ particles (b) nitrided Ni20Cr showing the resulting porosity (views of (10 × 10) µm areas)
**Slika 4:** AFM-sliki (a) nitrirani ODS FeAl, ki prikazuje grebene, zasidrane z delci $Y_2O_3$ in (b) nitriranega NiCr 20, ki prikazuje nastalo poroznost (ploskvi (10 × 10) µm

saturated in nitrogen inducing significant plastic deformation.

Indeed, EDS microanalyses indicate that no nitrogen has been retained in pure Ni either within the grains or at the grain boundaries where more protrusions are observed. Conversely, in the Cr-bearing alloys the distribution of nitrogen is uneven and confirms the XRD results. For instance, whereas about the mole fraction of N 10 % is present at the surface of Ni20Cr regardless of the location, in AISI 304L stainless steel some of the grains only incorporate about 12 % N and some others contain up to 17 % N, which is close to the chromium content in the substrate. Because of the anisotropic incorporation of N, different compressive stresses are generated. This leads to distortions, plastic deformation and even lattice rotations in an anisotropic fashion [42]. As a result of the anisotropic deformation, heterogeneous diffusion will occur modifying the nitrogen ingress rate [36]. On the contrary, in the FeAl intermetallic alloy the average composition is Fe-25Al-20N (*X*/%). This suggests that the N content being introduced could be limited by the Al amount at the surface of the substrate and therefore is only dependent on Al diffusion [43].

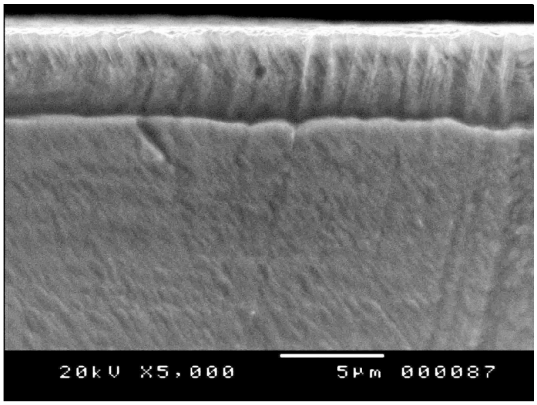


**Figure 5:** SEM cross section of the nitrided (a) AISI 304L stainless steel and (b) ODS FeAl showing protrusions and the nanograined structure of the substrate

**Slika 5:** SEM-prerez nitriranega (a) nerjavnega jekla AISI 304 in (b) ODS FeAl s protruzijami in nanozrnata struktura podlage

The SEM cross section morphologies clearly reveal that the only well defined nitrided layers appear on the AISI 304L and the ODS FeAl substrates after a chemical etch (**Figure 5**). However, the EDS composition profiles (**Figure 6**) indicate that N has effectively been incorporated in the Ni20Cr matrix. The maximum N content is found for the ODS FeAl alloy but the depth is the lowest because of N inward diffusion is arrested by the formation of AlN. On the contrary, the shape of the N content is similar in Ni20Cr and AISI 304L. As higher N contents are present in the steel, the nitrided layer is about 1 µm thicker in the steel than in the Ni20Cr alloy. At the substrate/nitrided layer interface, a steep N drop occurs in the steel in comparison with the Ni20Cr alloy. Some explanations can be found from thermodynamic calculations and TEM analyses. Nitrogen has a very low solubility [44] and permeability [45]. Upon nitrogen implantation chromium shows a strong tendency to form either the fcc CrN ($\Delta H°$ = –40 kJ mol$^{-1}$) or the hcp $Cr_2N$ ($\Delta H°$ = –38 kJ mol$^{-1}$) phases, which have not been observed experimentally in Ni20Cr. However, the hexagonal $Cr_2N$ phase seems to precipitate at the nitrided layer / AISI 304L interface as shown by cross section TEM and selected area diffraction patterns (SADPs) (**Figure 7**, **Table 3**). $Fe_2N$ nitride could be also present at the nitrided layer/steel interface but its heat of formation (–18 kJ mol$^{-1}$) suggests that $Cr_2N$ should be the major nitride. This means that the formation of metal nitrides at the nitrided layer/substrate interface would arrest further N inward diffusion and could explain the steep drop of the N content shown in **Figure 6**.

This may indicate that Cr allows to significantly increase the N solubility in Ni. Because nickel rejects nitrogen, the nickel-rich substrate (Ni20Cr) incorporates less nitrogen. On the other hand, from a thermodynamic point of view the free enthalpy ($\Delta G$) is more negative

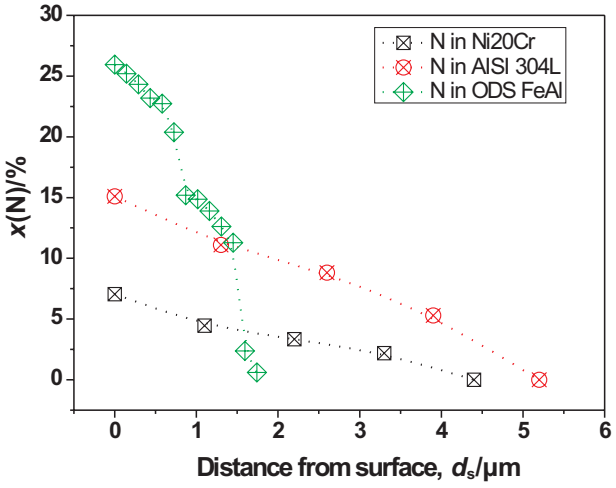


**Figure 6:** N profile from EDS microanalyses of the cross sections of the nitrided materials. (NB: EDS of ODS FeAl from TEM cross sections)

**Slika 6:** N-profil iz EDS-mikroanalize na prerezu nitriranih materialov (Opomba: EDS ODS FeAl iz TEM prereza)

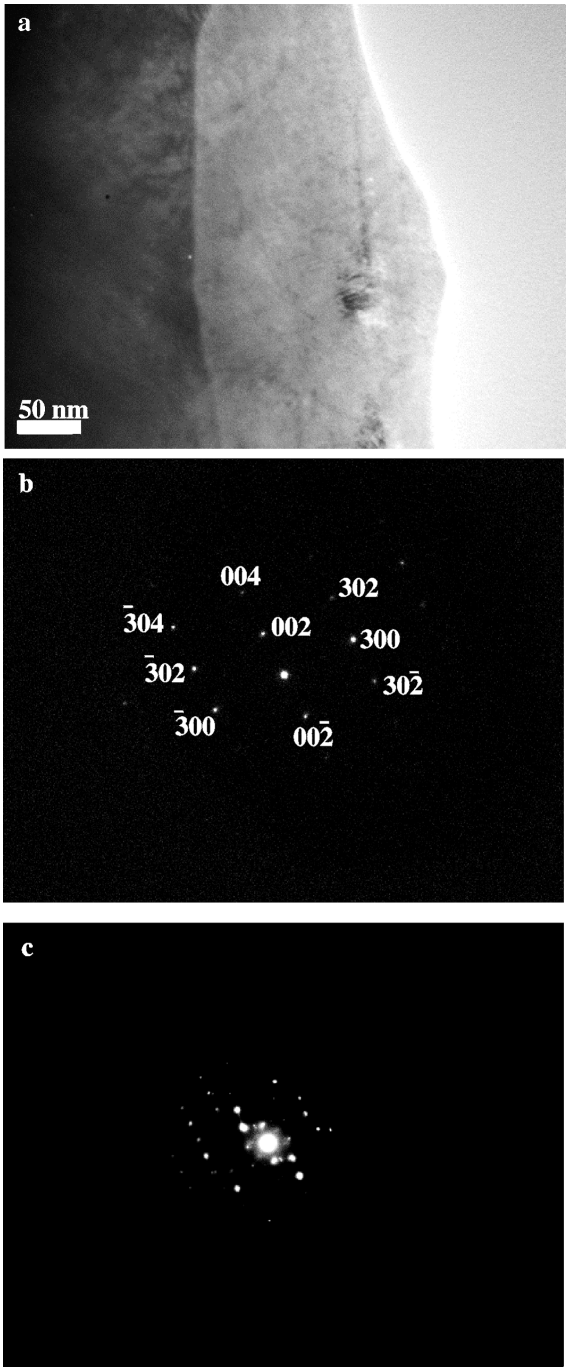


**Figure 7:** (a) TEM cross section of the nitrided AISI 304L stainless steel. SADPs of the (b) innermost zone corresponding to a single grain oriented $[010]_{Cr2N}$; and (c) outermost zone representative of various grains

**Slika 7:** (a) TEM-prerez nitriranega nerjavnega jekla AISI 304 L. SDAP (b) notranje cone, ki ustreza enemu zrnu z orientacijo $[010]_{Cr2N,}$ in (c) zunanja cona, ki ima različna zrna

(thus, more spontaneous reaction) upon the formation of chromium nitrides than that of iron nitrides (**Figure 8**). However, the iron effect cannot be neglected if the chemical potential of the species is also taken into account; i. e. when one mole of nitrogen encounters the substrate surface 70 % of the atoms are composed of iron

**Table 3:** Data from the selected area diffraction patterns (SADPs) shown in **Figures 7 (b)** and **(c)** and the corresponding compounds identified by TEM

**Tabela 3:** Podatkih iz difrakcijskih slik izbranih ploskev (SADPs), ki jih prikazuje **slika 7 (b)** in **(c)**, in ustrezna spojina, identificirana s TEM

| experimental *d*-spacing | $\gamma_N$ (experimental) | | $Cr_2N$ (JCPDS 79-2159) | | $Fe_2N$ (JCPDS 73-2102) | |
|---|---|---|---|---|---|---|
| | *d*-spacing | hkl | *d*-spacing | hkl | *d*-spacing | hkl |
| 2.40[c] | | | 2.37 | (110) | 2.39 | (110) |
| 2.25[b] | | | 2.21 | (002) | 2.21 | (002) |
| 2.10[c] | 2.10 | (111) | 2.09 | $(1\bar{1}1)$ | 2.10 | $(1\bar{1}1)$ |
| 1.86[c] | 1.86 | (200) | 1.86 | (201) | 1.87 | (201) |
| 1.52[c] | | | 1.55 | (210) | 1.48 | (211) |
| 1.46[c] | | | 1.46 | $(2\bar{1}1)$ | 1.47 | (003) |
| 1.35 [b] | | | 1.37 | (300) | 1.38 | (300) |
| 1.16 [b] | | | 1.16 | (302) | 1.17 | (302) |
| 0.92[c] | not assigned | | not assigned | | not assigned | |
| 0.89[c] | 0.89 | (400) | | | | |

[b] data from Figure 7 (b) and [c] from Figure 7 (c)

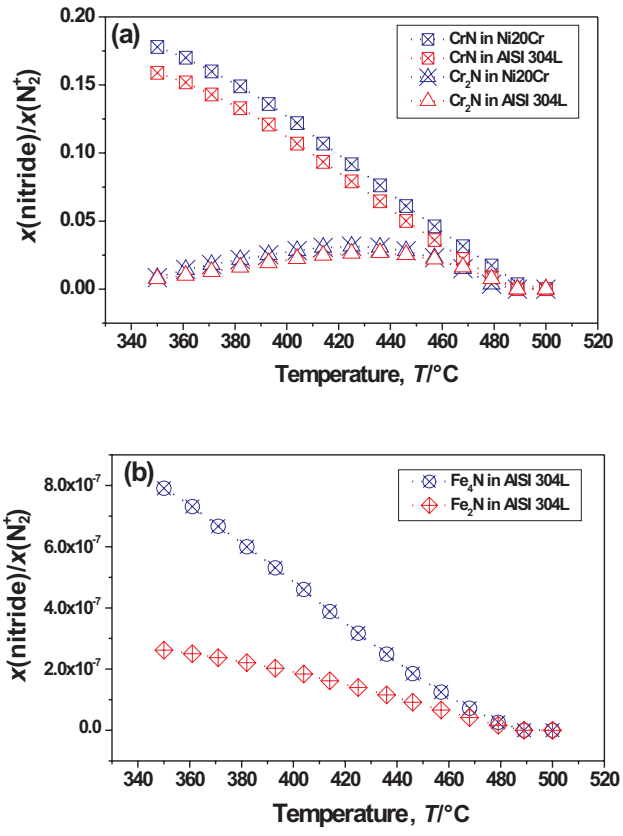


**Figure 8:** Evolution of mole of metal nitride produced per mole of $N_2^+$(g) as a function of temperature at $10^{-2}$ Pa according to the HSC thermochemical calculations [27] (a) chromium nitrides formation in Ni20Cr and AISI 304L and (b) iron nitrides in AISI 304L

**Slika 8:** Evolucija molarnosti kovinskega nitrida na mol $N_2$ (g) v odvisnosti od temperature pri $10^{-2}$ Pa na podlagi termokemičnih izračunov [27] (a) nastanka kromovih nitridov v NiCr20 in AISI 304 L in (b) nitridi železa v AISI 304 L

and only 20 % of chromium. As a result, iron can also enhance incorporation of nitrogen at least to some extent. Indeed, Rivière et al. [5] found that nitrogen was always detected in a nitride type state and that it was preferentially bound to chromium, without specific nitride formation, which agrees well with the trapping-detrapping mechanism proposed by Möller et al. [46]. Similarly, a small amount of iron atoms showed the same nitride type bonding but only at the outermost surface. Therefore, iron interaction together with a lower nickel content (which rejects nitrogen) results in higher nitrogen supersaturation in the superficial layers of AISI 304L than in Ni20Cr. Thereafter, because of the difference in chemical potentials between the external layer and the bulk, diffusion will be enhanced. As a result, the Fe-based alloy, which incorporates more nitrogen, will exhibit a higher degree of deformation. This induces significant swelling of the grains, thus developing rougher surfaces than Ni20Cr.

For the ODS FeAl intermetallic alloy, the nitrided layer has a nanostructured morphology and at the nitrided layer / substrate interface an iron band segregates (**Figure 9**). Diffraction patterns of the different areas point out the different features observed in these samples such as the nanometre scale of the nitrided layer characterised by the typical rings corresponding to FeAl as well as some spots at shorter distances belonging to AlN. As summarised in **Table 4**, some of the distances may also correspond to $\alpha$-Fe.

Sanghera and Sullivan [35] found that nitrogen implanted at low energy and low flux into pure aluminium did not render stoichiometric AlN because the radiation damage induced many vacancies, interstitials and defects. From our EDS analyses, only the outermost layers would contain enough nitrogen to produce the hexagonal AlN phases massively and therefore, once the average values of nitrogen decrease, a mixture of FeAl containing dispersed particles of AlN occurs closer to the nitrided layer/substrate interface. From the TEM results a combined mechanism of nitrogen diffusing inwardly and aluminium outwardly during the nitridation treatment would occur. This countercurrent diffusion would be promoted by the creation of short-circuit diffusion paths, i.e. the grain boundaries of the nanostructured layer. Indeed, diffusion of indium (isoelectronic with aluminium) has been found to be faster than that of iron by a factor of about two in $Fe_{66}Al_{34}$ and $Fe_{50}Al_{50}$ [47], which helps in corroborating the suggested mechanism.

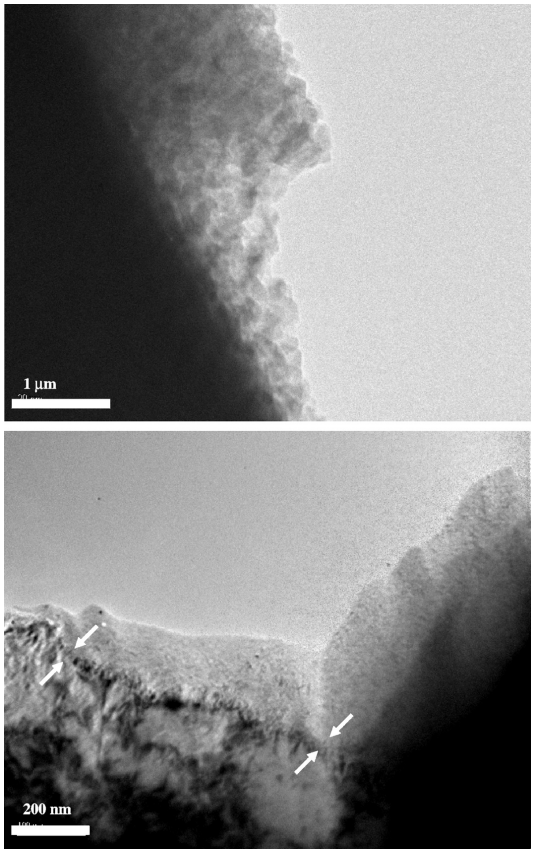


**Figure 9:** TEM cross section showing (a) the nanostructured morphology of the nitrided layer and (b) the nitrided layer/substrate interface. The band of $\alpha$-Fe segregated at this interface is indicated between arrows

**Slika 9:** TEM-prerez, ki prikazuje (a) nanostrukturirano morfologijo nitridne plasti, in (b) medpovršina nitrirana plast/podlaga. Plast segregiranega $\alpha$-Fe na tej medpovršini je prikazana med puščicami

**Table 4:** Experimental *d*-spacings obtained with 0.15 μm-diaphragm SADPs at the nitrided layer/substrate interface in the as-nitrided intermetallic alloy and their correspondence to the planes of the identified compounds

**Tabela 4:** Eksperimentalne *d*-razdalje, izmerjene pri SDPS z 0,15 μm veliko zaslonko, na medpovršini nitridna plast/podlaga v nitrirani intermetalni spojini in njihova lega glede na ploskev indentificiranih spojin

| Experimental *d*-spacing, nm | FeAl JCPDS 33-20 | $\alpha$-Fe JCPDS 89-4186 | AlN JCPDS 25-1133 |
|---|---|---|---|
| 0.252 | – | – | 002 |
| 0.207 | 110 | 110 | – |
| 0.160 | 111* | – | 110 |
| 0.143 | 200 | 200 | – |
| 0.119 | 211 | 211 | 202 |

* superstructure peak

### *3.2 High Temperature oxidation behaviour*

Because of their specific uses, the oxidation tests were conducted at different temperatures and the results will be therefore presented independently.

#### 3.2.1 Oxidation of Ni and Ni20Cr: 700 °C and 800 °C

**Figure 10** shows the mass gain curves against time for both untreated and nitrided specimens. It can be observed that in nitrided Ni no significant difference is observed at both temperatures. On the contrary, in Ni20Cr nitridation increases significantly the overall mass gain. Assuming parabolic behaviour, the oxidation constants have been calculated by the $(\Delta M/S)^2$ vs. time

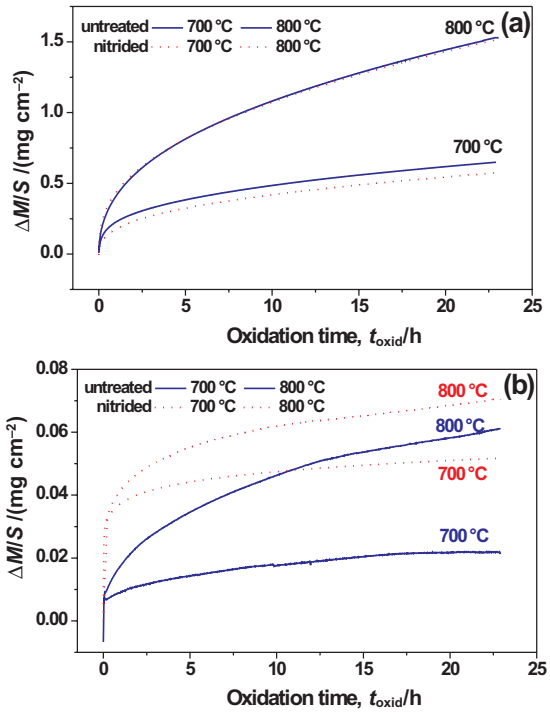


**Figure 10:** Isothermal oxidation at 700 °C and 800 °C for 24 h in synthetic air (a) untreated and nitrided Ni and (b) untreated and nitrided Ni20Cr

**Slika 10:** Izotermna 24-urna oksidacija pri 700 °C in 800 °C v sintetičnem zraku; (a) nenitriran in nitriran Ni in (b) nenitriran in nitriran NiCr20

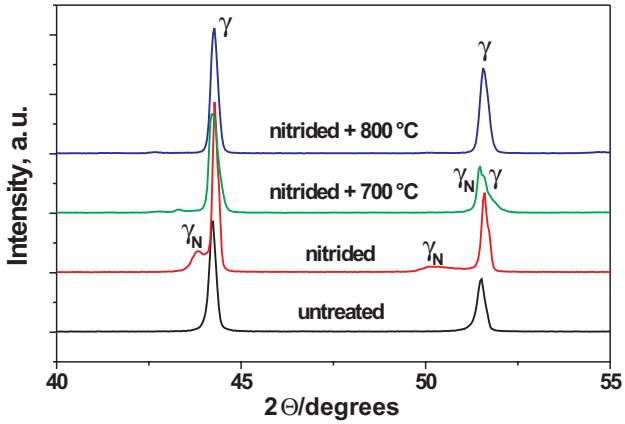


**Figure 11:** Selected range of the obtained on the untreated, as-nitrided and nitrided and oxidised at 700 °C and 800 °C Ni20Cr substrates. N.B: Only the matrix peaks are indicated. See text for further information concerning oxide species.

**Slika 11:** Izbrana področja na nenitriranem, nitriranem in nitriranem ter oksidiranem Ni20Cr podlagah. (Opomba: Prikazani so le vrhovi matice. V tekstu je pojasnilo o vrstah oksidov).

method. In Ni, the parabolic rate constant ($k_p$) values of $4 \cdot 10^{-12}$ g$^2$ cm$^{-4}$ s$^{-1}$ and $2.5 \cdot 10^{-11}$ g$^2$ cm$^{-4}$ s$^{-1}$ are found for 700 °C and 800 °C, respectively. However, in Ni20Cr the $k_p$ values increase about one order of magnitude from ($1.0 \cdot 10^{-15}$ to $8.3 \cdot 10^{-15}$) g$^2$ cm$^{-4}$ s$^{-1}$ at 700 °C and from ($2.3 \cdot 10^{-14}$ to $2.3 \cdot 10^{-13}$) g$^2$ cm$^{-4}$ s$^{-1}$ at 800 °C after the whole oxidation test.

The XRD patterns have revealed the formation of NiO oxides in both untreated and nitrided Ni samples, together with some weak peaks of the substrate, indicating a relatively thick oxide layer at both temperatures. The oxide species developed on Ni20Cr are the same for both the untreated and nitrided specimens at either temperature and these include NiO, $NiCr_2O_4$ and $Cr_2O_3$. At the highest temperatures, more contribution of $Cr_2O_3$ oxide is found to occur. However, the substrate/oxide intensity ratios are always higher at any temperature than in the nickel substrates. This means that a thinner oxide layer is obtained in the Ni20Cr samples after 24 h of isothermal oxidation. Regarding the expanded austenite ($\gamma_N$) phase (**Figure 11**) oxidation at 700 °C for 24 h brings about shifting of the $\gamma_N$ and $\gamma$ peaks towards the original $\gamma$ phase ($2\Theta = 44.28°$) giving rise to the observed doublet. This clearly implies redistribution of nitrogen in the matrix but no nitride phase can be derived from the XRD results.

The SEM morphologies are also completely different. Whereas the untreated specimens develop even and homogeneous oxide scales, the oxide layers spall off or oxide plates develop in nitrided Ni [**Figure 12(a)** and **(b)**]. In Ni20Cr oxidation occurs preferentially depending on the grain orientation and grain boundary. At the lowest temperatures, the Ni20Cr samples are distinctively covered of oxides [**Figure 12 (c)** and **(d)**], which are more developed at 800 °C [**Figure 12(e)** and **(f)**],

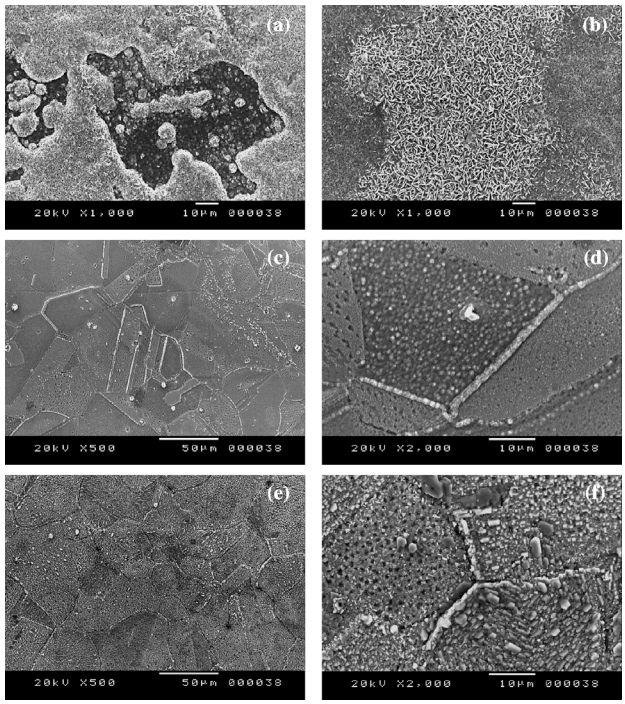


**Figure 12:** SEM surface morphologies developed at high temperature on (a) and (b) nitrided Ni at 700 °C and 800 °C; (c) and (d) nitrided Ni20Cr at 700 °C and (e) and (f) Ni20Cr at 800 °C

**Slika 12:** SEM-morfologija površin, ki so nastale pri visoki temperaturi na (a) in (b) nitriranem Ni pri 700 °C in 800 °C, (c) in (d) nitriranem Ni20Cr pri 700 °C in (e) ter (f) pri 800 °C

thus suggesting that the N implantation effect is lost at the highest temperature, as confirmed on the cross sections by SEM and EDS microanalyses. Indeed, the N content drops from about the mole fraction 10 % at the surface of the as-nitrided specimens to 3.5 % and 0 % after 24 h of oxidation at 700 °C and 800 °C. At 800 °C, some tiny metal nitrides precipitate (about 3 % N).

3.2.2 Oxidation of AISI 304L: (400, 450, 500 and 550) °C

**Figure 13** shows the mass gain curves as a function of time for both the untreated [**Figure 13 (a)**] and the nitrided [**Figure 13 (b)**] specimens. Oxidation is more significant in the nitrided samples than in the untreated steel upon the first oxidation times at any temperature as a result of both a chemical and physical effect [48]. The first one is related to the amount of implanted nitrogen, whereas the second refers to the defects induced upon implantation.

The XRD patterns of the untreated steel show mainly the substrate peaks, i. e. austenite $\gamma$ and ferrite $\alpha$ phases are observed, indicating the low thickness of the scale. The small participation of the ferrite $\alpha$ phase has been previously reported to occur as a result of both plastic deformation induced upon grinding [49] and after high temperature exposure due to chromium outward diffusion, which partially destabilise the $\gamma$ austenitic phase until oxide formation is accomplished [50]. Only in

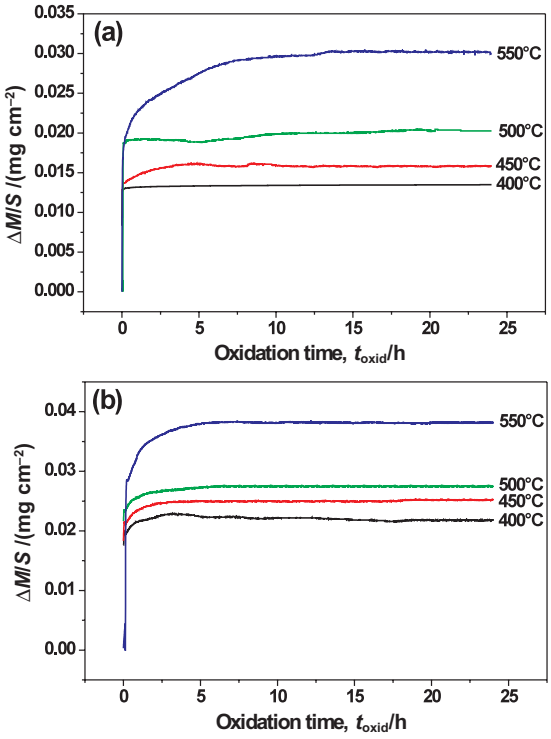


**Figure 13:** Isothermal oxidation of the AISI 304L stainless steel at 400, 450, 500 and 550 °C for 24 h in synthetic air (a) untreated and (b) nitrided

**Slika 13:** Izotermna oksidacija nerjavnega jekla AISI 304 L 24 h pri (400, 450, 500 in 550) °C v sintetičnem zraku; (a) nenitrirano, (b) nitrirano

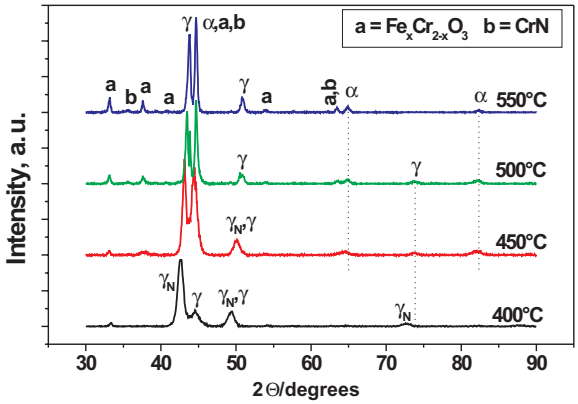


**Figure 14:** GIXRD patterns at 15° of the nitrided AISI 304L stainless steel after oxidation in air for 24 at 400, 450, 500 and 550 °C

**Slika 14:** GIXRD-odsevi pri 15° za nitrirano nerjavno jeklo AISI 304L po 24-urni oksidaciji na zraku pri (400, 450, 500 in 550) °C

GIXRD at 15° a weak hematite ($\alpha$-$Fe_2O_3$) signal appears at 550 °C.

In the nitrided specimens, the $\gamma_N$ phase is present up to 500 °C [**Figure 14**] but it evolves towards a more stable state, which implies rejection of nitrogen in solid solution in the nitrided layer. Mändl et al. [51] after annealing of a nitrided austenitic stainless steel at 425 °C found that the lattice expansion was considerably reduced, yielding a new $\gamma_{N2}$ phase and additional CrN peaks under 8° of incidence. The XRD results of **Figure 14** indicate that the decomposition of the $\gamma_N$ phase occurs by formation of CrN and two other FeNi phases $\alpha$ (bcc) and $\gamma$ (fcc) probably containing a small amount of Cr. The precipitation of the cubic CrN phase is detected from 500° C since at 400°C the mobility of chromium in the AISI 304L stainless steel is low [52]. The presence of the $\alpha$ phase can be explained as for the untreated steel (see above) as well as from the nitrogen partial dissolution from the $(Fe,Cr)_2N$ leading to a $\alpha$'-(N) martensite [53]. This fact, together with the substantial decrease of superficial nitrogen observed by EDS, indicates that upon oxidation, nitrogen may mainly diffuse inwardly towards the bulk. Such diffusion coupled to the outward diffusion of chromium from the bulk alloy gives rise to the more thermodynamically and kinetically stable CrN nitride. Öztürk and Williamson [54] also found the formation of CrN upon the post-annealing of the AISI 304 stainless steel at 400 °C. However, decomposition of such phase was not observed even after 36 h but a dramatic reduction in N content due to inward and outward diffusion.

The oxide scales developed in the untreated steel evolve mainly through bulk alloy outward diffusion and not via the grain boundaries [**Figure 15 (a) and (b)**]. On the contrary, oxide development is more pronounced on the surface of the nitrided steel even at the lowest oxidation temperatures as a result of the deformation induced through ion implantation [**Figure 15 (c)**]. Again, as the oxidation temperature increases, the oxide cove-

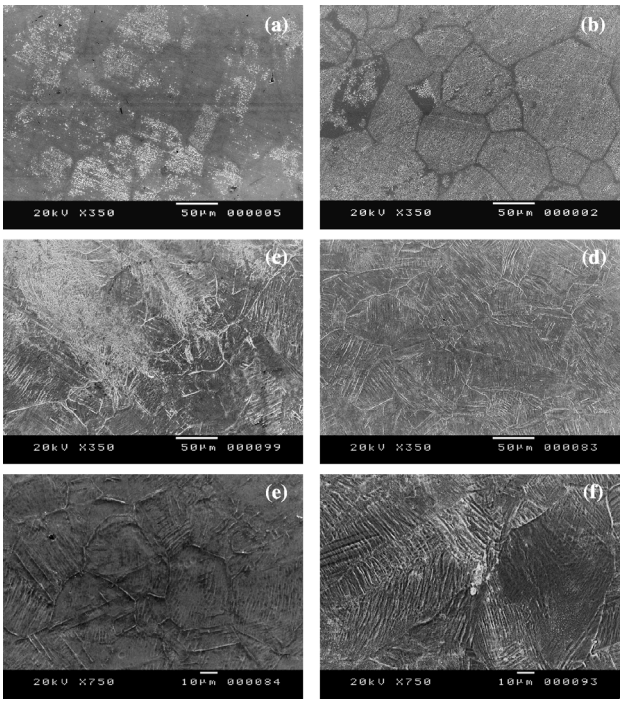


**Figure 15:** SEM surface morphologies developed the AISI 304L stainless steel (a) and (b) untreated and oxidised at 500 °C and 550 °C, respectively; and of nitrided and oxidised at (c) 400 °C, (d) 450 °C, (e) 500 °C and (f) 550 °C

**Slika 15:** Morfologija površine, nastale na nerjavnem jeklu AISI 304L: (a) izhodna in (b) oksidirana pri 500 °C in 550 °C; nitrirana in oksidirana pri (c) 400 °C, (d) 450 °C, (e) 500 °C in (f) 550 °C

rage increases depending on the roughness of each grain [**Figures 15 (d), (e) and (f)**]. Contrary to the untreated steel, diffusion seems to occur through both the bulk alloy and the grain boundaries.

The EDS microanalyses show the only presence of oxygen, chromium and iron on the scales (**Figure 16**). It can be observed that oxide formation is clearly promoted with increasing temperature whereas the superficial nitrogen content decreases. The ratios Fe/Cr after oxidation of the untreated steel at any temperature are relatively the same in comparison with the unoxidised steel. According to the cross section analyses, the oxidising temperature seems to provide enough energy to induce chromium and nitrogen diffusion so that tiny precipitation of CrN might occur as for the Ni20Cr substrates. This in turn leads to the $\gamma_N$ disappearance and the formation of the $\alpha$ phase. Öztürk and Williamson [54] observed the vanishing of the magnetic state of the $\gamma_N$ phase as the post-annealing treatment of the fcc AISI 304 steel at 400 °C progressed with time, in agreement with the above results.

### 3.2.3 Oxidation of ODS FeAl: 800 °C

After the 24 h exposure at 800° C, the weight gains of the nitrided specimens was four-fold that of the un-nitrided, with $k_p$ values of about $4.7 \cdot 10^{-8}$ mg$^2$ cm$^{-4}$ s$^{-1}$ for the latest stage [25], i.e. even 10 times faster than those of nitrided $\alpha$-iron [55].

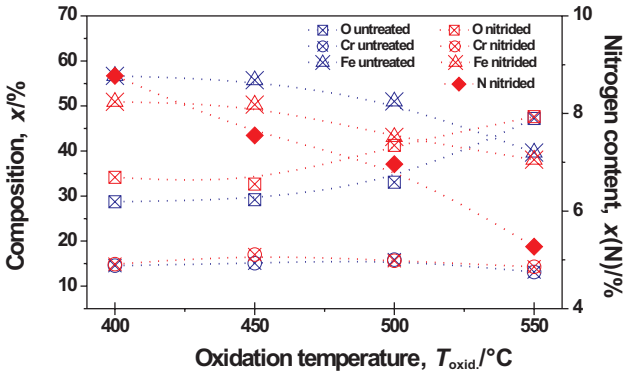


**Figure 16:** EDS surface composition of the oxidised surfaces of both untreated (blue) and nitrided (red) as a function of the oxidation temperature

**Slika 16:** EDS-sestava oksidirane površine nenitrirane (modro) in nitrirane površine v odvisnosti od temperature oksidacije

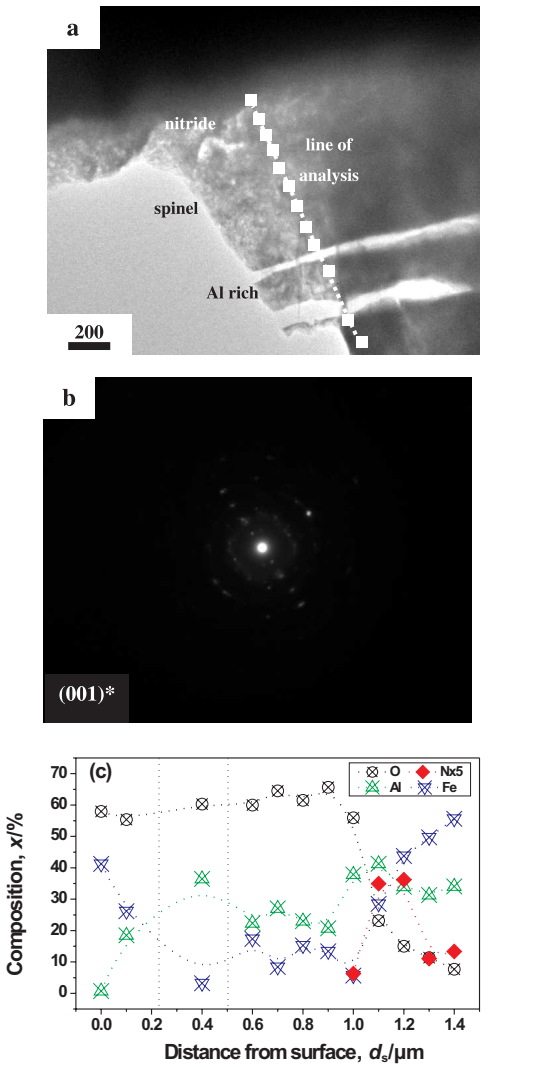


**Figure 17:** (a) Bright field TEM image of the stratified oxide scale, (b) SADP at the inner scale/substrate interface and (c) EDS micro-analyses across all the layers

**Slika 17:** (a) TEM-slika v svetlem polju za plastasti oksidni sloj, (b) SADP na medploskvi notranja plast škaje/podlaga in (c) EDS-analiza po prerezu vseh plasti

After cooling, the oxide scales are shown to extensively spall off, depicting at least two subscales, a very convoluted top layer and an inner layer with white needles. Although the surface EDS microanalysis and XRD only indicated the presence of iron oxide (hematite), TEM inspection reveals a more complex oxide scale [**Figure 17 (a)**]. As shown in **Figure 17 (b)**, the selected area diffraction patterns (SADPs) at the top and bottom inner scale suggests the existence of the $FeAl_2O_4$ phase, with a contribution of hexagonal AlN at the oxide/substrate interface, whose reflections are summarised in **Table 5**. The EDS (3 nm spot) microanalyses across the entire scale **[Figure 17 (c)]** confirm that the outermost oxide layer is only composed of iron and oxygen and is about 0.25 μm thick. According to the XRD patterns [25] this phase has been identified as $\alpha$-$Fe_2O_3$. Underneath, a 0.2 μm thick layer exists, which is mostly enriched in aluminium, which may correspond to $\alpha$-$Al_2O_3$. The inner oxide layer is the largest (about 0.5 μm thick) with more of Al than Fe, hence suggesting the presence of the $FeAl_2O_4$ phase found by SADP. At the spinel substrate interface nitrogen is found to concentrate, accompanied with a drop in the oxygen content.

**Table 5:** Experimental d-spacings obtained from SADPs at the inner oxide layer / substrate interface after oxidation at 800 °C of the nitrided ODS FeAl and their correspondence to the planes of the identified compounds.

**Tabela 5:** Esperimentalne *d*-razdalje iz SADPs na medpovršini notranja oksidna plast/podlaga po oksidaciji nitrirane ODS FeAl pri 800 °C in njihova lega glede na ravnine identificirane spojine

| *d*-spacing, nm | $FeAl_2O_4$ (JCPDS 34-192) | AlN (JCPDS 25-1133) |
|---|---|---|
| 0.465 | 111 | – |
| 0.270 | – | 100 |
| 0.246 | 311 | 002 |
| 0.204 | 400 | – |
| 0.186 | 331 | 102 |
| 0.139 | – | 103 |

Such complex structure allows to shed some light on the oxidation mechanisms after nitridation of ODS FeAl. Although outward diffusion of indium (isoelectronic with aluminium) is two times faster than that of iron in $Fe_{66}Al_{34}$ and $Fe_{50}Al_{50}$ [47], there is not enough aluminium available at the top surface to form the oxide since this is trapped as AlN throughout the compact layer. At the diffusion layer, $\alpha$-Fe was found to segregate at the fragmented FeAl matrix together with some AlN. Such iron is readily available for outward diffusion through the important number of short circuit paths that represent the grain boundaries and defaults created upon nitridation. However, once the outer iron scale is developed, the oxygen partial pressure decreases and only aluminium oxide is able to form owing to its higher thermodynamic stability. At reduced pressure only the $\alpha$-$Al_2O_3$ phase should develop but its reaction with either $Fe_2O_3$ [56] or FeO [57], a $FeAl_2O_4$ spinel oxide forms. At reduced oxygen partial pressures dissolution of AlN also takes place [58] and indeed, no nitrogen is found in any of the oxide layers except at the spinel / substrate interface. This implies that after dissolution of the nitride, nitrogen seems to diffuse further inwardly towards the substrate whereas the resulting aluminium tends to be transported outwardly, stabilising the spinel oxide phase. In previous works [59] it was already claimed that the spinel layer would only be partially effective in hindering outward aluminium diffusion when the grains coarsened with increasing temperature.

## 4 SUMMARY AND CONCLUSIONS

Similar low energy, high flux nitridation processing conditions on different fcc metallic substrates lead to very different results depending on the chemical composition of the matrix. It has been shown that pure nickel does not develop an expanded austenite phase due to rejection of nitrogen. The tiny retained amount of nitrogen creates blisters and pores as nitrogen tries to be triggered off the substrate. The major surface roughness is then developed by sputtering. On the contrary, with the addition of chromium an expanded austenite phase develops but nitrogen uptake is still limited by nickel rejection. In turn, iron atoms can thermodynamically favour nitrogen uptake at least at the outermost surface. The higher the nitrogen intake, the higher the degree of deformation including grain swelling, which leads to rougher and harder surfaces. On the contrary, in the presence of Al (ODS FeAl alloy) brings about the formation of an outer AlN compact layer and an inner diffusion layer in which AlN, $\alpha$-Fe segregation and fragmentation of the FeAl grains occur. Deformation of the material also seems to be induced upon implantation.

The high temperature oxidation behaviour seems to depend thereafter of the microstructure and chemistry of the implanted specimens. Whereas in pure Ni nitridation does not basically change the oxidation kinetics, on Ni20Cr the kinetics are increased by one order of magnitude. This is mainly due to trapping of chromium by the implanted nitrogen, hence impeding the formation of the protective $Cr_2O_3$ scale. For the longest exposures enough chromium flux from the matrix seems to be ensured. Deformation induces oxide scale spallation as shown in nitrided Ni. In the AISI 304L stainless steel oxidation of the nitrided specimens brings about progressive disappearance of the $\gamma_N$ phase accompanied with the appearance of an $\alpha$ phase and precipitation of fcc CrN nitride. This phase transformation phenomenon, in turn, may supply chromium to the oxide scale, since the nitrided samples have shown to be enriched in this metal in comparison with the untreated steel. Our results suggest that oxidation seems to proceed by oxygen inward diffusion through the more nitrogen rich planes composing the grains. In the nitrided ODS FeAl aluminium is trapped as AlN, therefore allowing the formation of a non protective outer $Fe_2O_3$ scale. Once the oxygen partial pressure is reduced dissolution of AlN occurs. Thereafter, nitrogen is further transported

inwardly, whereas aluminium diffuses outwardly. As a result, the $FeAl_2O_4$ spinel inner layer is developed under the $Fe_2O_3$ top layer. Therefore, the nitridation treatment changes the oxidation mechanisms. Overall, the role of implanted nitrogen is to retard the establishment of an external alumina scale, but does not seem to impede it. Longer oxidation tests should be carried out to confirm this possibility.

**Acknowledgments**

J.P. Rivière and G. Abrasonis from the LMP laboratory at Poitiers (France) are gratefully acknowledged for the nitridation experiments. These acknowledgments are also extended to various colleagues of the LEMMA laboratory (G. Bonnet, J. F. Dinhut, J. L. Grosseau-Poussard, J. Balmain and C. Savall) for carrying out some of the experiments and for fruitful discussion.

## 5 REFERENCES

[1] A. M. Jones, S. J. Bull Surf. Coatings Technol. 83 (**1996**), 269
[2] S. Picard, J. B. Memet, R. Sabot, J. L. Grosseau-Poussard, J. P. Rivière, R. Meilland, Mater. Sci; Eng. A 303 (**2001**), 163
[3] Z. L. Zhang, T. Bell, Surf. Eng. 1 (**1985**), 131
[4] C. Blawert, H. Kalvelage, B. L. Mordike, G. A. Collins, K. T. Short, Y. Jiraskova, O. Schneeweiss, Surf. Coatings Technol. 136 (**2001**), 181
[5] J. P. Rivière, P. Méheust, J. P. Villain, C. Templier, M. Cahoreau, G. Abrasonis, L. Pranevicious, Surf. Coatings Technol. 158–159 (**2002**) 99
[6] J. P. Rivière, M. Cahoreau, P. Méheust, J. Appl. Phys. 91 (**2002**) 10, 6361
[7] C. T. Sims, N. S. Stoloff, W. C. Hagel, Superalloys II, John Wiley & Sons, Inc. Chichester (1987)
[8] P. K. Aw, A.W. Bachelor, N. L. Loh, Surf. Coatings Technol. 89 (**1997**), 70
[9] P. K. Aw, A. W. Bachelor, N. L. Loh, Wear 208 (**1997**), 226
[10] C. Leroy, T. Czerwiec, C. Gabet, T. Belmonte, H. Michel, Surf. Coatings Technol. 142–144 (**2001**), 241
[11] H. He, T. Czerwiec, C. Dong, H. Michel, Surf. Coatings Technol. 163–164 (**2003**), 331
[12] F. Pedraza, J. L. Grosseau-Poussard, G. Abrasonis, J. P. Rivière, J. F. Dinhut, J. Appl. Phys. 94 (**2003**), 7509
[13] F. Pedraza, C. Savall, G. Abrasonis, J. P. Rivière, J. F. Dinhut, J. L. Grosseau-Poussard, Thin Solid Films 515 (**2007**), 3661
[14] D. Williamson, J. A. Davis, P. J. Wilbur, Surf. Coatings Technol. 103–104 (**1998**), 178
[15] J. P. Rivière, P. Méheust, J. A. García, R. Martínez, R. Sánchez, R. Rodríguez, Surf. Coatings Technol. 158–159 (**2002**), 295
[16] A. Lasalmonie, Intermetallics 14 (**2006**), 1123
[17] S. Thongtem, T. Thongtem, M. J. McNallan, Surf. Interface Anal. 28 (**1999**) 1, 61
[18] J. Magnan, G. C. Weatherly, M. C. Cheynet, Met. Mat. Trans. 30A (**1999**) 1, 19
[19] B. Zhao, J. Sun, J. S. Wu, Z. X. Yuan, Scripta Mater. 46 (**2002**), 581
[20] C. L. Chu, S.K. Wu, Surf. Coatings Technol. 78 (**1996**), 219
[21] T. K. Roy, R. Balasubramaniam, A. Gosh, Met. Mat. Trans. 27A (**1996**) 12, 3993
[22] T. K. Roy, R. Balasubramaniam, A. Gosh, Met. Mat. Trans. 27A (**1996**) 12, 4003
[23] H. C. Choe, Surf. Coatings Technol. 148 (**2001**), 77
[24] B. Zhao, J. Wu, J. Sun, B. Tu, F. Wang, Intermetallics 9 (**2001**), 697
[25] C. Dang Ngoc Chan, C. Huvier, J. F. Dinhut, Surf. Coatings Technol. 165 (**2003**), 119
[26] Y. Ando, S. Tobe, H. Tahara, T. Yoshikawa, Vacuum 65 (**2002**), 403
[27] Outokompu HSC Chemistry for Windows, Outokompu Research Oy, Pori, 1994
[28] R. Wei, Surf. & Coatings Technol. 83 (**1996**), 218
[29] J. P. Rivière, C. Brin, Ph. Méheust, J. P. Villain, R. Cauvin J. Phys. IV 11 (**2001**), 71
[30] E. Menthe, K. T. Rie, Surf. Coatings Technol. 116–119 (**1999**), 199
[31] M. P. Fewell, D. R. G. Mitchell, J. M. Priest, K. T. Short, G. A. Collins, Surf. Coatings Technol. 131 (**2000**), 300
[32] K. Marchev, R. Hidalgo, M. Landis, R. Vallerio, C. V. Cooper, B. C. Giessen, Surf. Coatings Technol. 112 (**1999**), 67
[33] K. Marchev, R. Hidalgo, M. Landis, R. Vallerio, C. V. Cooper, B. C. Giessen, Surf. Coatings Technol. 116–119 (**1999**), 184
[34] B. E. Warren, X-Ray Diffraction, Dover, New York (1990)
[35] H. K. Sanghera, J. L. Sullivan, Surf. Interface Anal. 27 (**1999**), 678
[36] G. Abrasonis, J.P. Rivière, C. Templier, A. Déclemy, L. Pranevicious, X. Milhet J. Appl. Phys. 97 (**2005**) 8, 3531
[37] L. Pranevicius, C. Templier, J. P. Rivière, P. Méheust, L. L. Pranevicius, G. Abrasonis, Surf. Coatings Technol. 135 (**2001**), 250
[38] L. Pranevicius, L. L. Pranevicius, D. Milcius, S. Muzard, C. Templier, J. P. Rivière, Vacuum 72 (**2004**), 161
[39] M. F. Denanot, J. Delafond, J. Grilhé, Rad. Effects 88 (**1986**), 145
[40] A. P. Matthews, M. Iwaki, Y. Horino, M. Satou, K. Yabe, Nucl. Inst. Meth. Phys. Res. B59/60 (**1991**), 671
[41] F. Pedraza, M. Reffass, G. Abrasonis, C. Savall, J. P. Rivière, Surf. Coatings Technol. 176 (**2004**), 236
[42] B. Clausen, T. Lorentzen, M. A. M. Bourke, M. R. Daymond, Mat. Sci. Eng. A259 (**1999**), 17
[43] F. Pedraza, J. L. Grosseau-Poussard, Thin Solid Films 467 (**2004**), 140
[44] M. Hansen, K. Anderko, Constitution of Binary Alloys 2nd Ed. McGraw-Hill Co. Inc., New York (1958), 984
[45] A. A. Kodentsov, M. J. H. Van Dal, C. Cserhati, L. Daroczi, F. J. J. Van Loo, Acta Mater. 47 (**1999**), 3169
[46] W. Möller, S. Parascandola, T. Telbizova, R. Günzel, E. Richter, Surf. Coatings Technol. 136 (**2001**), 73
[47] H. Mehrer, M. Eggersmann, A. Gude, M. Salamon, B. Sepiol, Mat. Sci. Eng. A239-240 (**1997**), 889
[48] P. Kofstad, High Temperature Corrosion, Elsevier Applied Science Publishers, Ltd. Essex, 1988, 61
[49] F. J. Pérez, M. J. Cristóbal, M. P. Hierro, F. Pedraza, Surf. Coatings Technol. 120–121 (**1999**), 442
[50] F. Pedraza, PhD Thesis. Universidad Complutense de Madrid, 1998
[51] S. Mändl, R. Günzel, E. Richter, W. Möller, B. Rauschenbach, Surf. Coatings Technol. 128–129 (**2000**), 423
[52] W. Liang, X. Bin, Y. Zhiwei, S. Yaqin, Surf. Coatings Technol. 130 (**2000**), 304
[53] M. A. El Khakani, G. Marest, N. Moncoffre, J. Tousset, Nucl. Inst. Meth. Phys. Res. B59/60 (**1991**), 817
[54] O. Öztürk, D. L. Williamson, Surf. Coatins Technol. 158–159 (**2002**), 288
[55] R. H. Jutte, B. J. Koi, A.J. Sommers, E-J. Mittemeijer, Oxid. Met. 48 (**1997**), 87
[56] T. Fujimura, S. I. Tanaka, J. Mater. Sci. 34 (**1999**), 425
[57] S. E. Sadique, M. A. H. Mollah, M. M. Ali, M. M. Haque, S. Basri, M. M. H. M. Ahmad, S. M. Sapuan, Oxid. Met., 54 (**2000**) 5–6, 385
[58] C. H. Xu, W. Gao, Y. D. He, Scripta. Mater. 42 (**2000**), 975
[59] F. Pedraza, J. L. Grosseau-Poussard, J. F. Dinhut, Intermetallics 13 (**2005**), 27

UDK 678.6/.7:620.18
Original scientific article/Izvirni znanstveni članek

ISSN 1580-2949
MTAEC9, 42(3)171(2008)

# NUMERICAL AND EXPERIMENTAL ANALYSES OF THE DELAMINATION OF CROSS-PLY LAMINATES

## NUMERIČNA IN EKSPERIMENTALNA ANALIZA DELAMINACIJE V KRIŽNIH PLOŠČATIH LAMINATIH

**Robert Zemčík, Vladislav Laš**

University of West Bohemia in Pilsen, Department of Mechanics, Univerzitní 22, 306 14, Plzeň, Czech Republic
zemcik@kme.zcu.cz

*Prejem rokopisa – received: 2007-09-20; sprejem za objavo – accepted for publication: 2008-01-16*

This article focuses on a numerical and experimental investigation of the delamination of cross-ply FRP laminates. The tested samples were cut from plates [0/90/90/0] made of unidirectional carbon-epoxy prepregs in a vacuum autoclave. The experimental tests were performed on precracked double-cantilever beam samples according to ASTM standards with Mode-I loading. The load-displacement relations were recorded during the test and the crack length was measured optically with a digital camera. The corresponding numerical simulations were performed in the finite-element code MSC.Marc. The goal was to assess the critical value of the energy-release rate $G$, which was chosen as the interlaminar fracture toughness. The simulation used the equality between the energy-release rate and the J-integral for the elastic case.

Keywords: composite, cross-ply, beam, delamination, experiment, simulation

V delu obravnavamo numerično in eksperimentalno raziskavo delaminacije v križnih ploščatih FRP-laminatih. Preizkušanci so bili odrezani iz plošč [0/90/90/0], ki so bile izdelane v avtoklavu iz surovcev ogljikovo vlakno-epoksi. Preizkusi so bili izvršeni na vnaprej razpokanih dvojno vpetih nosilcih skladno z ASTM-standardi z obremnitvijo Mode 1. Odnos obremenitev – pomik je bil ugotovljen med preskusom, dolžina razpoke pa se je merila optično z digitalno kamero. Za numerično simulacijo je bila uporabljena metoda končnih elementov s kodo MSC.Marc. Cilj je bil določiti kritično vrednost hitrosti sprostitve energije G, ki je bila opredeljena kot interlaminarna žilavost loma. V simulaciji je uporabljena enakost med hitrostjo sprostitve energije in J-integralom za primer elastičnosti.

Ključne besede: kompoziti, križna plošča, nosilec, delaminacija, eksperiment, simulacija

## 1 INTRODUCTION

One of the key damage mechanisms in laminates is the origin and propagation of a failure or a crack between individual layers; this is known as delamination and it must be considered in the design of a laminated structure. Delamination can be caused by imperfections during the manufacturing process or due to static and dynamic loads. The existence of delamination in a composite material degrades its stiffness and in certain cases it can degrade the stability to a critical level. The dangerous factor is the propagation of the delamination, which is influenced by the geometrical parameters, the material characteristics and the loading type. Both types of propagation can be present: slow and stable as well as fast and unstable.

In this investigation we have looked at a numerical simulation of the delamination of a laminated specimen made of unidirectional fiber-reinforced composite layers. This follows on from the work started in [1]. The aim is to design a numerical model for the simulation of crack propagation. An important parameter used in such analyses is the critical value of the energy-release rate ($G_c$).

The majority of studies investigating the delamination on laminated structures use either the critical value of energy-release rate $G_c$ [2–4] or the stress-intensity factor $K_c$ [5] as the interlaminar fracture toughness. The early studies were focused mainly on the experimental procedures and analytical solutions. These were later followed by studies dealing with numerical simulations based on a finite-element analysis and introducing new, special element types for the modeling of the delamination [6–8].

It is known that the critical value of $G_c$ as calculated according to the ASTM standard [9] does not behave as a constant. The critical value changes during the prescribed test by as much as tens of percent. Therefore, it is questionable as to which value should be chosen, for instance, for the numerical simulation.

In this work the value of $G_c$ is assessed by experimental measurements on a Mode-I delamination specimen. The analysis was performed on a cross-ply laminate manufactured from unidirectional plies reinforced with carbon fibers in an epoxy resin. It is known [10] that in the case of linear stress-strain behavior there is equality between $G$ and the value of the J-integral ($J$). Therefore, it was possible to substitute the evaluation of the decisive parameter $G_c$ with the calculation of $J_c$ in the numerical simulations. The numerical calculations are carried out using the finite-element method in MSC.Marc.

The difference between the experimentally and numerically obtained dependencies of force vs. displace-

ment for the critical value $G_c$ is presented. The basic material parameters (elasticity constants) used in the simulations were identified in previous studies [11,12], where the damage and failure of specimens made of the same material are investigated.

## 2 EXPERIMENT

Firstly, an experimental assessment of the inter-laminar toughness for Mode-I delamination was carried out according to the standard ASTM D 5528-01 [9]. The specimens used were rectangular strips denoted as DCB (Double Cantilever Beam) having dimensions $l \times b$ = (160 × 19.7) mm (see **Figure 1**). Each specimen was cut out using a water jet from a 4.6-mm-thick laminated cross-ply composite plate with a lay-up [0/90/90/0], whereas the middle part was 0.3 mm thick (see **Figure 2**). The plate was manufactured from epoxy prepregs reinforced with continuous Toray T600SC carbon fibers using autoclave technology. A non-adhesive aluminum foil, which served as the initial crack, was inserted into the midplane of the plate (i.e., between the 90 degree plies) during manufacture (see **Figures 1 and 4**). The thickness of the foil was 11 μm.

The experiment was performed on the Zwick/Roell Z050 testing machine. The opening force was applied using two piano hinges bonded on the lower and upper surfaces of the specimen (see **Figures 1 and 3**). During the testing process the dependence of the opening force $F$ vs. the transverse (or load point) displacement $\delta$ was recorded (see **Figure 3**). The crack propagation with time (crack length $a$) was inspected optically using a digital camera (Canon EOS 400D, Sigma 105/2.8 EX DG MACRO) every 10 s (resolution approximately 20 px/mm). The optical measurement also served as a verification of the transverse displacement values, which might differ, in general, from the grip movement, as recorded by the testing machine, due to its imperfect rigidity. The delamination process had a slow and stable character up to the final rupture. The speed of the grip movement was 10 mm/min.

The major problems identified during the experiments were the inhomogeneity of the initial crack zone

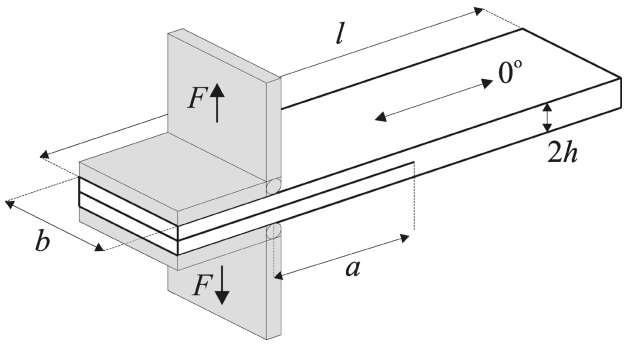


**Figure 1:** DCB specimen with attached piano hinges and inserted foil
**Slika 1:** DCB-vzorec s pritrjenim šarnirom in z vstavljeno folijo

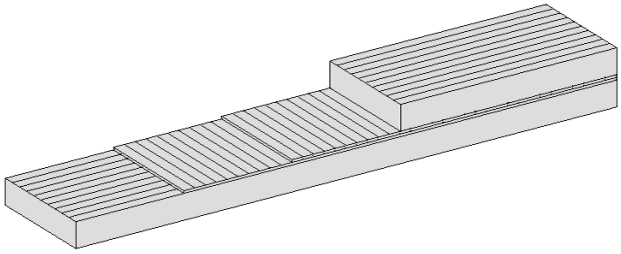

**Figure 2:** Material lay-up (showing the part without the foil)
**Slika 2:** Zlog materiala (prikazan je del brez folije)

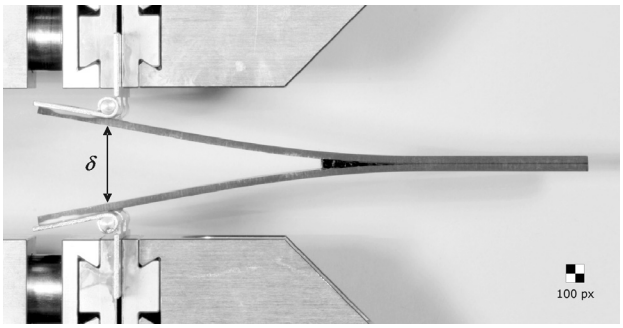


**Figure 3:** DCB specimen experimental setup
**Slika 3:** DCB-vzorec z eksperimentalno postavitvijo

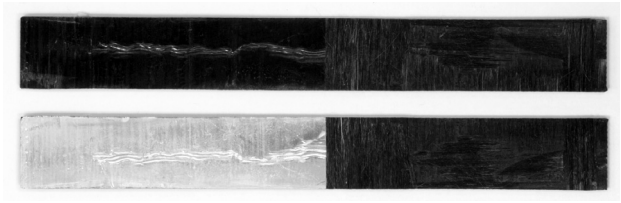

**Figure 4:** Crack surfaces of the fractured DCB specimen
**Slika 4:** Površina razpok pretrganega DCB-vzorca

(the end of the foil) and the so-called fiber bridging between the upper and lower parts of the specimen (see **Figure 5**). The bridging of fibers occurs in composite specimens within the unidirectional layers, as in this case.

## 3 ESTIMATION OF THE ENERGY-RELEASE RATE

The energy-release rate $G$ is defined mathematically, in general, as

$$G = -\frac{1}{b}\frac{\mathrm{d}U}{\mathrm{d}a} \tag{1}$$

where d$U$ is the differential increase in the strain energy, d$a$ is the differential increase in the delamination (or crack) length, and $b$ is the specimen width. Concerning the investigated Mode I for the DCB specimen, the corresponding energy-release rate $G_I$ can be expressed using the Euler-Bernoulli theory of beams as [3,13]

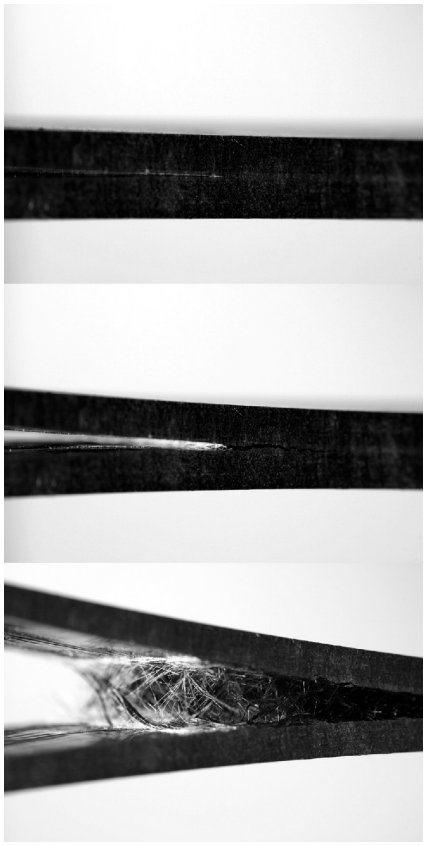

**Figure 5:** Sequence of photographs showing the fiber-bridging progress
**Slika 5:** Sekvenca posnetkov, ki prikazuje napredovanje vlaknate premostitve

$$G_{\mathrm{I}} = \frac{F^2 a^2}{bEI} \tag{2}$$

where $EI$ is the bending stiffness, i.e., the sum of the Young's moduli in the axial direction multiplied by the inertia moments for all the plies (see **Figure 1**).

There are several possible ways of calculating the strain-energy release (or eventually the interlaminar fracture toughness) according to the ASTM standard [9]. One way is the so-called Modified Beam Theory (MBT) method. The energy-release rate in this case is calculated as

$$G_{\mathrm{I}} = \frac{3F\delta}{2ba} \tag{3}$$

Since the beam is not perfectly built-in (a certain amount of rotation can occur at the crack front, i.e., where a clamped condition is assumed), a correction can be applied, which assumes that the delamination is larger by the amount $|\Delta|$. Hence, the crack length is $(a+|\Delta|)$ and the corrected energy-release rate is then given by

$$G_{\mathrm{I}} = \frac{3F\delta}{2b(a+|\Delta|)} \tag{4}$$

where the value of $\Delta$ is calculated according to the procedure given in the standard [9] and the values obtained for both types of specimens are shown in **Table 1**. Equation (2) can be corrected in a similar way.

## 4 NUMERICAL SIMULATION

The numerical simulation was performed using the finite-element method in the MSC.Marc system. In this case the analysis was solved as a plane-strain problem. The geometry was modeled using 4-node rectangular elements. The [0/90/90/0] lay-up was meshed with 8/2/2/8 layers of elements in the thickness direction and 600 elements along the length. A different model was prepared for each crack length $a$.

The equality between the values of the energy-release rate and the J-integral in the case of the elastic analysis was used in the simulations. MSC.Marc calculates the J-integral using the DeLorenzi method [14].

The material is assumed to be homogeneous, linearly elastic, and orthotropic, and to have the following elasticity constants: longitudinal Young's modulus $E_{\mathrm{L}}$ = 110000 MPa, transverse modulus $E_{\mathrm{T}}$ = 7700 MPa, Poisson's ratio $\nu_{\mathrm{LT}}$ = 0.28 and shear modulus $G_{\mathrm{LT}}$ = 4500 MPa, which were identified previously [11,12].

The critical values of the energy-release rate and the parameter $\Delta$ were calculated using (4) in order to best characterise the averaged experimental dependency in **Figure 6**. The hypothetical delamination curves for the interval $0.1 < G_{\mathrm{Ic}} < 1.5$ kJ/m$^2$ are shown in the graph together with the optimum curve corresponding to the values displayed in **Table 1**. The reconstructed load-displacement curve from the FEA is compared with the experiment.

**Table 1:** Measured and calculated parameters of the DCB specimen

| | | |
|---|---|---|
| Initial crack length /mm | $a_0$ | 62 |
| Crack-length correction /mm | $\lvert\Delta\rvert$ | 5.12 |
| Critical energy-release rate /(kJ/m$^2$) | $G_{\mathrm{Ic}}$ | 1.373 |

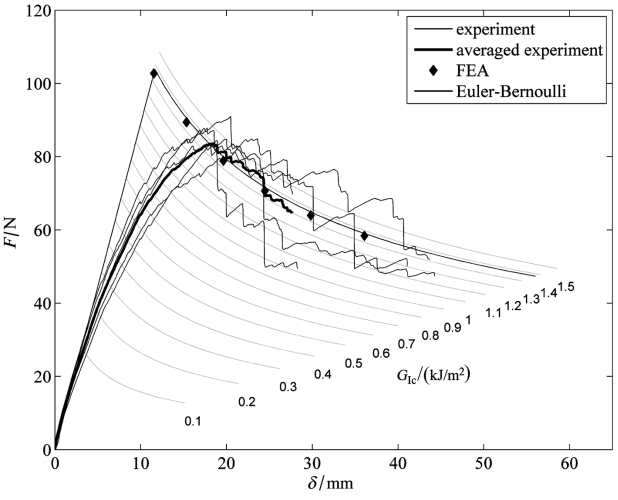


**Figure 6:** Load-displacement curves for the DCB specimen
**Slika 6:** Krivulje obremenitev – pomik za DCB-vzorec

## 5 CONCLUSIONS

An experimental investigation of low-speed Mode-I delamination was carried out on carbon-fiber-reinforced epoxy specimens in order to estimate the critical energy-release rate value $G_{Ic}$. The double-cantilever beam specimens with a cross-ply lay-up were manufactured with inserted aluminum foil serving as an initial crack. The critical energy-release-rate value was determined using the Euler-Bernoulli theory and the ASTM standard from the averaged experimental data. A numerical model was created in the FEA code MSC.Marc for the simulation of the experiment. The model took advantage of the equality between the energy-release rate and the J-integral in the case of an elastic material. The load-displacement dependency was reconstructed and compared with the experimental results. It is clear that it is possible to consider the critical energy-release rate value as the interlaminar fracture toughness in the case of the delamination of a composite with transversely oriented fibers.

### Acknowledgement

This work was supported by the research project GA AV IAA200760611 and research project MSM 4977751303.

## 6 REFERENCES

[1] V. Laš, R. Zemčík, P. Měšťánek: Numerical simulation of composite delamination with the support of experiment. Acta Mechanica Slovaca, 1 (**2006**), 303–308

[2] M. Hojo et al.: Mode I delamination fatigue properties of interlayer-toughened CF/epoxy laminates. Composite Science and Technology, 66 (**2006**), 665–675

[3] T. Kusaka et al.: Rate dependence of Mode I fracture behaviour in carbon-fibre/epoxy composite laminates. Composites Science and Technology, 58 (**1998**), 591–602

[4] A. B. Pereira, A. B. Morais: Mode I interlaminar fracture of carbon/epoxy multidirectional laminates. Composites Science and Technology, 64 (**2004**) 2261–2270

[5] W. T. Chow, S. N. Atluri: Stress intensity factors at the fracture parameters of delaminations crack growth in composite laminates. Composites Part B, 28B (**1997**), 375–384

[6] R. Borst, J. J. C. Remmers: Computational modelling of delamination. Composites Science and Technolgy, 66 (**2006**), 713–722

[7] C. H. Roche, M. L. Accorsi: A new finite element for global modelling of delaminations in laminated beams. Finite Elements in Analysis and Design, 31 (**1998**), 165–177

[8] F. Shen, K. H. Lee, T. E. Tay: Modeling delamination growth in laminated composites. Composites Science and Technology, 61 (**2001**) 1239–1251

[9] ASTM D5528-01, Standard Test Method for Mode I Interlaminar Fracture Toughness of Unidirectional Fiber-Reinforced Polymer Matrix Composites, Annual Book of ASTM Standard, 2002, 249–260

[10] D. P. Miannay: Fracture mechanics, Springer, 1998

[11] R. Zemčík, V. Laš: Identification of composite material properties using progressive failure analysis. Proc. of Computational mechanics 2005, Nečtiny, 2005, 695–700

[12] R. Zemčík, V. Laš: Numerical simulation of damage in fiber-reinforced composites and comparison with experiment. Proc. of 22nd Danubia-Adria symposium on experimental methods in solid mechanics, Monticelli Terme, Parma, 2005, 174–175

[13] M.-S. Sohn, X-Z Hu: Comparative study of dynamic and static delamination behaviour of carbon fibre/epoxy composite laminates. Composites, 26 (**1995**), 849–858

[14] MSC.Marc Volume A: Theory and user information, Version 2005. MSC.Software Corporation, 2004

UDK 669.14.018:669.18
Original scientific article/Izvirni znanstveni članek

ISSN 1580-2949
MTAEC9, 42(4)175(2008)

# APPLICATION OF THE THEORY OF PHYSICAL SIMILARITY FOR THE FILTRATION OF METALLIC MELTS

## UPORABA TEORIJE FIZIKALNE PODOBNOSTI ZA OPIS FILTRIRANJA KOVINSKE TALINE

**[1]Karel Stránský, [2]Jiří Bažan, [2]Jana Dobrovská, [3]Martin Balcar, [3]Pavel Fila, [3]Ludvík Martínek**

[1]VUT Brno, FSI, Czech Republic
[2]VŠB-Technical University of Ostrava, Czech Republic
[3]ŽĎAS, a.s. Žďár nad Sázavou, Czech Republic
stransky@fme.vutbr.cz

*Prejem rokopisa – received: 2007-10-08; sprejem za objavo – accepted for publication: 2008-05-07*

The Bernoulli equation is the basis for the primary description of the flow of a real metallic melt through the pouring system for the filling of the casting mould with an inserted ceramic filter. In principle, a modified, dimensionless form of the Bernoulli equation can be used for the determination of the loss coefficient $\xi$ as a general function of the dimensionless criteria – the Reynolds, Froude and Euler numbers. It was verified by modelling the flow of the modelling liquid (in this case water) through ceramic filters. In the same interval of Reynolds numbers the loss coefficient $\xi$ was greater for foam filters than for filters with direct holes (strainers); however, the outlet coefficient $\mu$ of the foam filters was, in identical conditions, significantly lower than that of filters with direct holes.

Key-words: similarity criteria, modelling, steel flow, ceramic filters, steel filtration

Bernoullijeva enačba je podlaga za opis pretoka taline skozi livni sistem z vstavljenim keramičnim filtrom. Načeloma je mogoče uporabiti modificirano brezdimenzijsko obliko Bernoullijeve enačbe za določitev koeficienta izgube $\xi$ kot funkcije brezdimenzijskega kriterija – Reynoldsovega, Froudovega ali Eulerjevega števila. S pretokom modelne tekočine (vode) je bilo preverjeno, da je pri enakem intervalu Reynoldsovih števil koeficient izgube $\xi$ večji pri penastem filtru kot pri filtru z direktnimi luknjicami, vendar pa je izhodni koeficient $\mu$ za penaste filtre pri enakih pogojih pomembno nižji kot pri filtrih z neposrednimi luknjicami.

Ključne besede: merila podobnosti, modeliranje, tok jeklene taline, keramični filtri, filtriranje jeklene taline

## 1 INTRODUCTION

The theory of physical similarity makes it possible to investigate the regularities of physical and other phenomena with similar behaviour, and it is possible to conclude from the known behaviour of one phenomenon, the behaviour of a second. This theory is based on similarity criteria, i. e., on dimensionless quantities (similarity numbers), which can substitute in the investigated phenomenon for dimensional physical quantities. The determination of similarity criteria is the basic task for the application of the theory of physical similarity of an investigated problem, since, on the one hand, they *reduce the number of variables* describing the given problem, and, on the other hand, they *specify the similarity relations* between the pertinent phenomenon and its model. The theory of physical similarity is used for the determination of similarity criteria and afterwards, for criteria dependencies, three methods of generalised variables, including the dimensional analysis, the analysis of the mathematical model and finally the analysis of the physical model.

The objective of this study is to prove that the technology of filtration of metallic melts can be efficiently investigated by the application of the theory of physical similarities using appropriately determined dimensionless similarity numbers – i. e., criteria. This study is based on extensive previous and current experimental research [1–6].

## 2 PRINCIPAL DIMENSIONLESS CRITERIA OF SIMILARITY FOR THE FILTRATION OF METALLIC MELTS

The *Bernoulli* equation is the basis for the primary description of the flow of a real metallic melt through the pouring system for the filling of the relevant casting mould with an inserted ceramic filter. With respect to the pressure losses caused during the flow through the filter, this equation can have the following form:

$$\frac{\rho w^2}{2} + h\rho g + p + \xi \frac{wv\rho}{d} = \text{const.} \qquad (1)$$

where $\rho w^2/2$ (Pa) represents the kinetic energy, $h\rho g$ (Pa) represents the positional or gravitational energy of the capacity of a liquid unity, which is determined by gravity, and $p$ (Pa) represents the potential pressure energy, which is usually dependent on the external

forces being exerted. The values in the equation are: $w$ = the real liquid flow-rate (m $s^{-1}$), $\rho$ = the density of the flowing liquid (kg $m^{-3}$), $h$ = the real position, the real height of the flowing liquid (m), $g$ = the acceleration due to gravity (m $s^{-2}$), $\xi$ = a dimensionless loss coefficient expressing the filter's hydraulic resistance (–), $\nu$ = the kinematic viscosity of the flowing liquid ($m^2$ $s^{-1}$) and $d$ = the diameter of the filter capillaries with direct holes (m). The pressure of the flowing real liquid $p$ is expressed in a basic unit (Pa) with the basic physical dimension of (kg $s^{-2}$ $m^{-1}$). It follows from the *Bernoulli* equation that the sum of the kinetic, positional, pressure and loss energy of an ideally flowing liquid remains constant, i.e., *const* in volume unit at each place during its flow.

The original *Bernoulli* equation (1) is transformed by division with the expression $\rho w^2/2$ (Pa) to a dimensionless form

$$1+\frac{2hg}{w^2}+\frac{2p}{\rho w^2}+\xi\frac{2\nu}{wd}=\frac{2\ \text{const.}}{\rho w^2} \qquad (2)$$

which contains the already standard (internationally) adopted dimensionless similarity criteria, namely: the Froude criterion $Fr = w^2(hg)^{-1}$, the Euler criterion $Eu = p\rho^{-1}\ w^{-2}$ and the Reynolds criterion $Re = wd\nu^{-1}$. With the use of these similarity criteria (numbers) it is possible to express the *Bernoulli* equation in a dimensionless form:

$$1+\frac{2}{Fr}+2Eu+\frac{2\xi}{\text{Re}}=\frac{2\ \text{const.}}{\rho w^2} \qquad (3)$$

The Froude criterion $Fr = w^2(hg)^{-1}$ expresses the ratio of the inertia and the gravitational forces in the flowing metallic liquid, including its undulation, vortices and also surface phenomena. It is often also called the Froude criterion 1, $Fr_1$, in contrast to the Froude criterion 2, $Fr_2$, expressed in the form $Fr_2 = w(hg)^{-1/2}$, which characterises the so-called *"kinetic head"*.

The Euler criterion $Eu = p(\rho w^2)^{-1}$ expresses the ratio of the pressure and the inertia forces. It characterises the loss of pressure during the flowing of a real metallic liquid and influences the hydraulic resistance of the flowing liquid caused by viscous forces (viscosity).

The Reynolds criterion $Re = wd\nu^{-1}$ belongs to the basic hydrodynamic criteria and it characterises the ratio of the inertia and the viscous forces, i.e., the forces caused by the viscosity of the filtered metallic melt. Its absolute value contains information about the basic character of the flowing of viscous liquids, laminar or turbulent, and also the information about the transition from one type of form of flowing to another.

The modified dimensionless form of the *Bernoulli* equation (3) can, in principle, be used for the determination of the loss coefficient $\xi$, as a general function of dimensionless criteria

$$\xi=\frac{\text{Re}}{2}\left\{\frac{2\ \text{const.}}{\rho w^2}-\left(1+\frac{2}{Fr}+2Eu\right)\right\} \qquad (4)$$

which indicates that during the flowing of a metallic melt through the ceramic filter the loss coefficient is proportional to the Reynolds number, whereas the constant of proportionality is also dependent on the Froude and Euler numbers and on other parameters of the Bernoulli equation. The expression 2 const. $(\rho w^2)^{-1}$ is also dimensionless, since the original physical dimension of this constant is in pascal (Pa).

## 3 MODELLING OF A METALLIC MELT FLOW THROUGH CERAMIC FILTERS

The practical use of the interdependence between the loss coefficient and the used ceramic filter requires that an equation is determined that contains certain specific numeric values. It is possible to determine such an equation by an appropriately chosen and arranged type of modelling. For these purposes the hydraulic characteristics of filters with direct holes (strainers) and foam filters were chosen for the modelling. Water served as the modelling liquid, since its viscosity is quantitatively comparable with the viscosity of liquid steel. The measurement of the hydraulic parameters during the flowing of a liquid through ceramic filters was carried out on the water measuring line in the laboratory of the Department of Airplanes and Engines at the Military Academy in Brno.

The results of the measurements for two different types of filters are described in detail in the reports[7–9]:

a) For the same type of filter with direct holes (strainer) manufactured by the company Keramtech Žacléř, s. r. o., Czech Republic, a filter number of 0217, a diameter of 70 mm and a basic filter height (thickness) $L$ = 10 mm with 19 holes of diameter $D$ = 6 mm, in which a total of six filter-slenderness ratios were measured. The slenderness ratios were defined as the ratio of the filter height (thickness) $L$ and the diameter of one filter-capillary aperture $D$. The changes of slenderness were achieved by changes of the height (thickness) of the same type of filters and by their serial ordering (stacking).

b) For the same type of foam filter (*schaum filter*) with the dimensions (90×90×25) mm (8.0 ppi), manufactured by the company FOSECO, in which two different hole slendernesses were measured.

The first series of modelling, the results of which are briefly presented in this study, was focused on the determination of the loss coefficient $\xi$ and of the filter outlet coefficient $\mu$. The specific energy loss $e_z$ was defined for the purposes of the assessment of selected filters by the relation $e_z = (\xi w^2/2)$ ($m^2$ $s^{-1}$), which means that the energy loss is directly proportional to the filter loss coefficient (filter specific resistance) and the square of the flow rate of the modelling liquid – the water in the pipeline of the modelling system. The Reynolds number

of the investigated filters was defined by the standard relation

$$Re_F = \frac{w_F D_{hF}}{\nu} \quad (5)$$

where $w_F$ is the flow rate of the liquid in the filter and $D_{hF}$ is the hydraulic diameter of the filter, which is equal to the diameter of one of its apertures (capillaries). The filter outlet coefficient $\mu$ was defined as the ratio of the real volume flow of the modelling liquid (water) with respect to the friction losses and the possible contraction of the water jet to the ideal volume flow through the filter, determined from the equations for the flowing of an ideal liquid[7].

## 4 RESULTS OF THE MODELLING OF THE FLOW THROUGH CERAMIC FILTERS

In **Figure 1** the dependence of the *loss coefficient* $\xi_P$ of both types of ceramic filters, as determined by modelling, on the Reynolds number $Re_F$ and the slenderness of filter apertures *L/D* is shown. The loss coefficient is considered as the *local resistance of the filter* inserted into the pipeline (index P), and as the resistance corresponding to the state of the modelling liquid (i.e., water at a temperature of 20 °C) in the filter (index F). The two curves in the upper part of the diagram are valid for foam filters, while the group of curves in the bottom part of diagram relates to filters with direct holes (strainers). With increasing Reynolds number and decreasing filter slenderness the coefficient $\xi_P$, expressing the filter's resistance and the energy loss of the flowing liquid, decreases. However, for the foam filters the decrease of the coefficient $\xi_P$ with the decrease of the filter's slenderness *L/D* is distinctly larger than for filters with direct holes.

The modelling of the *filter-outlet coefficient* $\mu$ is shown in **Figure 2**. The two curves in the bottom part of the diagram are related to foam filters, while the group of curves in the upper part of the diagram are related to filters with direct holes. The outlet coefficient $\mu$ also

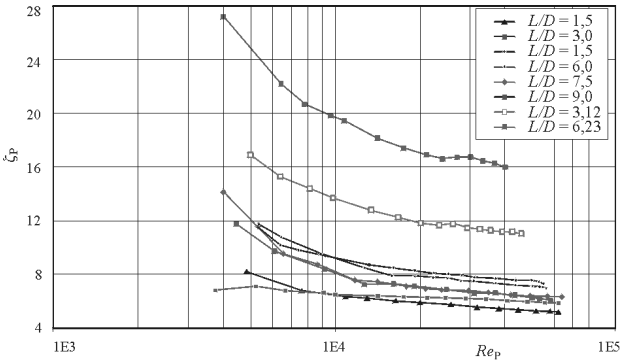


**Figure 1:** Dependence of the coefficient of the local resistance of the ceramic filters on the Reynolds number and the filter's slenderness

**Slika 1:** Odvisnost koeficienta lokalnega upora keremičnega filtra of Reynoldsovega števila in od vitkosti filtra

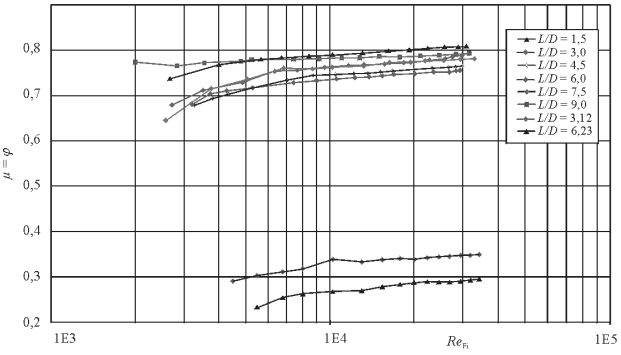


**Figure 2:** Dependence of the filter-outlet coefficient on the Reynolds number and the ceramic filters' slenderness

**Slika 2:** Odvisnost izhodnega koeficienta od Reynildsovega števila in od vitkosti filtra

expresses the contraction $\varphi$ of the modelling liquid flowing out of the filter. It is obvious that the foam filters have, in comparison with the filters with direct holes, significantly lower values of the outlet coefficient $\mu$, although the slendernesses of the apertures (capillaries) were otherwise identical. The values of the outlet coefficients $\mu$ for the foam filters vary in the interval 0.23 to 0.35, while the values of the outlet coefficients $\mu$ for the filters with direct holes are within the interval 0.65 to 0.80, and the Reynolds numbers are very close $Re_{Fi} = 2 \cdot 10^3$ to $3.5 \cdot 10^4$ (**Figure 2**). It is worth noting that the Reynolds number $Re_{Fi}$ in the diagram shown in **Figure 2** is linked to the Reynolds number $Re_P$ in the diagram shown in **Figure 1** by equation (6) in the following manner:

$$\mathrm{Re_p} = \frac{\mathrm{Re_{Fi}}}{\sqrt{1+\xi_p}} \quad (6)$$

During the modelling measurements the theory of physical similarities was strictly respected and the obtained results were expressed with dimensionless similarity numbers.

## 5 CONCLUSIONS

The results of the modelling measurements shown in **Figures 1** and **2** indicate that it is characteristic for both different types of ceramic filters (i.e., filters with direct holes and foam filters) that lower the values of the coefficient $\xi_P$, expressing the filter losses or the resistance to the flowing of the liquid through the filter, correspond to higher values of the coefficient $\mu = \varphi$, expressing the contraction of the liquid flow flowing out from the filter aperture (capillary) and vice versa. The higher hydraulic resistance during the flow of the steel melt through the foam filters favourably affects the micro-mechanism of filtration. The hydraulic resistance influences the filtration of metallic liquid through ceramic filters with direct holes (capillaries) to a considerably lesser degree. **Table 1** summarises the values for

**Table 1:** Comparison of the kinematic viscosity of liquids flowing through the filters – water and steel
**Tabela 1:** Primerjava kinematične viskoznosti tekočin, ki se pretakajo skozi filter – voda in jeklena talina

| Kinematic viscosity $\nu$ / $m^2\ s^{-1}$ | Model – water [10] | | Reality – carbon steel [11] | |
|---|---|---|---|---|
| | Temperature /°C | Viscosity /$m^2\ s^{-1}$ | Temperature /°C | Viscosity /$m^2\ s^{-1}$ |
| | 20 | $1.55 \cdot 10^{-7}$ | 1600 | $6.23 \cdot 10^{-7}$ |

the kinematic viscosity of the water at the temperature of the modelling of flow through the filter and carbon steel containing the mass fraction of C 0.25 % at the casting temperature.

This work was realised within the frame of the projects GA ČR reg. no. 106/06/0393 and EUREKA E!3192 ENSTEEL.

## 6 REFERENCES

[1] M. Příhoda, J. Bažan, J. Dobrovská, P. Jelínek, Z. Jonšta, M. Vrožina: *Nové poznatky z výzkumu plynulého odlévání oceli [New findings from research of continuous casting of steel]*, VŠB – Technical University of Ostrava, Faculta of Metallurgy and Materials Engineering, Ostrava (**2001**), 175 pp. ISBN 80-248-0037-3

[2] J. Happ, M. G. Frohberg: *Untersuchungen zur Filtration von Eisenschmelzen,* Giessereiforschung 23 (**1971**) 1, 1–9

[3] G., F. A. Acosta et al.: *Analysis of Liquid Flow through Ceramic Porous Media Used for Molten Metal Filtration*, Metallurgical and Materials Transactions B 26B (**1995**), 159–171

[4] J. Roučka et al.: *Filtrace slévárenských slitin [Filtration of casting alloys]*, Czech Foundry Society – Technological committee, Brno (**2000**), ISBN 80-02-01389-1

[5] P. Jonáš: *O turbulence [On turbulation]*, Inženýrská mechanika 5 (**1998**) 2, 89-106

[6] J. Bažan, K. Stránský: *Flowing of the melt through ceramic filters,* Materiali in Tehnologije / Mater. Tehnol. 41 (**2007**) 2, 99–102

[7] J. Maxa, D. Rozehnal, P. Onderlička: Stanovení hydraulických poměrů cedítkového a pěnového filtru modelováním [Determination of hydraulic characteristic of strainer and foam filter by modelling], Military Academy in Brno, (**1996**), 50 p

[8] J. Maxa, D. Rozehnal, P. Onderlička: Matematické zpracování výsledků měření cedítkových a pěnových keramických filtrů získaných modelováním [Mathematical processing of results of measurement of strainer and foam ceramic filters obtained by modelling], Military Academy in Brno, (**1996**), 52 p

[9] J. Maxa, D. Rozehnal: Stanovení hydraulických poměrů cedítkových filtrů modelováním [Determination of hydraulic characteristic of strainer filters by modelling], Military Academy in Brno, (**1997**), 39 p

[10] K. Ražnjević: *Termodynamické tabulky [Thermo-dynamic tables]*. Vydavateľstvo technickej a ekonomickej literatúry ALFA, Bratislava (**1984**), 313 p

[11] T. Myslivec: Fyzikálně chemické základy ocelářství *[Physical-chemical principles of steelmaking]*. SNTL/ALFA, Praha (**1971**), 448 p

UDK 547:620.1:61
Original scientific article/Izvirni znanstveni članek

ISSN 1580-2949
MTAEC9, 42(4)179(2008)

# PRIPRAVA NANOKOMPOZITA ZA BIOMEDICINSKE APLIKACIJE

## PREPARATION OF NANO-COMPOSITES FOR BIOMEDICAL APPLICATIONS

**Stanislav Čampelj[1], Darko Makovec[1], Luka Škrlep[2], Miha Drofenik[1,3]**

[1]Odsek za sintezo materialov, Institut "Jožef Stefan", Jamova 39, SI-1000 Ljubljana, Slovenija
[2]Zavod za gradbeništvo Slovenije, Dimičeva 12, 1000 Ljubljana, Slovenija
[3]Fakulteta za kemijo in kemijsko tehnologijo, Univerza v Mariboru, Smetanova ul. 17, SI-2000 Maribor, Slovenija
stanislav.campelj@ijs.si

*Prejem rokopisa – received: 2007-11-23; sprejem za objavo – accepted for publication: 2008-04-24*

Kompozitni nanodelci, ki vsebujejo superparamagnetno maghemitno jedro, prevlečeno s tanko plastjo amorfnega silicijevega oksida so zelo obetaven material za uporabo v biomedicini. Magnetno jedro omogoča manipulacijo z delci z zunanjim magnetnim poljem, medtem ko plašč amorfnega silicijevega oksida omogoča vezavo različnih molekul na njihovo površino. Vezava različnih organskih molekul, na primer zdravilnih učinkovin, zahteva pripravo nanodelcev, ki imajo na površini sloj funkcionalizacijskih molekul z različnimi funkcionalnimi skupinami.

Funkcionalizacijo nanodelcev smo dosegli s kovalentno vezavo različnih silanskih molekul: (3-aminopropil)trietoksisilan (APS) in viniltrietoksisilan (VTS), na njihovo površino. Reakcija je potekla v mešanici etanola, v katerem je bila predhodno raztopljena izbrana silanska molekula, in stabilne vodne suspenzije kompozitnih nanodelcev. Vezavo različnih silanskih molekul na površino nanodelcev smo spremljali z elektrokinetičnimi meritvami in s konduktometrično meritvijo koncentracije molekul na njihovi površini. Izkazalo se je, da lahko vežemo na delce molekule APS v površinski koncentraciji, ki se sklada s koncentracijo silanolnih skupin na površini amorfnega silicijevega oksida.

Ključne besede: nanodelci, nanokompoziti, silani, zeta-potencial, funkcionalizacija

Composite nano-particles of superparamagnetic maghemite particles coated with a thin layer of silica are very promising material for biomedical applications. The magnetic core of the composite nano-particles allows manipulation of particles with external magnetic field while the silica shell allows additional bonding of molecules to the surface. Different organic molecules, such as medical drugs, require nano-particles with a layer of functionalization molecules with different functional groups.

The functionalization of nano-particles was achieved with covalent bonding of different silanol molecules: (3-aminopropyl) triethoksysilane (APS) and vinyltriethoksysilane (VTS) to their surface. Reaction took place in a mixture of ethanol with previously dissolved silane and stable aqueous suspension of composite nano-particles. The bonding of different silanol molecules was monitored with electro-kinetic measurements and with conductometric measurements of molecules on the surface. The concentration of APS molecules which can be bondend to the surface of the composite nano-particles is in accordance with the concentration of silanol groups on the surface of silica.

Key words: nanoparticles, nanocomposites, silanes, zeta potential, fuctionalisation

## 1 UVOD

V zadnjih letih se veliko pozornosti namenja uporabi magnetnih nanodelcev v medicini. Magnetizem delcev nam omogoča, da lahko z njmi na daljavo manipuliramo z zunanjim magnetnim poljem, spremljamo njihov položaj ali jih segrevamo. Uporabljamo jih tako v diagnostične namene, kot je na primer za povečevanje kontrasta pri slikanju z NMR-tehniko, kot tudi v terapevtske namene, kot sta na primer magnetna hipertermija in ciljni vnos zdravilnih učinkovin. Primeren magnetni material za uporabo v medicini je maghemit ($\gamma$-$Fe_2O_3$), ki velja za nestrupen material[1,2]. Pogoj za uporabo nanodelcev v medicini je poleg majhne velikosti in zadovoljivih magnetnih lastnosti tudi njihova nestrupenost in specifične površinske lastnosti. Če želimo, da je magnetni nanokompozit primeren za uporabo v medicini, je treba na njegovo površino vezati različne biološke učinkovine. Vezavo učinkovin na površino nanokompozita dosežemo s funkcionalizacijskim slojem molekul, ki so vezane na njegovo površino. Ta sloj molekul zagotavlja funkcionalne skupine za kemijsko vezavo različnih učinkovin, hkrati pa preprečuje aglomeracijo nanodelcev med uporabo. Narava funkcionalizacijskih molekul določa tudi površinske lastnosti delcev (površinski naboj, polarnost) in s tem njihovo združljivost z biološkimi sistemi[3].

Za različne biološke uporabe je treba na površino delcev vezati različne biološke molekule, kot so na primer proteini, antigeni ali deli DNA-molekule, kar zahteva plast molekul z različnimi funkcionalnimi skupinami. Pomembno je, da so molekule močno vezane na površino delcev[4,5,6]. Ker je površina železovega oksida relativno inertna, ne omogoča močne vezave molekul. Močno kovalentno vezavo različnih molekul na površini delcev omogočimo, če oksidne delce prevlečemo z amorfnim silicijevim oksidom. Silicijev oksid ima namreč na površini močno vezane silanolne OH-skupine. Na površinske OH-skupine lahko nadalje kovalentno vežemo različne funkcionalizacijske mole-

kule. Plast silicijevega oksida na oksidnih delcih mora biti neprekinjena in homogena. Debelina plasti mora biti dovolj debela, da zaščiti magnetno jedro nanokompozita, hkrati pa dovolj tanka, da bistveno ne poslabša njegovih magnetnih lastnosti.

Silanolne skupine na površini amorfnega silicijevega oksida niso primerne za vezavo vseh biološko aktivnih molekul. Tako so za vezavo različnih molekul potrebne različne skupine, kot sta na primer aminoskupina ($NH_2$) ali karboksilna skupina (COOH). V tem primeru lahko vežemo na površinske silanolne skupine silane, ki nosijo želeno funkcionalno skupino. Silani so molekule, ki temeljijo na spojini silan, $SiH_4$. Navadno imajo na Si-atom vezane tri etoksidne skupine in eno alkilno verigo, ki se konča s funkcionalno skupino. Silani v vodi hidrolizirajo in reagirajo s površinskimi silanolnimi skupinami ter tako tvorijo močno Si-O-Si-vez s površino silicijevega oksida[7,8,9] še za APS.

Pri tem delu smo sistematično raziskovali vezavo različno funkcionaliziranih silanskih molekul (APS, VTS) na površino kompozitnih nanodelcev iz maghemitnega jedra in tanke prevleke silicijevega oksida.

## 2 EKSPERIMENTALNO DELO

### *2.1 Priprava nanokompozita*

Sintezni postopek za pripravo kompozitnih nanodelcev je podrobno opisan drugje[10]. Nanodelce maghemita smo sintetizirali s koprecipitacijo ionov $Fe^{2+}$ in $Fe^{3+}$ v vodni raztopini s koncentrirano raztopino amonijaka. Sintetizirane nanodelce smo sprali z amonijakalno raztopino (pH > 10,5). Na delce smo v naslednji stopnji adsorbirali citronsko kislino. Ta deluje kot surfaktant in prepreči njihovo aglomeracijo. Prekrivanje delcev s silicijevim oksidom je potekalo s hidrolizo tetraetoksisilana (TEOS). V etanolu raztopljen TEOS smo dodali v stabilno suspenzijo maghemitnih nanodelcev. V suspenziji nastane hidroliza TEOS-a in nukleacije silicijevega oksida na površni maghemitnih nanodelcev. Pomembno je, da v suspenziji ni aglomeratov nanodelcev, saj bi v tem primeru prekrili s silicijevim oksidom aglomerate, in ne posameznih nanodelcev. Tako pripravljene kompozitne nanodelce smo sprali in dispergirali v vodi.

Analiza kompozitnih nanodelcev je pokazala, da so iz magnetnega maghemitnega jedra s premerom (13,7 ± 2,9) nm in iz plasti amorfnega silicijevega dioksida z debelino okoli 2 nm. Izračunana masna ploščina nanokompozita je 94,4 $m^2/g$. Iz magnetnih meritev je razvidno, da kažejo kompozitni nanodelci superparamagnetizem ob relativno visoki nasičeni magnetizaciji $35 \cdot 10^{-4}$ T/g.

### *2.2 Vezava silanskih molekul na površino kompozitnih nanodelcev*

Na površino kompozitnih nanodelcev smo vezali naslednje silanske molekule: (3-aminopropil) trietoksisilan, $(CH_3CH_2O)_3Si(CH_2)_3NH_2$ (APS) in viniltrietoksisilan, $(CH_3CH_2O)_3SiCHCH_2$ (VTS) (**slika 1**). Vezava molekul je potekla v vodem mediju pri temperaturi 50 °C. Stabilni vodni suspenziji (20 mL) z masnim deležem 0,5 % kompozitnih nanodelcev smo dodali etanol (25 mL), v katerem smo predhodno raztopili silan (≈0,02 mol). Izračunan dodatek silana na površino nanokompozita je bil v vseh primerih 2 $mmol/m^2$.

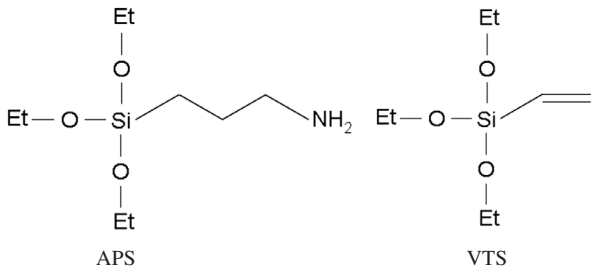


**Slika 1:** Shematski prikaz molekul APS in VTS
**Figure 1:** Schematic presentation of APS and VTS molecules

Za spremljanje prekrivanja površine kompozitnih delcev in določitev količine silana, ki je potrebna za popolno prekritje površine nanokompozita pri prej omenjenih pogojih, smo uporabili APS. Pri tem smo dodatek APS spreminjali od 1 $\mu mol/m^2$ do 2 $mmol/m^2$.

Po 5 h smo delce magnetno ločili in jih temeljito sprali z destilirano vodo. Uspešnost prekritja nanokompozita s silani smo spremljali z elektrokinetičnimi meritvami, ki so bile opravljene z zetametrom (Brookhaven Instruments Corp., ZetaPALS).

Površinsko koncentracijo aminoskupin na površini kompozitnih nanodelcev smo določali s kondukto-metrično titracijo. Suspenzijo spranih kompozitnih nanodelcev, prevlečenih z APS v vodi, smo titrirali z razredčeno raztopino klorovodikove kisline (HCl). Prevodnost suspenzije je odvisna od količine raztopljenih ionov v nosilni tekočini (vodi). Na začetku imamo v raztopini le $-NH_3^+$ vezane na površini delcev in ione $OH^-$ v vodi. Lastni pH suspenzije je 9. Med titracijo poteče reakcija med klorovodikovo kislino in aminoskupino. Pri tem nastaja nedisociirana molekula vode, ki ne prispeva k prevodnosti raztopine, zato se le-ta bistveno ne spremeni. Ko v raztopini ni več površinskih aminoskupin, ki bi bile na voljo za reakcijo s klorovodikovo kislino, se količina ionov z vsakim dodatkom kisline zelo poveča. Posledica je povišana prevodnost raztopine. Ekvivalentna točka se določi iz ostre spremembe v naklonu premice odvisnosti prevodnosti od koncentracije dodane HCl. Prevodnost suspenzije smo merili s konduktometrom (Radiometer analytical IONcheck30).

## 3 REZULTATI IN DISKUSIJA

**Slika 2** prikazuje elektrokinetične meritve za kompozitne nanodelce, funkcionalizirane z različnimi silani. Sami kompozitni nanodelci kažejo v nevtralnem močno negativen zeta- potencial, ki je posledica negativno

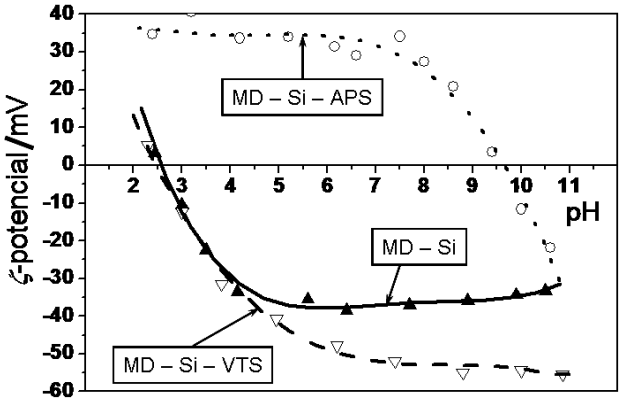


**Slika 2:** Graf elektrokinetičnih meritev za nanokompozitne delce (polna linija), nanokompozitne delce, funkcionalizirane z APS (pikčasta linija) in nanokompozinte delce, funkcionalizirane z VTS (črtkana linija)

**Figure 2:** Graph of electro kinetics measurements for nano-composite particles (full line), nano-composite particles functionalized with APS (dotted line) and nano-composite particles functionalized with VTS (dashed line)

nabitih silanolnih OH-skupin na površini. Tako imajo izoelektrično točko (IEP) pri kisli pH-vrednosti okoli 2,5. Iz elektrokinetičnih meritev je razvidno, da je v vseh primerih funkcionalizacije prišlo do sprememb na površini delcev, kar gre pripisati uspešni vezavi silanov na njihovo površino. Po pričakovanju je sprememba najbolj očitna, če na površino delcev vežemo APS. Opazen je premik IEP od pH = 2,5 na pH = 9,5. APS ima na koncu alkilne verige aminoskupino, ki je po naravi bazična. To pomeni, da je v območju visokih pH-vrednosti nedisociirana in ima negativen naboj. Ko se pH-vrednost medija premakne na področje nizkih pH-vrednosti, se aminoskupina protonira in posledično dobimo pozitivno nabito skupino na koncu alkilne verige $-NH_3^+$.

V primeru vezave VTS na površino nanodelcev se IEP ne spremeni, pač pa se poveča negativni naboj. Vinilna skupina ima zaradi dvojne vezi povečano elektronsko gostoto in posledično višji negativni naboj.

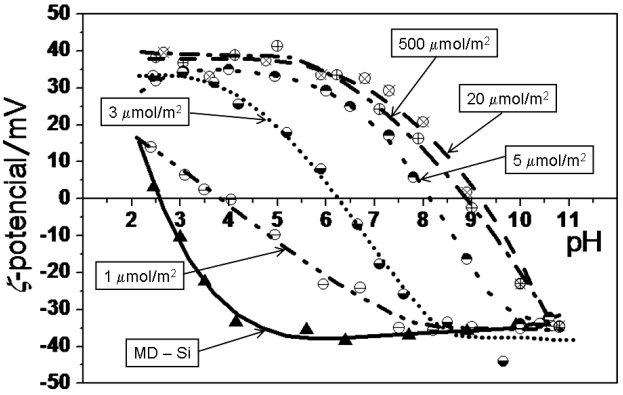


**Slika 3:** Graf elektrokinetičnih meritev za nanokompozit, funkcionaliziran z različnimi dodatki APS

**Figure 3:** Graph of electro kinetics measurements for nano-composite functionalized with different amounts of APS

V kislem območju pH-vrednosti poteče reakcija med dvojno vezjo in vodo, pri čemer nastane alkohol. Hidroksilna skupina na koncu alkilne verige je po svojih kemijskih lastnostih podobna silanolnim OH-skupinam, zato se IEP ne premakne.

**Slika 3** prikazuje elektrokinetične meritve za različne dodatke APS, uporabljene v procesu vezave na površino kompozitnih nanodelcev. Množina dodanega APS k nanodelcem je izražena v mikromolih APS na kvadratni meter površine nanodelcev. Z višanjem dodatka APS se viša koncentracija APS, vezana na površini nanodelcev, zato se IEP suspenzije postopno povečuje. Končno pH-vrednost IEP dosežemo pri dodatku APS enakem ali večjem od 20 μmol/m$^2$. Sklepamo, da je v tem primeru površina nanodelcev nasičena z vezanimi molekulami.

Rezultati elektrokemičnih meritev se skladajo s konduktometričnimi meritvami koncentracije aminoskupin na površini nanodelcev (**Tabela 1**). Z večanjem količine dodanega APS se veča tudi izmerjena koncentracija APS na površini nanodelcev. Pri dodatku 20 μmol APS na kvadratni meter površine nanodelcev, se je na površino vezal APS v površinski koncentraciji (8,1 ± 0,8) μmol /m$^2$ oziroma 4,8 ± 0,5 molekul APS na kvadratni nanometer površine nanodelcev. Vrednost se dobro ujema s številom silicijevih atomov oziroma silanolnih OH-skupin na površini amorfnega silicijevega oksida, ki je 4,55 molekul OH na kvadratni nanometer silicijevega oksida[11]. Na vsako od površinskih silanolnih skupin se namreč lahko veže po ena molekula APS. Pri višjih dodatkih APS je izmerjeno število aminoskupin na površini večje od teoretično možnega. Vzrok za to je verjetno nastanek polimernih molekul med hidrolizo APS zaradi relativno visoke koncentracije APS v suspenziji. Pri tem nastanejo polimerne molekule nižjih molekulskih mas, ki se med seboj povezujejo in pri tem nastajajo polimerne molekule višjih molekulskih mas. Teh z izpiranjem delcev po funkcionalizaciji verjetno nismo popolnoma izločili. Znano je, da ta proces nastane, ko koncentracija silana preseže vrednost ≈3 mmol/L. V primeru dodatka 500 μmol APS na kvadratni meter nanodelcev je bila koncentracija silana v vodni fazi suspenzije 86 mmol/L.

**Tabela 1:** Rezultati konduktometričnih meritev površinske koncentracije aminoskupin na površini nanodelcev v odvisnosti od dodatka APS uporabljenega v procesu funkcionalizacije.

**Table 1:** Results of conductometric titration measurements for the nano-composite functionalized with different amounts of APS

| Dodatek APS na površini delcev μmol/m$^2$ | 1 | 3 | 5 | 20 | 500 |
|---|---|---|---|---|---|
| Izmerjena površinska koncentracija amino-skupin, $c_{amino}$/(μmol/m$^2$) | 3,2 ± 1,5 | 3,7 ± 1 | 2,4 ± 1 | 8,1 ± 0,8 | 11,0 ± 1 |
| Koncentracija molekul APS na površini delcev, $c$/nm$^2$ | 1,9 ± 0,9 | 2,2 ± 0,6 | 1,4 ± 0,6 | 4,8 ± 0,5 | 6,6 ± 0,6 |

## 4 SKLEP

Površino magnetnih nanodelcev smo funkcionalizirali z vezavo različnih silanskih molekul ((3-aminopropil)trietoksisilan (APS) in viniltrietoksisilan (VTS)) na njihovo površino preko vmesne tanke plasti amorfnega silicijevaga oksida. Slednji omogoči s svojimi površinskimi silanolnimi OH-skupinami močno kovalentno Si-O-Si-vez silana s površino delcev. Površinska koncentracija silanskih molekul. vezanih na površini nanodelcev, se sklada s koncentracijo silanolnih skupin na površini amorfnega silicijevega oksida.

## 5 LITERATURA

[1] Q. A. Pankhurst, J. Connolly, S. K. Jones, J. Dobson, J. Phys. D: Appl. Phys. 36 (**2003**), R167–R181
[2] R. Hiergeist, W. Andrä, N. Buske, R. Hergt, I. Hilger, U. Richter, W. Kaiser, J. Magn. Magn. Mater., 201 (**1999**), 420–422
[3] C. C. Berry, A. S. G. Curtis, J. Phys. D, 36 (**2003**), R198–R206
[4] A. K. Gupta, M. Gupta, Biomaterials, 26 (**2005**), 3995–4021
[5] Y. Ichiyanagi, S. Moritake, S. Taira, M. Setou, J. Magn. Magn. Mater., 310 (**2007**), 2877–2879
[6] M. E. Park, J. H. Chang, Mat. Sci. Eng. C, 27 (**2007**), 1232–1235
[7] Z. Ma, Y. Guan, H. Liu, J. Magn. Magn. Mater. 301 (**2006**), 469–477
[8] X. Liu, J. Xing, Y. Guan, G. Shan, H. Liu, Colloids Surf A, 238 (**2004**), 127–131
[9] K. Woo, J. Hong, J. P. Ahn, J. Magn. Magn. Mater., 293 (**2005**), 177–181
[10] S. Čampelj, D. Makovec, M. Bele, M. Drofenik, J. Jamnik, Mater. Tehnol., 41 (**2007**), 103–107
[11] R. K. Iler, The chemistry of silica, John Wiley & Sons, New York 1979, 637

UDK 669.14.018.252:669.18:519.68
Professional article/Strokovni članek

ISSN 1580-2949
MTAEC9, 42(4)183(2008)

# THE DEVELOPMENT OF A CHILL MOULD FOR TOOL STEELS USING NUMERICAL MODELLING

## RAZVOJ KOKILE ZA ORODNA JEKLA Z UPORABO NUMERIČNEGA MODELIRANJA

**Martin Balcar, Rudolf Železný, Libor Sochor, Pavel Fila, Ludvík Martínek**

ŽĎAS, a.s., Strojirenska 6, CZ 59171 Zdar nad Sazavou, Czech Republic
martin.balcar@zdas.cz

*Prejem rokopisa – received: 2006-10-11; sprejem za objavo – accepted for publication: 2008-03-25*

A long lifetime and tools with optimum quality affect the primary production field and require improvements to the technological conditions of tool-steel ingot production. In the design of a newly developed chill-mould shape the specific casting and crystallization conditions of tool steel, large forging ingots are exploited. The casting and solidification processes were modeled numerically by applying the MAGMA software and the ingot shape was optimized with respect to the real solidification conditions, suppressing the ingot's internal discontinuities and obtaining an acceptable level of structural and chemical homogeneousness.

Key words: tool steel, mould, ingot casting, numerical modeling

Dolga trajnostna doba in optimalna kakovost vplivata na primarno proizvodnjo jekla in zahtevata izboljšanja v tehnologiji izdelave jeklenih ingotov. Pri razvoju nove kokile so bili upoštevani pogoji ulivanja in kristalizacije velikih ingotov iz orodnega jekla za izkovke. Procesa ulivanja in strjevanja sta bila modelirana z MAGMA-programom. Oblika ingota pa je bila optimizirana z upoštevanjem realnih razmer pri strjevanju, preprečen je bil nastanek notranjih diskontinuitet in dosežen sprejemljiv nivo strukturne in kemične homogenosti.

Ključne besede: orodno jeklo, kokila, ulivanje ingotov, numerično modeliranje

## 1 INTRODUCTION

In the frame of the traditional production of equipment and tools for heavy engineering and metallurgy, large forgings of tool steel are also manufactured at ŽĎAS. The tool-steel forgings with good forming properties and tougher requirements in terms of the product's internal quality can only be forged from ingots with a high internal quality. In earlier papers we have discussed the possible causes for the occurrence of inherent defects in heavy ingots of W. Nr. 1.2343 (X37CrMoV5-1) and W. Nr. 1.2344 (X40CrMoV5-1) tool steels according to EN ISO 4957 and in roll forgings of 8CrMoV or 8Cr3MoSiV steels.[1,2].

The optimization of the ingot-solidification process in the casting mould, the change of the mould shape and avoiding the formation of the defects in the ingot were achieved using the MAGMA software for the simulation of the casting and solidification process of the 8K8.4 forged ingot with a mass of 7.6 t. The project's success was achieved with the design and the verification of a new shape for the 8K9.2 chill mould for the casting of tool-steel ingots with a mass of 8.9 t.

## 2 DEFECTS IN TOOL STEEL INGOTS

In ZDAS heavy semi-products for tools are produced from ingots of the 8K series, with weights from 1000 kg to 11700 kg, forged on the CKV 630, CKV 1250 and CKV 1800 presses from the traditional steel grades EN ISO 4957 W. Nr. 1.2842 (90MnCrV8), W. Nr. 1.2842 (X210Cr12), W. Nr. 1.2343 (X37CrMoV51), W. Nr. 1.2344 (X40CrMoV51), W. Nr. 1.2714 (55NiCrMoV7) and special steels for rolls of 8CrMoV, 8CrMoSiV, 8Cr3MoSiV. The increased difficulty of making heavy forgings of tool steels is connected with the specific properties of high-carbon steels, alloyed with chromium, molybdenum and vanadium. Only by ensuring a sufficient forging-reduction ratio of the as-solidified steel, which may have a large number of defects in the final solidification areas in the axial part of the ingot, can a high internal quality of the forging be achieved. To achieve a high reduction ratio it is necessary to ensure a high forming rate and considerable deformation levels per compression.

Tool-steel forming with the CKV 1800 press is limited by the ingot reduction that can be achieved with the pressing force. For this reason, the deformation rate depends strongly on the temperature. A poor forging process may lead, in the case of the bar forgings of tool steels with a large diameter (>200 mm), to a low degree of deformation in the axial part of the forging. With respect to the requirements for the tool's service life and the resistance to considerable dynamic stressing, it is necessary to attain a high internal homogeneity without critical defects. The internal quality of the forgings is checked for crack and cavity occurrence by using ultrasonic examination.

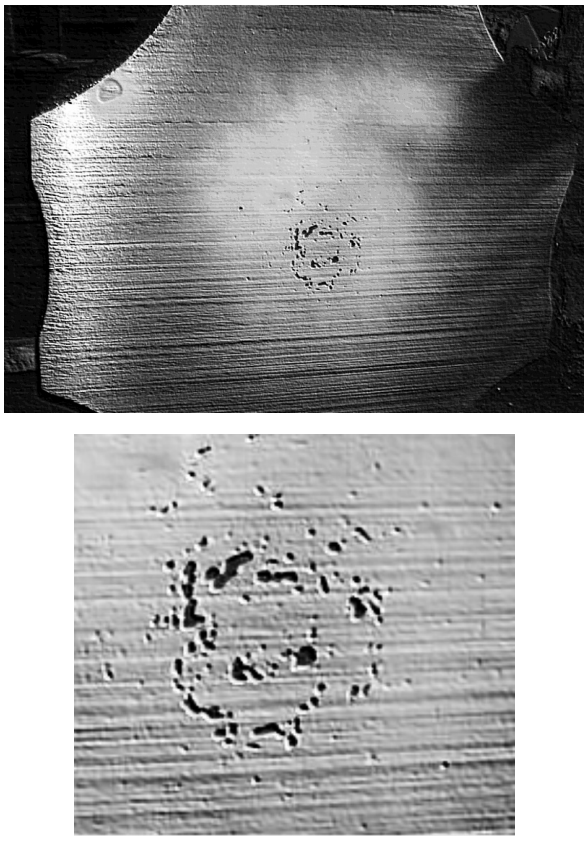

**Figure 1:** Cross-section at half ingot body height. Image of liquid penetrant test and detail of the axial part of the 8CrMoSiV steel ingot
**Slika 1:** Prečni prerez pri polovici višine ingota. Posnetek preiskave s tekočim penetrantom in detajl aksialnega dela ingota iz jekla 8CrMoSiV

The analysis of the tool-steel ingot and the forging carried out in connection with the extensive and repeated occurrence of axial defects in forgings has led to interesting findings for the 8K8.4 ingot's solidification, crystallization and forming. In spite of the exploitation of the limited possibilities of material deformation on the CKV 1800 press, the metallographic examinations of the forgings have not shown an insufficient forging reduction in the ingot axis, while ingot examinations have pointed out the causes of the defect occurrence at the forging axis.

**Figure 1** shows an image of an 8K8.4 ingot of 8CrMoSiV steel in cross-section at 1/2 ingot body height after a liquid penetrant test, with the considerable occurrence of regular cavities and shrinkage porosity at the ingot axis. The defects are confirmed to the ingot's vertical section, **Figure 2**, with imaging of the distribution and the shape of the defects throughout the vertical section of the ingot's upper part below the ingot's head.

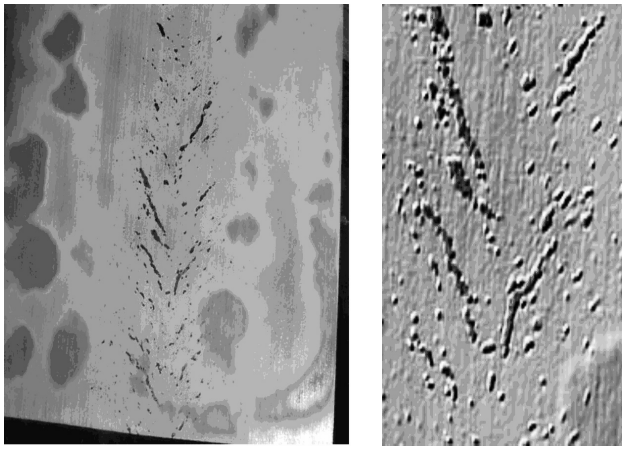

**Figure 2:** Longitudinal section of the part below the ingot head. Image of the liquid penetrant test and detail of the axial part of the 8CrMoSiV steel ingot
**Slika 2:** Vzdolžni prerez pod glavo ingota. Posnetek preiskave s tekočim penetrantom in detajl aksialnega dela ingota iz jekla 8CrMoSiV

## 3 NUMERICAL SIMULATION OF 8K8.4 INGOT CASTING AND SOLIDIFICATION

The conditions for simulations of the existing shape and the design of the optimized shape of the steel chill mould were selected on the basis of practical results and experience of forging the 8K8.4 ingot of 8CrMoSiV tool steel. From the MAGMA database, the GS80CrMo steel was selected because it is very similar to the steel grade investigated in terms of its chemical composition, which is shown for both steels in **Table 1**.

The solidification data were verified on a model of the current polygonal ingot type 8K8.4 of weight 7600 kg. The results of the numerical simulation were obtained as a set of graphical outputs from the MAGMA database and examined in compliance with the practical findings of the ingot's internal quality assessment. On the basis of the analysis, the following parameters for the simulation of the steel ingot's casting and solidification (marking according to the MAGMA database) were determined and selected for further work:

| | |
|---|---|
| SOLTIME | [s] |
| LIQTOSOL | [s] |
| NIYAMA | [1] |
| PRINCIPAL STRES | [MPa] |

**Table 1:** Chemical composition in mass fractions (w/%) of the 8CrMoSiVsteel and the GS80CrMo steel for the simulation from the MAGMA database
**Tabela 1:** Kemična sestava jekla 8CrMoSiV in jekla GS80CrMo iz baze podatkov MAGMA, ki je bila uporabljena pri simulaciji

| | C | Mn | Si | P | S | Cr | Ni | Mo | V |
|---|---|---|---|---|---|---|---|---|---|
| 8CrMoSiV | 0.78 - 0.85 | 0.30 - 0.40 | 0.60 - 0.80 | < 0.010 | < 0.005 | 1.80 - 2.10 | < 0.30 | 0.50 - 0.60 | 0.10 - 0.20 |
| 80CrMo | 0.80 | 0.40 | 0.45 | - | - | 2.00 | - | 0.30 | - |

MISES [MPa]
*w*(C) segregation [%]

**Figure 3** shows a graphical representation of the numerical simulation results of the 8K8.4 ingot of the GS80CrMo (8CrMoSiV) steel grade. The SOLTIME parameter in the figure shows the evolution of the solidus temperature zone and of the ingot solidification with its dependence on time.

The melt holding time at the liquidus and solidus temperatures interphase dividing line, LIQTOSOL in **Figure 4**, indicates that the metal in the ingot body axis remains at the liquidus–solidus interphase dividing line for a longer time than at the part below the ingot head.

The criterion for micro-shrinkage occurrence – NIYAMA – is shown in **Figure 5**. The vertical axial section through the ingot body in the Niyama criterion representation in scale (0–1) shows the risk points for the occurrence of micro-shrinkage. The Niyama criterion, decisive for the occurrence of micro-shrinkage, is defined as $G/\sqrt{T}$ ($K^{1/2} \cdot s^{1/2} \cdot mm^{-1}$) where $G/(K \cdot mm^{-1})$ is the temperature gradient and $^{T}/(K \cdot s^{-1})$ is the cooling rate. The critical value of the Niyama criterion, decisive for micro-shrinkage occurrence in the castings is 0.775 $K^{1/2} \cdot s^{1/2} \cdot mm^{-1}$. Accordingly, the area of overvalues for the critical limit of the Niyama criterion reflects the propensity for micro-shrinkage formation [3].

In the conditions of the steel ingots, the Niyama criterion determines the appearance of the material cavities and the micro-porosity. It is, however, not possible to determine with more precision the critical Miyama value on the basis of the available results. When representing the Niyama criterion in scale (0–1), a zone with the values $G/\sqrt{T}$ to 0.5 $K^{1/2} \cdot s^{1/2} \cdot mm^{-1}$ in the axial part of the ingot in **Figure 3**, some shrinkage porosity and cavities may form in the area at approximately 30 % of the body height.

The principal stress parameter in **Figure 5** shows the relative local stressing arising from volume changes in the course of a steel ingot's solidification. In the cross-section at 1/2 the ingot body's height, the zone of relatively high local stresses in the ingot body middle part is evident. The occurrence of high stressing in the ingot can also be related to the ingot's ability to provide the fluid phase in different solidification areas.

The MISES parameter in **Figure 6** shows the relative stress that is used to compare the triaxial stress state with the uniaxial stress state (with the rupture test). The stress values can be compared with the yield and the ultimate strength obtained with the tensile test.

The carbon concentration change throughout the ingot cross-section expressed by the concentration zones in **Figure 8**, does not show the significant non-mixing expected from the ingot's solidification process.

The results of the numerical simulation agree sufficiently well with the assessed internal quality of the experimental ingots and confirmed the conformity of the theoretical calculations and the practical experience. They also point out some possible causes for the occurrence of axial defects in the ingot and the forging of the tool steel.

The result of the simulations and verifications of the real ingot's internal quality was the starting stage for the design and construction of a new mould shape.

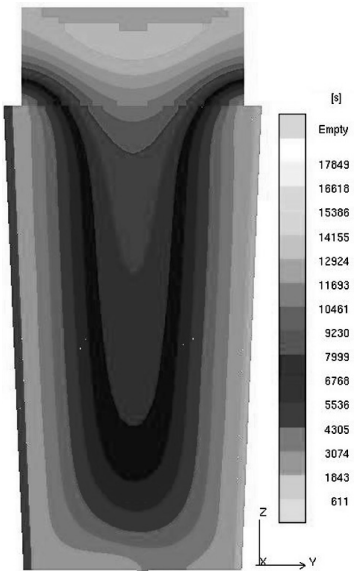


**Figure 3:** Ingot solidification time 8K8.4 (SOLTIME, s)
**Slika 3:** Čas strjevanja ingota 8K8.4 (SOLTIME, s)

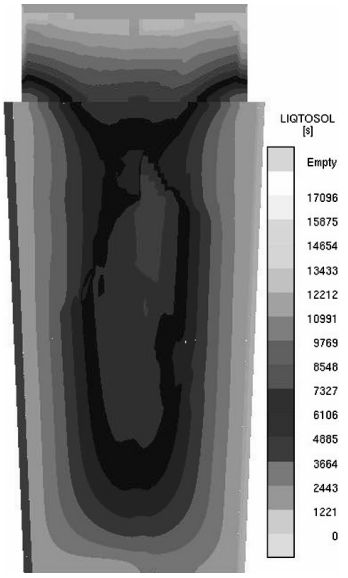


**Figure 4:** Time $T_{likvidus} - T_{solidus}$ 8K8.4 (LIQTOSOL, s)
**Slika 4:** Čas $T_{lik.} - T_{sol.}$ za ingot 8K8.4 (LIQTOSOL, s)

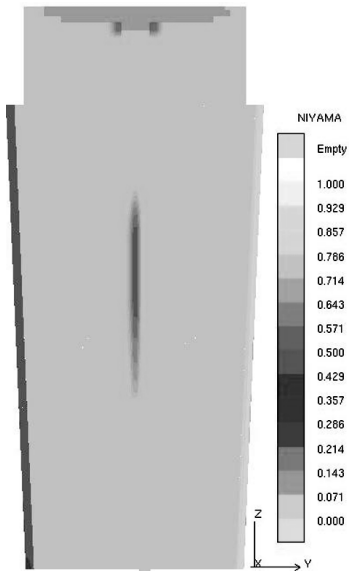


**Figure 5:** Niyama criterion 8K8.4 (NIYAMA [1])
**Slika 5:** Niyama–kriterij za ingot 8K8.4 (Niyama[1])

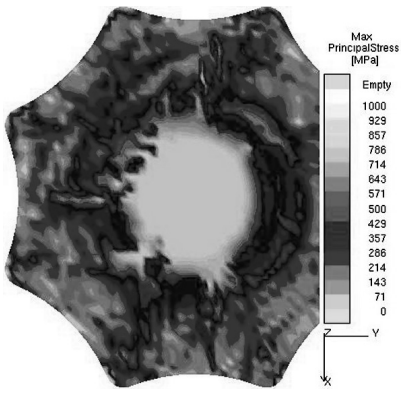


**Figure 6:** Relative local stress 1/2 ingot height 8K8.4 (PRINCIPAL STRESS, MPa)

**Slika 6:** Relativna lokalna napetost pri polovici višine ingota 8K8.4 (Glavna napetost, MPa)

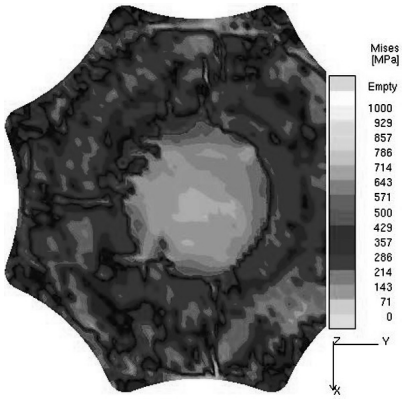


**Figure 7:** Relative stress 1/2 ingot height 8K8.4 (MISES, MPa)

**Slika 7:** Relativna napetost pri polovici višine ingota 8K8.4 (Mises, MPa)

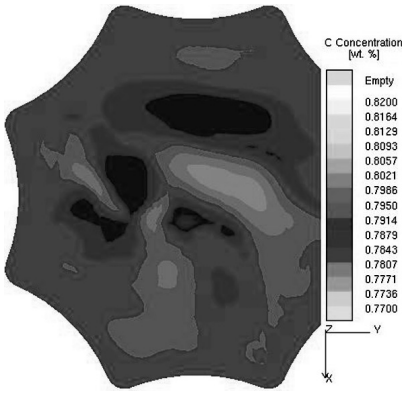


**Figure 8:** Carbon concentration 1/2 ingot height 8K8.4 (*w*(C)/%)

**Slika 8:** Koncentracija ogljika v masnih deležih pri polovici višine ingota 8K8.4 (*w*/C)/%)

## 4 DESIGN AND VERIFICATION OF THE INGOT 8K9.2

The design of the new shape of the mould and ingot evolved gradually with the comparison of the results of the calculations for a number of modifications to the mould's geometry. It was based on the present polygonal ingot – type 8K8.4, with a weight of 7600 kg. The main geometrical changes were for the slenderness and the taper of the ingot. The shape was finally modified to be suitable for a simulation of the solidification of the polygonal ingot 8K9.2 of weight of 8850 kg. The comparison between the basic parameters of the ingot 8K8.4 and the new shape design of the ingot 8K9.2 is shown in **Table 2**.

The results of the numerical simulation of casting and solidification of the ingot 8K9.2 of steel GS80CrMo (8CrMoSiV) evaluated in terms of selected parameters in a similar way as for the original ingot, are shown in **Figures 9 to 14**.

It is clear from **Figure 9** that the change to the mould's geometry has positively changed the shape and course of the curves of the time zones of the solidus temperature. In **Figure 10** the positive effect of the

**Table 2:** Basic parameters of the ingot 8K8.4 and the design of the ingot 8K9.2

**Tabela 2:** Osnovni parametri za ingot 8K8.4 in načrt za ingot 8K9.2

| Type | Weight and volume | | | | | S slenderness | V taper |
|---|---|---|---|---|---|---|---|
| | ingot | head | | body | | H | |
| | [kg] | [kg] | [%] | [kg] | [%] | D | [°] |
| 8K8,4 | 7 600 | 800 | 11% | 6 800 | 89% | 1.9 | 4.8 |
| 8K9,2 | 8 850 | 1 200 | 14% | 7 650 | 86% | 1.3 | 11.0 |

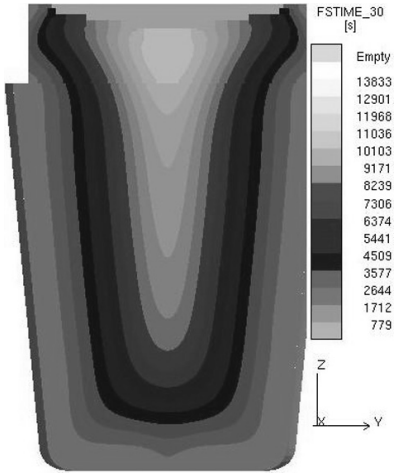


**Figure 9:** Ingot solidification time 8K9.2 (SOLTIME, s)

**Slika 9:** Čas strjevanja ingota 8K9.2 (SOLTIME, s)

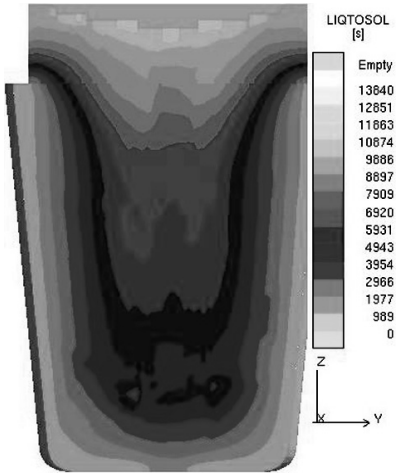


**Figure 10:** Time $T_{liquidus} - T_{solidus}$ 8K9.2 (LIQTOSOL, s)

**Slika 10:** Čas $T_{lik.} - T_{sol.}$ za ingot 8K9.2 (LIQTOSOL, s)

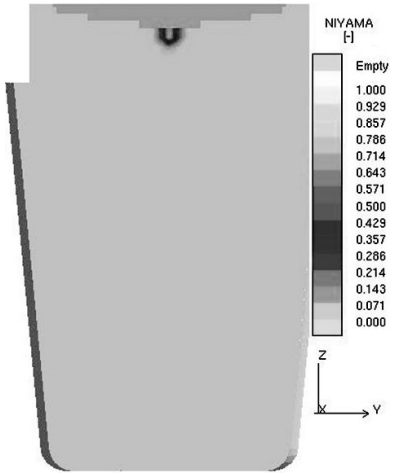


**Figure 11:** Niyama criterion 8K9.2 (NIYAMA [1])

**Slika 11:** Niyama–kriterij za ingot 8K9.2 (Niyama[1])

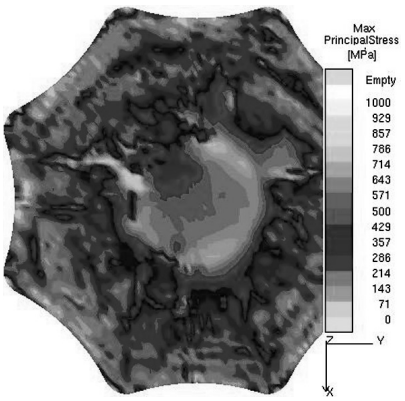


**Figure 12:** Proportional local stress 1/2 height of the ingot 8K9.2 (PRINCIPAL STRES, MPa)

**Slika 12:** Relativna lokalna napetost pri polovici višine ingota 8K9.2 (Glavna napetost, MPa)

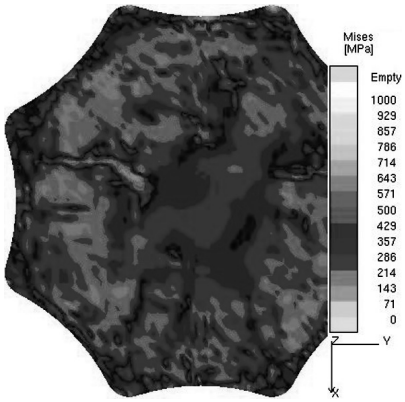


**Figure 13:** Relative stress 1/2 height of the ingot 8K9.2 (MISES, MPa)

**Slika 13:** Relativna napetost pri polovici višine ingota 8K9.2 (Mises, MPa)

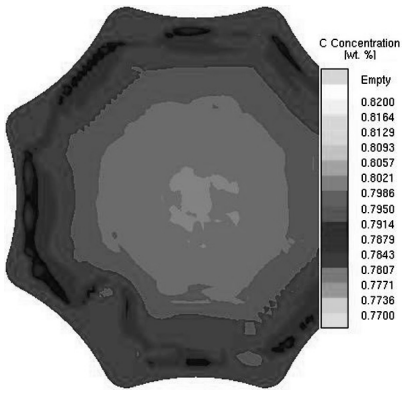


**Figure 14:** Carbon concentration 1/2 height of the ingot 8K9.2 (w(C)/%)

**Slika 14:** Koncentracija ogljika v masnih deležih pri polovici višine ingota 8K9.2 (*w*(C)/%)

enlargement of the ingot taper on the time of the melt persistence the phase-to-phase interface liquidus and solidus is shown. A comparison with **Figures 3 and 4** shows a significant improvement of the feeding of the fluid metal from the head into the body of the ingot. On the basis of the result of the simulation of the casting and the solidification an improvement to the internal quality of the ingot can be expected.

As shown in the ingot section in **Figure 11**, and with a difference compared to the ingot 8K8.4, no axial cavities and shrinkage porosities formed during the solidification of the ingot 8K9.2. In **Figure 12** and **Figure 13** are some interesting changes compared with the original ingot shape. The relative proportional local stress (principal stress) due to volume changes during the solidification of the ingot is reduced considerably. It is assumed that this change is connected with the improved flowability of the fluid metal to the phase-to-phase interface and/or to the point of steel solidification in the ingot. The interrelation between the relative stress and the proportional local stress parameter significantly increases the homogeneity of the stress distribution over the ingot cross-section. Thus, it is logical to expect a lower level of internal stresses in the ingot and an improved homogeneity of the steel's microstructure.

The effect of a change of the mould on the un-mixing and segregation processes is evident from the images in **Figure 14**. The chemical heterogeneity of the ingot 8K9.2 in terms of carbon concentration change over the ingot body cross-section is probably related to the lengthening of the solidification time. This time in the axis and in the middle part of the ingot body, as shown in **Figure 3**, is 9230 s for the ingot 8K8.4 and 11036 s for the ingot 8K9.2, and in **Figure 9** the solidification time for the new ingot shape is increased by 806 s, i.e., by 19.6 % compared to the initial ingot shape.

Based on the achieved improvements in terms of internal quality for the simulated ingot shape, two moulds of shape 8K9.2 were manufactured and their suitability for achieving better internal quality for ingots and forgings of the steel processed in the secondary metallurgy equipment in ŽDAS was tested. The tests were carried out with the steel EN ISO 4957 W. Nr. 1.2344 (X40CrMoV51) and two ingots of 8K9.2 were cast. One ingot was then processed by forming on the CVK 1800 press, using open-die forging technology, to a bar of 350 mm in diameter with the maximum material yield.

Of crucial importance for the evaluation of the effect of the change of the mould shape is the forging's internal quality, which is tested ultrasonically according to the standard SEP 1921. These tests showed that in terms of internal defects the experimental forging from the ingot 8K9.2 of steel EN ISO 4957 W. Nr. 1.2344 (X40CrMoV51) conformed with the levels A/a, B/b, C/c, D/d, E/e. For tool steels, the levels D/d and E/e are acceptable.

**Table 3:** Ingot utilization – EN ISO 4957 W. Nr. 1.2344 (X40CrMoV5-1) steel forging and internal quality tested ultrasonically per SEP 1921

**Tabela 3:** Uporaba ingota – EN ISO 4957 W. Nr. 1.2344 (X20CrMoV5-1) jekleni odkovek in podatki o notranji kakovosti, preskušeni z ultrazvokom po SEP 1921

| Typ | Hmotnost [ kg ] | Guaranteed Ultrasonic level | Ingot utilization | |
|---|---|---|---|---|
| | | | [ kg ] | [ % ] |
| 8K8,4 | 7600 | E/e | 0 | 0 |
| | | D/d | 4600 | 61 |
| | | C/c | 5450 | 72 |
| | | B/b | 5950 | 78 |
| 8K9,2 | 8850 | E/e | 7300 | 82 |

From the verifications carried out and the comparison of results of the statistical data on the earlier production of forgings of steel EN ISO 4957 W. Nr. 1.2344 (X40CrMoV51) shown in Table 3, it is evident that a considerable increase of the ingot yield was achieved after the introduction of the new mould shape.

The bar forging length complied at all levels with the requirements of the ultrasonic test for the ingot volume yield of 82 %. The difference to 100 % could not be used because of the crack extension from the ingot head during the forming process and also for the waste in the ingot foot due to the material flow and the loss during squaring up the face of the forging with machine cutting.

Based on the result of the first assessment it is possible to conclude that an improved internal quality of the ingot 8K9.2 in terms of ultrasonic tests of the internal quality of the tool-steel forging was achieved. This conclusion is confirmed with the results achieved with real shop orders for the tool-steel forgings of heavy bars and blocks with a weight up to 7 t, a bar diameter up to 600 mm and the height of the block up to 500 mm.

## 5 CONCLUSIONS

The MAGMA software was used for the design of a new shape for the 8K9.2 mould. In spite of the possible modeling errors, it is possible to conclude, based on the results achieved, that a great improvement in the quality of forgings has been attained as a direct result of the change in the geometry of the forging ingot of type 8K.

The development work will be continued with the aim of a further increase in the quality of the ingots and forgings of selected tool-steel brands and of the verification of the results of a numerical simulation in terms of the internal structure and of the chemical homogeneity related to the solidification and the forming of the ingot.

### Acknowledgements

The presented results are part of the TANDEM program of the FT–TA/061 project.

The project was implemented based on state resources with the financial support of the Ministry of Industry and Trade of the Czech Republic.

## 6 REFERENCES

[1] Martínek, L., Balcar, M., Novák, J., Sochor, L.: Rozbor vnitřních necelistvostí ingotu z nástrojové oceli. 6. Mezinárodné metalurgické sympozium. Rájecké Teplice, 2003

[2] Martínek, L., Balcar, M., Novák, J., Sochor, L.: Vnitřní struktura ingotu z nástrojové oceli. 20. konference Teorie a praxe výroby a zpracování oceli, Rožnov. Tanger, 2003

[3] Carlson, K.D., Shouzhu Ou, Hardin, R., Beckerman, Ch.: Development of New Feeding – Distance Rules Using Casting Simulation: Part I. Methodology. http://www.engineering.uiowa.edu/~becker/documents.dir/ FeedingPart1.pdf